

ADVANCING ASTEROID SURFACE EXPLORATION USING SUBLIMATE-BASED  
REGENERATIVE MICROPROPULSION AND 3D PATH PLANNING

by

Greg Wilburn

---

Copyright © Greg Wilburn 2019

A Thesis Submitted to the Faculty of the

DEPARTMENT OF AEROSPACE AND MECHANICAL ENGINEERING

In Partial Fulfillment of the Requirements

For the Degree of

MASTER OF SCIENCE

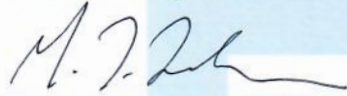
In the Graduate College

THE UNIVERSITY OF ARIZONA

2019

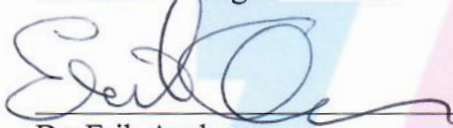
THE UNIVERSITY OF ARIZONA  
GRADUATE COLLEGE

As members of the Master's Committee, we certify that we have read the thesis prepared by Greg Wilburn, titled Advancing Asteroid Surface Exploration Using Sublimate-based Regenerative Micropropulsion and 3D Path Planning and recommend that it be accepted as fulfilling the dissertation requirement for the Master's Degree.



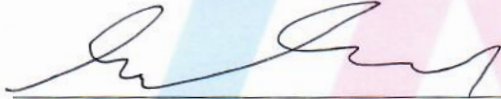
Dr. Jekan Thangavelauthum

Date: Dec 10, 2019



Dr. Erik Asphaug

Date: Dec 10, 2019

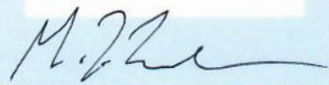


Dr. Eniko Enikov

Date: Dec 10, 2019

Final approval and acceptance of this thesis is contingent upon the candidate's submission of the final copies of the thesis to the Graduate College.

I hereby certify that I have read this thesis prepared under my direction and recommend that it be accepted as fulfilling the Master's requirement.



Dr. Jekan Thangavelauthum  
Master's Thesis Committee Chair  
Department of Aerospace and Mechanical Engineering

Date: Dec 10, 2019

ARIZONA

## **Acknowledgements**

The author would first like to thank his thesis committee members for their help and direction in solving some of the complex problems in this work. The author acknowledges the time and effort of his advisor, Dr. Jekan Thangavelauthum, for his guidance over the entire course of the project. Recognition is deserved for Dr. Erik Aspbaug and Dr. Stephen Schwarz for their development of the *AMIGO* robot concept. The development of MEMS systems presented could not have been done without the coursework and guidance from Dr. Eniko Enikov.

Special thanks goes to my friends and family who have supported and encouraged me through my graduate studies. I couldn't have done it without you, Emilia!

# Table of Contents

|     |   |     |
|-----|---|-----|
| I.  | Abstract .....  | 5   |
| 1.  | Introduction .....  | 6   |
|     | a. Background and Challenges .....  | 6   |
|     | b. Problem Statement .....  | 7   |
|     | c. Significance of the Project .....  | 8   |
|     | d. Scope of the Thesis and Outline .....  | 9   |
| 2.  | Asteroid Exploration and Mobility .....   | 11  |
|     | a. Science Rationale and Traceability Matrix .....                              | 12  |
|     | b. Literature Review: Mobility Actuation and Small Body Surface Explorers ..... | 18  |
| 3.  | AMIGO .....   | 21  |
|     | a. CubeSats .....   | 22  |
|     | b. AMIGO Concept .....  | 24  |
|     | c. Engineering Development Model and Testing .....                              | 28  |
| 4.  | Sublimate Regenerative Micropropulsion System and Micronozzle Design .....      | 38  |
|     | a. Literature Review: Other Micropropulsion Systems .....                       | 40  |
|     | b. Significance of the Asteroid Environment .....                               | 44  |
|     | c. Cold Gas Systems .....   | 45  |
|     | d. Sublimate Propulsion .....   | 47  |
|     | e. Micronozzle Design .....   | 49  |
|     | i. Quasi-Isentropic Analysis with Microfluidic Effects .....                    | 50  |
|     | ii. Constrained Particle Swarm Optimization .....                               | 56  |
|     | iii. Convergent Section and Throat Geometry Design .....                        | 60  |
|     | f. Computational Fluid Dynamics .....   | 61  |
|     | g. Nozzle Fabrication Methods to Explore .....                                  | 65  |
| 5.  | Valve Designs .....   | 70  |
|     | a. Literature Review of MEMS Valves .....                                       | 71  |
|     | b. Individual Nozzle Actuation Valves Design and Fabrication Process .....      | 76  |
|     | c. Main Sealant Valve Design and Fabrication Process .....                      | 88  |
| 6.  | Control Systems for Hopping, Attitude, and Up-Righting .....                    | 92  |
|     | a. Hopping Algorithm .....  | 93  |
|     | b. Attitude Control During Hops .....   | 96  |
|     | c. Up-Righting Maneuvers .....  | 102 |
| 7.  | Conclusion .....  | 105 |
|     | a. Summary of Findings .....  | 106 |
|     | b. Innovations .....  | 107 |
|     | c. Limitations .....  | 108 |
|     | d. Future Work .....  | 109 |
| II. | References .....  | 110 |

# I. Abstract

The advancement of asteroidal surface science necessitates in-situ science collection by robotic landers. The Asteroid Mobile Imager and Geologic Observer (AMIGO) is a conceptualized surface hopping robot relying on miniaturization of avionics, structures, and science equipment to accompany a larger “mothership” type orbiter for surface measurements. The scientific rationale for asteroid surface characterization is explored. Ideally, mobility facilitates more robust data collection from a range of areas on the asteroid surface with fewer robots for maximum coverage. As evidenced by images from asteroid visiting spacecraft, recently *Hayabusa II* and *OSIRIS-Rex*, “rock gardens” on asteroid surfaces provide uneven and obstructed terrain from boulders and piles of dust.

Two enabling technologies are developed for the CubeSat class AMIGO hopping robot. Hopping is enabled by a high-level path planning algorithm is developed by using a stereo camera that outputs both color images and a depth map for obstruction detection. The depth map allows for objects and adverse terrain to be detected and avoided for safer mobility. The surface boulders present difficulties in both line of site to other areas of the asteroid and in landing safely. These large obstructions and dramatic topology of asteroids reduces the robot’s visibility range and navigating around them provides new scenes to examine. The boulders should also be avoided when hopping such that they do not damage the robot or cause it to tip over to a state where data cannot be collected. Imaging from these new locations and headings can be used to construct surface level maps of the terrain and gather information on boulder distribution. The avoidance algorithm is evaluated on a test model of AMIGO with representative avionics and structure by hopping multiple times to avoid obstacles.

The other technology is a micropropulsion system based on cold-gas and microelectromechanical systems (MEMS) technology to provide both lift-off hopping actuation and 2-axis attitude control during a quasi-ballistic, open loop trajectory to a target destination. Hopping from the propulsion system allows the robot to traverse the rough terrain to an area deemed interesting or safe from the hop selection algorithm. The design methodology for the micronozzles and two control valves are shown. Micronozzles are optimized in a quasi-isentropic analysis and compared to computational fluid dynamics simulations.

# 1. Introduction

## 1.a: Background and Challenges

The science and origins of asteroids is deemed high priority in the *Planetary Science Decadal Survey*. Two of the main questions from the Decadal Survey pertain to what the “initial stages, conditions, and processes of solar system formation and the nature of the interstellar matter” that was present in the protoplanetary disk, as well as determining the “primordial sources for organic matter.” Major scientific goals for the study of planetesimals are to decipher geological processes in SSSBs not determinable from investigation via in situ experimentation, and to understand how planetesimals contribute to the formation of planets. Ground based observations are not sufficient to examine SSSBs, as they are only able to measure what is on the surface of the body; however, in situ analysis allows for further, close up investigation as to the surface characteristics and the inner composure of the body.

The advancement of asteroidal surface science necessitates in-situ science collection by robotic landers. The Asteroid Mobile Imager and Geologic Observer (AMIGO) is a conceptualized surface hopping robot relying on miniaturization of avionics, structures, and science equipment to accompany a larger “mothership” type orbiter for surface measurements. Ideally, mobility facilitates more robust data collection from a range of areas on the asteroid surface with fewer robots for maximum coverage. As evidenced by images from asteroid visiting spacecraft, recently *Hayabusa II* and *OSIRIS-Rex*, “rock gardens” on asteroid surfaces provide uneven and obstructed terrain from boulders and piles of dust.

Multiple actuation modes exist to facilitate mobility. These systems must fit within the 1U CubeSat form factor along with all other components for successful robot operation and science collection. It should also have minimal dependence on the surface characteristics of which little is known while being efficient for longer mission life

## 1.b: Problem Statement

The goal of this thesis is to develop a mobility mode for robotic exploration of small solar system body surfaces. Two systems must be developed to meet this end. Firstly, a method to plan a path across the surface is needed. The surface of asteroids is rough with many features that are both interesting and detrimental to a robot's lifespan. Ideally, the visualization system for object detection should augment one of the science instrument's capabilities. The most viable option is a top-mounted stereo camera planned to be used on AMIGO. It is assumed an open-loop path planning algorithm will be developed such that the path can be calculated once with no need for in-route corrections.

The other system to be developed is mobility actuation on an asteroid's surface. Traditionally, rovers have been used on other bodies such as Mars and the Moon. Since the Soviet *Lunokhod* rovers of the early 1970's, roving capabilities have been extended and proven widely successful. Much is known about careful design of suspension, wheels, and management; however, they are most unsuitable for both 1U CubeSats and asteroid surfaces. Therefore, a new mobility mode based on hopping needs to be developed. The system must fit within 0.2U with a mass of under 200 grams based on volume and mass budgeting of the entire robot. Additional mass and volume can be recovered if the hopping system also provides attitude control, negating additional control actuators during the hop for safe landing.

## **1.c: Significance of the Project**

Two enabling technologies are developed for the CubeSat class AMIGO hopping robot. Hopping is enabled by a high-level path planning algorithm developed by using a stereo camera that outputs both color images and a depth map for obstruction detection. The depth map allows for objects and adverse terrain to be detected and avoided for safer mobility. The surface boulders present difficulties in both line of site to other areas of the asteroid and in landing safely. These large obstructions and dramatic topology of asteroids reduces the robot's visibility range and navigating around them provides new scenes to examine. The boulders should also be avoided when hopping such that they do not damage the robot or cause it to tip over to a state where data cannot be collected. This idea can be extended to feature detection so objects and areas of interest can be purposefully studied. Imaging from these new locations and headings can be used to construct surface level maps of the terrain and gather information on boulder distribution. The avoidance algorithm is evaluated on a test model of AMIGO with representative avionics and structure by hopping multiple times to avoid obstacles.

The other technology is a micropropulsion system based on cold-gas and microelectromechanical systems (MEMS) technology to provide both lift-off hopping actuation and 2-axis attitude control during a quasi-ballistic, open loop trajectory to a target destination. Hopping from the propulsion system allows the robot to traverse the rough terrain to an area deemed interesting or safe from the hop selection algorithm.

An array of individually actuated micro-nozzles provides thrust for hopping and coarse attitude control. These nozzles are designed with microfluidic corrections to traditional isentropic nozzle analysis to predict losses. A particle swarm code is used to optimize the nozzle design and evaluated in 2D Computational Fluid Dynamics (CFD) simulations. The propellant is stored in a solid phase to increase the system's density specific impulse and sublimates under the vacuum ambient pressure. The propellant's sublimated vapor is used as the working fluid and the chamber pressure is controlled by heating elements. This produces much lower storage pressures than a conventional cold gas system and increases system reliability and safety. In this scheme, the storage chamber acts as a gas generator. Other components to be miniaturized include a main sealant valve for long term storage and individual actuation valves utilizing piezoelectric actuation.

## 1.d: Scope of the Thesis and Outline

The majority of this work is dedicated to the development of a micro-propulsion system for safety and efficiency. The use of sublimate-stored propellant negates the need for highly pressurized gas storage, leading to a much more lightweight and dependable system. The exploration of safe, alternative propulsive chemicals and low operating pressures enables rapid development in a university setting with less stringent safety requirements than other systems with more energetic and toxic materials. A general 3D path planning method is devised to efficiently use this hopping system for obstacle avoidance on an asteroid's surface. Development of the technologies presented will enhance a future class of asteroid surface explorers to answer some of the pressing questions in planetary science.

In *Chapter 2: Asteroid Exploration and Mobility*, the rationale for asteroid exploration is explored. The chapter is heavily influenced by findings in the most recent *Planetary Science Decadal Survey* to detail why asteroid exploration is important, such as enabling larger missions to land on previously uncharacterized surfaces, advancements in in-situ resource utilization, and proto-solar system history. Although one small robot has limited capabilities in terms of scientific significance, the outlining of desired information constrains the sorts of sensors needed on board and drives the system level design of AMIGO. The chapter ends by exploring some of the potential methods of mobility actuation with ideas drawn and lessons learned from a combination of successful and proposed asteroid hoppers.

*Chapter 3: AMIGO* focuses on the design and implementation of an AMIGO robot. After highlighting the developments in the CubeSat class of satellites, the compact design of systems and concept of operations is shown. Significantly, the path planning algorithm using stereo imaging is developed. This enables AMIGO to hop to multiple locations in safe schemes for extended exploration and robust science data.

The propulsion system development is detailed in *Chapter 4: Sublimate Regenerative Cold Gas System and Micronozzle Design*. Of significance is the progress in micronozzle design with corrections to traditional isentropic analysis and optimization through particle swarms. The overall workings of a novel sublimate regenerative propulsion system is explained. Computational fluid dynamics analysis shows the viability of these micronozzles with exploration of methods on how to fabricate the nozzles.

The control of these nozzles is done by two sets of microvalves whose design is shown in *Chapter 5: Valve Designs*. The downstream valves control individual nozzle actuation with rapid speed and low sealing force. The design is based on cantilever bimorph piezoelectric actuation from a 50 V supply, easily obtainable on CubeSat power systems. These valves allow for a control system to either open all nozzle flows for high forces to lift the robot off the surface or for coarse attitude control during their hops. The upstream valve provides long-term sealing as the time from storage to usage of these robots could be years. They also use piezoelectric elements, but as a diaphragm for low leak rates and high sealing forces.

The propulsion system is shown to fit into the concept of operations in *Chapter 6: Control System for Hopping, Attitude Control, and Up-Righting*. Three mobility modes are designed for that will be encountered. Firstly, an overview of using a single shot method to solve Lambert's orbital boundary value problem for excursion planning. Then, a sliding mode controller is

developed for the saturated attitude control regimes from the bottom mounted thrusters. Lastly, a scheme for up-righting the robot is shown should it land on its side.

## 2. Asteroid Exploration and Mobility

In this chapter, the importance of further asteroid exploration and surface investigations is needed. The focus is on smaller asteroids that cannot be extensively characterized by Earth based observation, such as 101955 *Bennu*. Asteroids can answer many questions on planetary formation, early solar system composition, chemical distribution, and more.

Since the launch of *Galileo* in 1989, There have been 6 successful flyby spacecraft and 3 successful orbiting spacecraft to small solar system bodies. To compliment larger orbiter type spacecraft, an accompaniment of smaller surface landers is used for measurements not capable from off the surface. The focus for science goals pertain to capabilities of these small form factor, distributed robots. Various forms of mobility enable these micro-robots to collect more robust science data at multiple locations. The motivation behind asteroid surface hoppers is explored.

## 2.a: Science Rationale and Traceability Matrix

The science and origins of asteroids is deemed high priority in the *Planetary Science Decadal Survey*. Two of the main questions from the Decadal Survey pertain to what the “initial stages, conditions, and processes of solar system formation and the nature of the interstellar matter” that was present in the protoplanetary disk, as well as determining the “primordial sources for organic matter” [2.1]. Major scientific goals for the study of planetesimals are to decipher geological processes in SSSBs not determinable from investigation via in situ experimentation, and to understand how planetesimals contribute to the formation of planets.

Ground based observations are not sufficient to examine SSSBs, as they are only able to measure what is on the surface of the body; however, in situ analysis allows for further, close up investigation as to the surface characteristics and the inner composition of the body. The four sub-categories of lander missions would be in solar system and asteroidal science, planning for future human mission, in-situ resource utilization, and defense from impacts.

Scientific investigations can be augmented by both robotic and manned missions. Akin to the Apollo missions, human missions would provide real-time decision making for more effective in-situ geological experiments and sample collection. Human missions would be limited to asteroids with sufficient safety, considering elements such as gravity, surface roughness, and value of potential science data to be collected.

Robotic missions would undoubtedly precede manned missions to targets of interest, partially to assess the safety of the location. Per the Planetary Science Decadal Survey, manned and robotic missions have their own distinct overarching goals; human missions focus on health, safety and practicality while robotic missions are driven by pure science collection [2.1]. A potential route for the synergy between man and machine would be some orbiter spacecraft with deployable landers to assess the asteroid, followed by humans landing on the same asteroid to exploit the existing infrastructure.

Primitive bodies, including asteroids, Kuiper Belt Objects (KBOs), and Oort Cloud objects, remain intact and contain information of the proto-solar system [2.2]. The internal composition of some of these bodies, shielded from stellar radiation and evolutionary processes, is of pre-solar grains reflective of the solar system’s early composition. The Stardust comet sample return mission showed low abundance of expected materials, signaling a need for further investigation of the internals of the small solar system bodies [2.1]. KBOs, which largely resemble the early formation composition of the gas giants, and Oort cloud objects are the most pristine samples of solar system development but remain quite distant and challenging to get to. The close-by asteroids, however, are representative of the inner composition of planetesimals. They provide insight into concepts such as accretion, compound formation, and differentiation whereby heavier compounds are separated towards the gravitational center of the body. Further insight to the formation processes relies on knowledge of bulk chemistry and internal structure [2.1]. This can partly be accomplished by micro-imagers and seismic sensing networks.

It is currently theorized that accretion of planetesimals from smaller bodies occurred rapidly in the inner solar system, with larger planets forming from collisions of these bodies [2.3]. The remnant SSSBs would go on to partake in the conjectured Late Heavy Bombardment after planetary gravitational effects disrupted their orbits, evidenced in cratering in the Moon, Mars, and other bodies. This high influx of material could have significantly altered the forming planets’

composition, atmospheres, and water content. Assessing the volatiles contained within the primitive bodies could show if and what types of asteroids deposited such components. This would also impact the evidence for the Nice model of planetary migration, in which the larger planets formed further out and drifted inwards, disrupting KBOs rich in volatiles [2.4].

Two of the main science goals for visiting SSSBs is to learn how they coalesce to form planets and organic life, and to obtain the record of material evolution throughout the solar system's lifespan [2.1].

Asteroids are considered to be primitive bodies that contain a record of the physical conditions and how cosmic chemicals have been altered in the solar system. By studying the "time capsules," conditions of the proto-solar system can be constrained to better understand formation processes and material abundance. They can also provide context to how organic matter formed and potentially led to biogenesis. The least affected grains of material would be inside the asteroid's surface, shielded from destruction and perturbation from collisions, solar radiation, etc. It is possible that some of these samples may be pre-solar grains, material that has not undergone evolutionary processes since before the nebular cloud collapsed to form the Sun and other bodies in the solar system.

Specific objectives from the Decadal Survey include to be studied [2.1]

- Understand pre-solar processes recorded in the materials of primitive bodies.
- Study condensation, accretion, and other formative processes in the solar nebula.
- Determine the effects and timing of secondary processes on the evolution of primitive bodies.
- Assess the nature and chronology of planetesimal differentiation.

Some of these specific goals can be completed through rapidly advancing and miniaturizing technology, such as microscopes and seismic sensors. This opens the door for microspacecraft to complete science objectives rather than relying solely on large scale spacecraft. A summary of questions needed to be answered through in-situ measurements are listed in Table 2.1.

Larger asteroids that have differentiated into distinct layers with a crust, mantle, and core provide a more readily accessible sample size to learn of planetary differentiation processes. These smaller bodies are better to study than planets for differentiation because the distinct layers are more easily reachable. For example, coring would require much smaller drilling equipment and a network of seismic sensors can provide global coverage with less coordination. Information to be gained includes elemental distribution within the different phases, isotope dating for length of formation processes, and general hypothesis testing of planetesimal differentiation [2.1]. Some important questions:

Indispensable to furthering astrobiology, the composition, origin, and distribution of organic matter and volatiles must be understood. Inner solar system objects are depleted of volatiles, either due to closer proximity to the Sun or from a systematic lack of the material during their formation. Certain samples of simple organic matter have been analyzed, but larger, more complex compounds remain unresolved. The Spitzer Space Telescope has worked to compare organic matter found in asteroids and comets to better constrain the distribution, timeline, and evolution of organic matter in the solar system [2.5]. To constrain the origin of an asteroid, measurements

of density, dynamical properties, and isotopic compositions are used for high level assessment [2.6]. The most likely method to determine a body's origin is in its composition, as orbit characteristics can vary wildly over time and bulk density sheds no light on what the body is made of. Understanding chemical distribution of these primitive bodies with respect to when and where they formed will show the overall distribution of molecules in the presolar cloud.

It is becoming ever clearer that planet formation occurred by the combination of smaller planetesimals through collisions and mergers. Current asteroids and primitive bodies provide some constraints for model creation, such as orbital parameters and size distribution. Radiogenic isotope analysis constrains the timing of planetoid evolution and combination. Each planet formed in some "feeding zone", a region in the accretion disk where a great deal of material coalesced into a gravitationally dominant body. There is also debate on if asteroids formed closer to larger planets and were flung to the inner solar system or if they formed more closely to their current positions. The lack of water in the latter model would be explained by Al decay heating the ice and forming hydrated olivine and pyroxene, whereas ice would've been melted by close approach of the sun in the former distribution model [2.7]. Some important questions remaining are:

A more dramatic reason for advancing asteroid research is for planetary protection and defense. Asteroids have struck the Earth throughout its almost 4.5-billion-year life per geologic records. Most meteors that enter the atmosphere are inconsequential, mostly ablating during descent or landing harmlessly in the ocean. Some, however, can have destructive and lasting impacts. Recently, the 2013 Chelyabinsk meteorite, only 20 meters in size, exploded over Russia and caused 1,500 hundred injuries from a release of energy larger than the Hiroshima nuclear bomb [2.8]. Of course, there was also a much larger asteroid 65 million years ago that is thought to have resulted in the mass extinction of dinosaurs and many other creatures after impacting in the Yucatan region. Part of the defense issue is in detection of asteroids with enough time to implement damage mitigation procedures. The other issue is in what exactly the mitigation procedure would be; if it is decided to explode the asteroid or drill it in half, would that actually work? The first step in devising a plan is to study the internal structure of a range of asteroids to properly characterize the cohesiveness and compliance.

Earth-based telescopes are the primary method to study large populations of asteroids. Per the Decadal Survey, telescopes provide information on physical surface material, bulk characteristics, volatile content, size, and rotation [2.1]. In-situ measurements provide richer data but visiting such large numbers of asteroids would be prohibitively expensive and unnecessary. Of course, before a mission to a primitive body, the object must be discovered, and its orbit/ bulk characteristics well defined for more constrained mission design. However, they do not reveal much on the internal composition and structure of asteroids, nor can they measure with sufficient depth the isotopic composition or fine grain surface detail.

| Topic   | Question  |
|---|---|
| Nature and Chronology of Planetary Differentiation                          | Did asteroid differentiation involve near-complete melting to form magma oceans, or modest partial melting?   |
|   | How did differentiation vary on bodies with large proportion of metal or ices?  |
|   | Were there radial or planetesimal-size limits on differentiation, and were KBOs and comets formed too late to have included significant amounts of live aluminum-26 as a heat source? |
| Primordial Distribution of Volatiles and Organic Matter in the Solar System | What was the proportion of surviving presolar organic matter in the solar nebula, relative to the organic compounds produced locally?   |
|   | What roles did secondary processes and mineral interactions play in the formation of organic molecules?   |
|   | How stable are organic molecules in different space environments?   |
|   | What caused the depletion in volatile elements, relative to chondrites, observed in differentiated asteroids and planets?   |
| How and When Planetesimals were Assembled to Form Planets                   | Are there systematic chemical or isotopic gradients in the solar system, and if so, what do they reveal about accretion?  |
|   | Do we have meteoritic samples of the objects that formed the dominant feedings zones for the innermost planets?   |
|   | How did Earth get its water and other volatiles? What role did icy objects play in the accretion of various planets?  |

Table 2.1: Importance of Asteroid Investigation

Advancement in technology is allowing for spacecraft to take high-resolution images to map out, and touchdown on their surfaces (e.g., *NEAR*, *Deep Impact*, *Hayabusa I and II*, *OSIRIS-REx*). The vast majority of asteroid surfaces seem to be covered in regolith based on thermal and visual images. Understanding the dynamics of asteroids, their granular materials, in their native small-body gravitational environment ( $\sim 0.0001 g_{\text{Earth}}$ ), is vital for the correct interpretation of their surface geology [2.9]. This requires prolonged surface exploration of the asteroid surface using a lander and is the next incremental step in technology compared to current missions such as OSIRIS-REx and what was exploited by Hayabusa II.

Sample return missions require a container that can withstand Earth re-entry with velocities in excess of 13 km/s. Missions to more distant objects, such as the Trojans or KBOs could take in excess of 10-15 years of flight time plus the return trajectory, with free return missions taking even longer.

A proposed *Asteroid Interior Composition Mission* was to collect more information on the internal structure of main belt asteroids with a secondary goal of characterizing surface chemistry. To sample the interior without massive coring machinery, it was proposed to use an explosive charge to excavate the surface with a network of seismic sensors to peer deeper into the asteroid's layers without blowing the whole body apart.

In conjunction with relevant question asteroids can answer and the capabilities of small measurement systems for CubeSats discussed in *Chapter 3*, a science traceability matrix is shown in Table 2.2.

| <b>Science Objective</b>    | <b>Measurement Objective</b>                                     | <b>Payload</b>                               | <b>Investigation</b>  |
|-----------------------------|--|--|---|
| Stereo imaging              | Human-scale panoramic imaging for geology and astronaut training | Stereo camera with top-mounted vantage point | Panoramas and movies from various   |
|                             | Surface mapping  | Stereo camera                                | Diversity of various sized surface features   |
| Surface micro-imaging       | Micro-imaging of fine geologic structures                        | Micro-camera                                 | Close-up images of rocks and grains for textural analysis and meteorite comparison  |
|                             | Imaging of ongoing surface thermal fatigue                       | Stereo camera, micro-camera                  | Observe potential thermal effects over multiple diurnal cycles from constant location   |
| Seismology                  | Global seismology  | IMU, seismic sensor, piezo vibrator          | Detection of ground movement induced by boulder extraction or other mission activity using direct sensing with before/after imaging |
|                             | Determine local surface hardness and compliance                  | IMU, camera, piezo vibrator                  | Measure acceleration from multiple hops on same location, imaging after vibrating surface   |
| Electric field measurements | Characterize electric fields and dust                            | Mylar shell, solar panels, piezo vibrator    | Measure dust obfuscation of photovoltaics, vibrational dislodging of dust, voltage from ground to 1-m height                        |

Table 2.2: Science Traceability Matrix

The Space and Terrestrial Robotic Exploration Lab (Space TREx) at the University of Arizona has proposed the Asteroid Mobile Imager and Geologic Observer (AMIGO) that will be deployed at multiple locations around the surfaces of small bodies and provide stereo imaging from vantage points ~1 m above the surface, close-up geologic imaging, and seismic sensing. The payload consists of three or more 1U CubeSats that each contains an inflatable and on-board propulsion system to perform surface hopping. For the AMIGO lander, there are four science goals:

1. Stereo imaging for large-scale surface characteristics.
2. Micro-imaging for fine-grain surface science.
3. Seismology for internal structure and cohesion.
4. Measure the electric characteristics of surface regolith and the monolithic asteroid structure.

Each of these science goals seeks to fill a current knowledge gap in the characteristics of asteroids. For example, the proposed NASA Asteroid Redirect Mission was to retrieve a boulder from the surface of a near Earth asteroid and return the sample for further analysis [2.10]. Currently, the dynamics of how to extract a boulder from the surface of an asteroid is an open problem. The issue is as fundamental as Newton's Third Law; if one aims to pull a three-ton boulder from the asteroid surface, the spacecraft must exert three tons on the asteroid. Will the asteroid and boulder have enough cohesive strength to not completely fall apart? Seismic sensors and close-up geologic sensors will provide this information. Each science objective in Table 2.2 can contribute to answering the questions in Table 2.1.

The characterization of surface regolith of asteroids is vital to the success of future lander missions and the further understanding of the composition of asteroids. For instance, it is theorized that planetesimals often impacted with each other and either obliterated into fine dust and small clumps or aggregated together. In either case, fine grains are created. For intact planetesimals, this dust accreted to the surface and became the surface regolith. However, that regolith may not have the same compositions as the asteroid itself due to a combination of multiple meteoric impact events. In situ analysis will aid in the understanding of the surface of asteroids in this regard. A large reason for the concept of AMIGO is to add to the current base of knowledge for the surface characteristics of asteroids for use in future lander missions. The familiarity with asteroid surfaces gained by lower cost missions will lay the foundation for, say, a Discovery class mission to be more successful due to limiting the unknowns in the geology dynamics of asteroids. It is also important to have multiple scales of measurements. It will be much easier for fine-grain details to be discerned from these surface landers than from the mother spacecraft as they can be essentially in direct contact. A continuum of data could thus be created from combining large-scale surface features collected by the orbiter and smaller details from the landers.

## 2.b: Literature Review: Mobility Actuation and Small Body Surface Explorers

There are a few methods to obtain mobility across an asteroid's surface: wheeled rovers, internally actuated hops, mechanical devices, micro-gripping soft-robots, and thrusters. Mobility is a non-trivial issue because of the unexpectedly rough surfaces and boulder fields on asteroids.

Traditional rovers are well suited to large bodies, such as the Moon and Mars, where local gravity is comparable to the Earth's. Wheels are able to turn and overcome small bumps with gravity holding the robot to the surface; however, in milli- and micro-gravity environments, the rotation of a wheel will impart a large enough delta-v to lift the robot off the surface and potentially into an escape trajectory [2.11]. The small traction capable requires very slow movement on the order of mms/s, like that envisioned on the MUSES-CN rover (Figure 2.1). There is also a great risk of the rover sticking in the potentially deep surface regolith or for the wheels to lose contact and control.

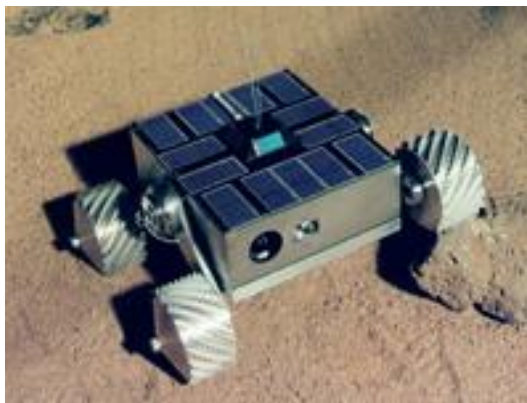


Figure 2.1: MUSES-CN Rover

Internally actuated devices typically rely on spinning up and braking a reaction wheel. A benefit to this system is the actuators are shielded from the surface regolith, extending their lifetime and limiting the probability of failure. The dynamics of the surface regolith must be well understood for accurate prediction of hopping dynamics, as the force transferred to the robot is dependent on robot-regolith interaction. Hedgehog is one such development by NASA JPL and Stanford, with three flywheels and external spikes to tumble for short distances and hop for more distant targets [2.12, 2.13]. Another is the Gyrover that contains spinning flywheels attached to a two-link manipulator [2.14]. A recent successful example of this concept is JAXA's MINERVA-II 1A and 1B landers, as they landed and hopped around the surface of Ryugu and transmitted images (Figure 2.2). The MINERVA rovers utilize a cylindrical shaped body so only two torquers are required for full hopping control [2.15]. Included on-board the Hayabusa-II mission is MASCOT, a larger internally actuated rover with capabilities for fine-scale regolith imaging, radiometry, infrared spectrometry, and magnetometry [2.16]. Tumbling methods tend to not have fine control to land in specific locations and in a certain desired orientation. They do, however, permit large traverses with simple actuation for wide-range surface exploration.



Figure 2.2: Ryugu Surface

One type of mechanical hopping is by the use of a spring mechanism, a direct reactive force pushing the robot from the surface. The Canadian Space Agency developed the Micro-hopper for traversing Martian terrain, though with a limitation of only one hop per day due to the time to reform the shape memory alloy [2.17]. Another technique for hopping developed by *Plante and Dubowsky* at MIT utilize Polymer Actuator Membranes (PAM) to load a spring. The system is only 18 grams and can enable hopping of Microbots with a mass of 100 grams up to a 1 m [2.18].

Another mechanically actuated example is SPIKE, a 75 kg spacecraft-hopper that embeds science instruments into regolith via a boom connected to the robot in free fall [2.19]. Vibrating the boom causes cohesion with regolith to be broken and the spacecraft is free to hop to another location. Again, mechanical hoppers have a reliance on surface characteristics, which are not well constrained and vary asteroid to asteroid.

Area of Effect Soft-bots (AoES) are being developed by the ORCCA Lab at CU Boulder, soft robots that gain mobility by gripping the surface of the asteroid with large, flexible membranes [2.20]. HASEL actuators are used to manipulate the membrane which then adheres to the surface of the asteroid through cohesive forces. The robots are aimed to be capable of hopping into the asteroid's orbit from the surface and using the large surface area as attitude control from solar radiation pressure, like an active solar sail.

Recently, it has been discovered that the previously thought inert asteroid surfaces are dynamic, with multiple ejection events imparting escape velocity to centimeter-sized objects on asteroid Bennu [2.21]. A potential explanation is volatile plumes as the asteroid heats up on one side. If plumes are the cause, they could potentially be used as a "free ride" hopping mechanism. The difficulties presented, however, are substantial. The momentum imparted will need to be more well constrained so as to not reach escape velocity like many of the particles have, and the robot would have to be well placed to not tumble if on the edge of the plume or even in the right place when the plume erupts.

Thrusters allow for mobility independent of surface characteristics, though exhaust may cause interference with the electrically charged, organic regolith and kick up dust in the process. Sphere-

X is a spherical robot that hops using chemical propulsion and is intended for exploring in higher gravity of  $1.0 \text{ m/s}^2$  and higher [2.22-2.25]. This system, however, relies on reaction wheels to provide attitude control, as the thruster is used only for launching the robot. A thruster with multiple nozzles is required for pointing authority for smaller robots with less volume and mass for angular momentum transfer devices.

### **3. AMIGO**

The expanding role of nano-landers as science tools opens the door to asteroidal investigations previously untenable by flagship missions. Robust and less expensive robots can land on the surface of asteroids and perform important data collection on fine scales. This chapter explores the use of small space robots and the development of a CubeSat class asteroid surface hopper.

### 3.a: CubeSats

With the goal of reducing mission and development costs while performing significant science and observational objectives, nanosatellites are in increasing development. Nanosatellites are usually between 1-10 kg, much smaller than traditional large-scale missions that can easily be over 1,000 kg. Though “expendable” might be a misnomer, a major advantage of lower-cost and diversified satellites is that the loss of one system is not as devastating as it is for the traditional satellite class. Smaller satellites tend to have intentionally lesser capabilities as a single entity but there is a current drive to design constellations and swarms such that the whole is greater than the sum of its parts. The reduction of scope for each satellite and smaller size enables lower complexity and costs for both manufacturing and launching nanosatellites.

Specifically, the CubeSat has gained increased use in real science missions. CubeSats were originally designed as an education tool for both students and technology demonstrations [3.1]. They existed largely in the academic sphere as a way to test and develop new space technologies and concepts that would have been out of reach to develop larger platforms. CubeSats have a standard size of 1.33 kg and 10x10x10 cm profile as a 1 Unit (1 U) satellite and multiple units are combined for larger missions, notably 3, 6, and 12 U form factors. CubeSats have much faster development schedules and lower costs than their traditional counterparts [3.2]. With their expanded use and standardization, CubeSats are deployed with much faster turnarounds and have an ever-expanding base of COTS components. Missions have applications to three main areas: technology demonstration and development, mission operations and defense, and science advancement.

CubeSats are increasingly intensifying their scientific profile, from Earth observations to interplanetary missions [3.3]. Near Earth Asteroids, planets, and icy moons have seen an uptick of interest from CubeSat teams. The possibility of CubeSats beyond Earth’s sphere of influence has recently been shown with the MarCO twin satellites, as they were successful in their primary mission and displayed more miniaturized technology concepts [3.4]. MarCO was primarily a mission operations mission that served as a communication relay but had the secondary goal of demonstrating materials and equipment that can be used in such small satellites. In an effort to negate the need to miniaturize complex propulsion systems, solar sails have been demonstrated to be an effective means to guide CubeSats to their target destination. The Planetary Society’s Lightsail 2 has shown the use of solar sails with extensions to deep space nanosats with no reliance on a larger spacecraft for delivery [3.5]. CubeSats can also have a profound impact on planetary science without even leaving Earth’s orbit; in the case of AOSAT, on-orbit centrifuge technology can shed light on asteroid dust dynamics and cohesion [3.6].

The major inhibits to extending CubeSats beyond GEO has been in surviving the harsh space environments and development of miniaturized propulsion systems. Radiation can cause serious degradation in solar cells and electrical components, usually requiring radiation hardened hardware or thicker and carefully designed shielding for long term storage and operation [3.7]. Propulsion systems are often too heavy and bulky for the CubeSat platform [3.8]. Long range communication is also an issue as larger, more powerful and efficient antennas do not conform to the nanosatellite envelope.

Miniaturization and maturation of space technology has enabled nanosatellites to conduct science missions. By either diversifying into a swarm or accompanying larger satellites, CubeSats are a viable platform to explore small solar system bodies.

### 3.b: AMIGO Concept

Combining nano landers with larger flagship missions increases the science return of asteroid missions with lower overall costs. Putting large and expansive main spacecraft at risk of damage by landing or touch and go missions is easily avoided by deploying surface explorers to perform more hazardous endeavors.

The Asteroid Mobile Imager and Geologic Observer (AMIGO) (Figure 3.1) is a conceptual 1U CubeSat to explore the surface after deployment from a mother spacecraft in orbit or station keeping around the target body. The 10x10x10 cm chassis has the capacity to hold avionics, micro-propulsion system, a deployable inflatable structure, a stereo camera, a micro camera, and a seismic sensor. The inflatable structure deploys to up to 1 meter in diameter with the stereo camera mounted on top.

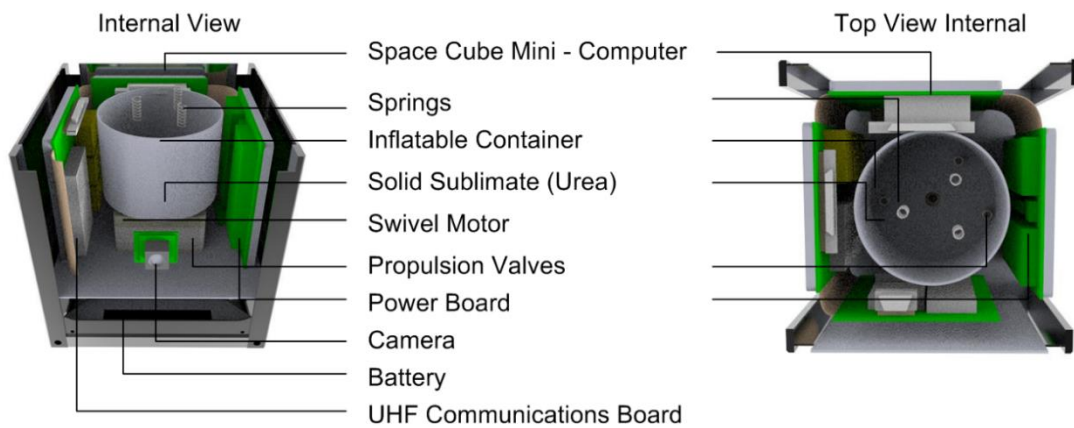


Figure 3.1: AMIGO Internals

Each AMIGO is deployed from a mother spacecraft (Figure 3.2). During descent, the robot inflates from its stowed 1U state. The bottom-heavy design facilitates upright landing, though the inflatable is designed to withstand the slow  $\sim 15$  cm/s impacts. Upon landing, initial context is determined for where the robot is on the surface. This is done by both on board imaging and tracking from the mother. The inflatable portion provides a tracking target, as smaller robots may not be large enough to be tracked. From there, the science mission is conducted.

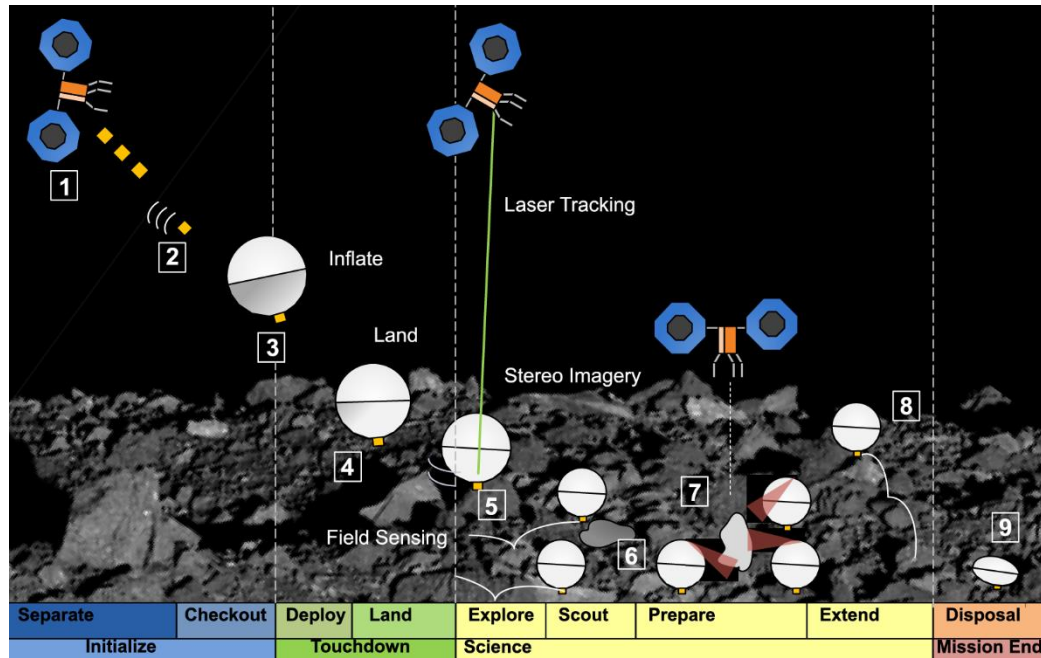


Figure 3.2: AMIGO ConOps

The hopping capability of the robot allows for selective and dense sampling on an asteroid's surface. This contrasts to other landing systems that can only sample data at a single location. Controlled hops allow for accurate landing at specific targets of interest, e.g. curious surface features or areas of dynamic change. For example, some areas of the asteroid may be more active and provide much more insight to the internal characteristics and composition than a dormant area. Another use would be in selecting the higher albedo locations as observed by the mother spacecraft, as they are indicative of recent churning activity to expose the internal material compared to darker areas long covered by regolith [3.9]. A combination of longer excursions and short hops empowers large-scale surface exploration and accuracy when accounting for the lumpy gravity fields of the small bodies.

For the AMIGO lander, there are four science goals:

1. Stereo imaging for large-scale surface characteristics.
2. Micro-imaging for fine-grain surface science.
3. Seismology for internal structure and cohesion.
4. Measure the electric characteristics of surface regolith and the monolithic asteroid structure.

The stereo camera provides context imaging and surface mapping/ path planning capability. The context of where the robot is allows for the robot to determine points of interest on the asteroid surface and potential locations to traverse to (Figures 3.3, 3.4). The depth mapping capability of stereo imaging allows for path planning for the robot to hop to multiple locations for robust sampling. The depth map allows for objects and adverse terrain to be detected and avoided for safer mobility. The surface boulders present difficulties in both line of sight to other areas of the asteroid and in landing safely. These large obstructions and dramatic topology of asteroids reduces the

robot's visibility range and navigating around them provides new scenes to examine. The boulders should also be avoided when hopping such that they do not damage the robot or cause it to tip over to a state where data cannot be collected. Imaging from these new locations and headings can be used to construct surface level maps of the terrain and gather information on boulder distribution. The stereo camera also provides imaging for the large-scale surface structure, akin to Figure 2.2.



Figure 3.3: AMIGO at Bottom of Hop



Figure 3.4: AMIGO at Top of Hop

The inflatable structure is a critical multi-functional device (Figure 3.5). By mounting the stereo camera on top, less dust will cling to the lens for clearer and longer-term imaging while providing a larger range of viewing. The inflatable also serves as an antenna to communicate with the mother spacecraft for science data and positioning [3.10]. The inflatable is visible from the overhead orbiter for positioning updates and reducing the possibility of losing the robot in the

potentially deep regolith. Flexible photovoltaic cells could be interlaced into the thin-film structure, allowing for energy collection to extend mission lifetime with lighter batteries. Sublimates will be used to inflate the structure to hundreds of Pascals and replenish any gas that may have leaked during the robot's lifespan.

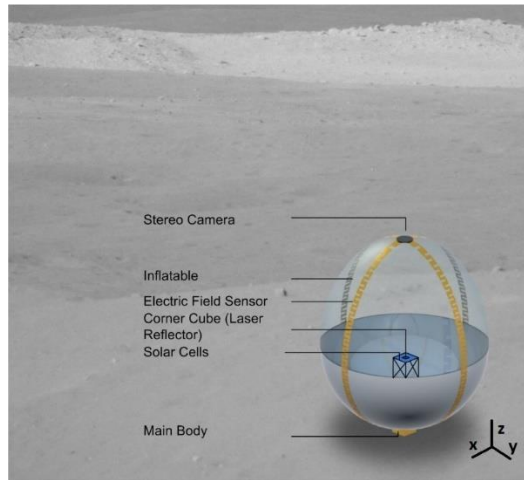


Figure 3.5: AMIGO on Surface

A bottom mounted micro-imager fulfills two of the mission's measurement objectives. Primarily to be studied is the fine-grain structure of the surface regolith and "boulders." Part of the science collected is the structure of the asteroid in comparison to meteorites found on Earth. This investigation seeks to answer if meteorites are smaller fragments of broken-up asteroids. The other objective of this camera is to detect active surface thermal fatigue from multiple diurnal cycles. As the asteroid rotates and experiences sun light and shade, there is potential for thermal fatigue and outgassing of volatiles underneath the surface that will be characterized.

The scope of AMIGO's mission and capabilities should be noted. Firstly, hops are currently an open loop with no way to feedback information for more controlled hops. The robot relies on an IMU which does accumulate error and the mothercraft to track its position, but that is only possible when the mothercraft is overhead. The robot also should not hop to a location it cannot see as that would put the robot at risk of landing in an unknown topography. The only other possibility would be mapping from adjacent robots operating as a swarm, but that would limit the range of the surface covered at any one time by the robots. During a hop, AMIGO is not capable of looking down, as the stereo camera only looks in one direction and any bottom mounted micro-imager could not obtain details when far away from the surface. Lastly, AMIGO's useful life will be limited by power generation and propellant remaining. Even after all propellant has been expelled and the robot can no longer hop, it can still obtain science data as a stationary node.

### 3.c: Engineering Development Model and Testing

The primary purpose of the engineering model is to test path planning and hopping algorithms. As the gravity environment on a small asteroid is much lower than that experienced on the Earth, a simulation of the microgravity environment is required to accurately assess the robot's dynamics and hopping control.

Three methods were considered for microgravity simulation: tethering, parabolic flights, and helium balloons. Tethering the robot requires significant infrastructure and dynamics analysis to obtain meaningful results. Reduced gravity aircraft in a parabolic flight are both expensive and allow for only short, usually 25 second weightless tests. These short durations are not long enough to complete a full hop, let alone multiple for mapping purposes.

Helium balloons provide a buoyant force to counteract some of the gravitational force experienced by the test model. The mass that can be lifted is equal to the mass of the displaced air by the balloon,

$$m_{buoy} = \rho_{air}V \quad (3.1)$$

Where  $\rho_{air}$  is the density of air and  $V$  is the volume of the balloon. In taking account of the mass of the helium in the balloon and the mass of the balloon, the mass that can be lifted by the helium balloon is

$$m_{lift} = m_{buoy} - m_{He} - m_{bal} \quad (3.2)$$

Where  $m_{He}$  is the mass of helium in the balloon,

$$m_{He} = \rho_{He}V \quad (3.3)$$

And  $m_{bal}$  is the mass of the balloon. The buoyancy of the helium balloon should counteract the majority of the weight from the robot. The balloon also augments the inflatable device on AMIGO allowing for a top-mounted stereo camera. From available off the shelf balloons, a 21" mylar spheroid is selected. This is the largest balloon found with a spherical shape with axisymmetric properties.

With a density of air  $\rho_{air} = 1.225 \text{ kg/m}^3$  of helium  $\rho_{He} = 0.179 \text{ kg/m}^3$ , a spherical volume of  $V = \sim 0.0795 \text{ m}^3$ , and mass of the balloon 22 g, the mass that can be lifted by the balloon is  $m_{lift} = 61.1 \text{ g}$ .

Utilizing a drone would also negate gravitational forces should the balloon not provide enough lifting force. A quadcopter would simulate the actuation modes of the bottom mounted thruster chip from Figure 4.1.

This robot is designed to only use the basic components to simulate hopping and path planning. The included non-structural components are listed in Table 3.1.

| Component            |        | Use                           | Mass (g) | Cost     |
|----------------------|--------|-------------------------------|----------|----------|
| Raspberry Pi Zero W  |        | Main Computer                 | 9.3      | \$10.00  |
| eYs3D Camera         | Stereo | Path Planning                 | 8        | \$179.99 |
| Crazyflie 2.1        |        | Hopping Actuation             | 18       | \$195.00 |
| Flow v2              |        | Motion sensing                | 1.6      | \$45.00  |
| 1200 mAh Battery     | LiPo   | Power Supply                  | 23       | \$9.95   |
| Power Boost Basic    | 500    | Volt and Connection Converter | 8        | \$9.95   |
| USB 3.1 micro A      | b to   | Camera interfacing            | 10       | -        |
| A/Micro USB Cable x2 |        | Power Supply                  | 10       | \$5.90   |
| USB OTG mini hub     |        | Camera and drone comm         | 12       | \$4.95   |

Table 3.1: Components with their Mass and Cost

The Raspberry Pi Zero W (referred to as Pi from here on out) has been selected as the main computer. This computer runs Raspbian OS with a large library for robotic control, mapping, and communication with 512 MB RAM and a 1 GHz processor. During testing, the Pi will be controlled by SSH from another computer, then left to run on its own during runs to simulate an automated robot system. The Pi receives 5 V power from a micro USB cable, interfaces with the stereo camera from another micro USB ports, and communicates with the drone over UART. UART communication negates the need for a powered USB splitter, as the Pi only has one USB port for sensors. This computer offers sufficient connectivity for all required tasks with user friendly development and a low mass.

Powering the Pi and drone is a 1200 mAh Lithium Ion Polymer (LiPo) battery at 3.7 V. The Pi, however, runs at 5 V and has a power receiving circuit over its USB Power in interface. Thus, the Power Boost 500 Basic is used to convert the battery power to a 5 V USB output. A USB A/Micro cable connects the Pi to this Power Boost.

As the propulsion system requires operation in a vacuum, another hopping mechanism which simulates the discretized actuation points is required. This is accomplished by using a quadcopter with the propellers positioned where the thruster nozzles would be on the bottom of the robot's chassis.

The selected drone is the Crazyflie 2.1 from Bitcraze. This drone was selected as it was the only nano-drone with a programmable API. Most other nano-drones are not directly programmable, so all communication and control must be done with an external computer and controller. Other programmable drones are usually much larger, like from Parrot or DJI, which

would negate the usefulness of the helium buoyancy. Communication and power are received over the USB interface.

The chassis simulates the volume constraints of a 1U CubeSat with 10x10x10 cm outer dimensions (Figure 3.6). The chassis must allow housing for avionics, mechanical interfacing with the Crazyflie, and rigid connection to the helium balloon.

In the goal of minimizing the mass of the system to reduce the load on the drone, balsa wood is chosen as the chassis material. Side panels are 2 mm thick and vertical rods are 1x1x9 cm. The remaining cm in height is allocated for the thickness of the top plate, bottom plate, and screws. The side plates and bottom plate are bonded to the vertical rods with the top open for access to avionics. The top plate is screwed in to threaded inserts bonded in the vertical rods to close the chassis.

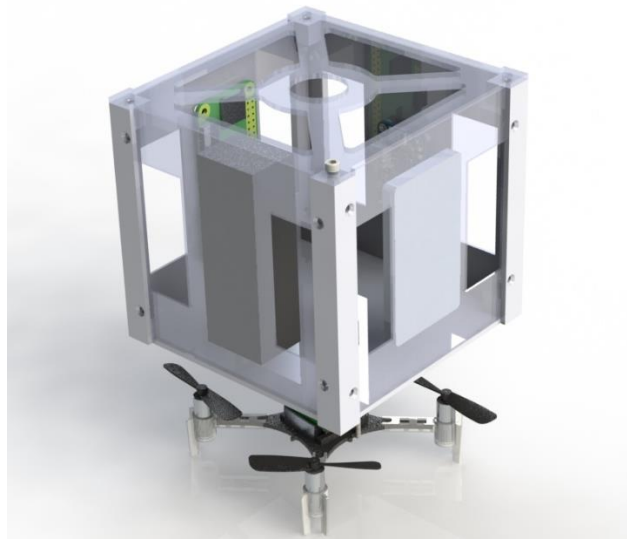


Figure 3.6: Chassis and Drone

Upon inflation, the helium balloon is tied to the corners of the chassis (Figure 3.7). Strings run from one corner, are tied to the balloon nozzle at the top, and connected to the other corner to keep the balloon against the chassis. An unsecured balloon would cause unknowable disturbances in the robot's operation.



Figure 3.7: Test Model with Balloon

The output of the stereo camera is a point cloud, color composite image, and depth map with distances in RGB. The on-board image processing from the camera uses the point cloud to create the depth map. An example scene (Figure 3.8) is used to highlight obstacle detection with objects placed 1 meter (right box), 2 meters (middle box), and 3 meters (left box) from the robot, with the camera placed on top of the chassis of the robot.



Figure 3.8: Color Image of Object Detection

An unprocessed depth map (Figure 3.9) is output from the camera software. Far objects are in blue, while the closest objects are in red and white.

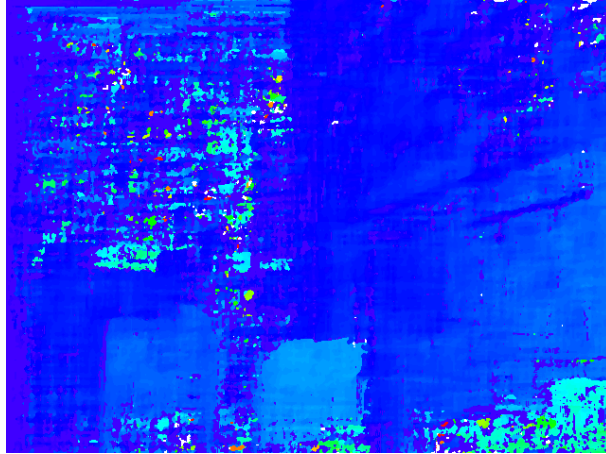


Figure 3.9: Unprocessed Depth Map

The image's depth map needs to be processed to detect viable paths to hop. This is done by first splitting the depth map into varying regions of distance: "Distant", "Medium", and "Close". In this way, objects at various distances can be classified and noise can be cleaned. From this depth map, it is obvious that adverse and uneven lighting causes imperfect depth information.

A range of RGB values for each distance region is defined. A mask is created to filter out areas not in the distance range in OpenCV, a computer vision library. From the depth map in Figure 3.9, each distance field is shown in Figure 3.10.

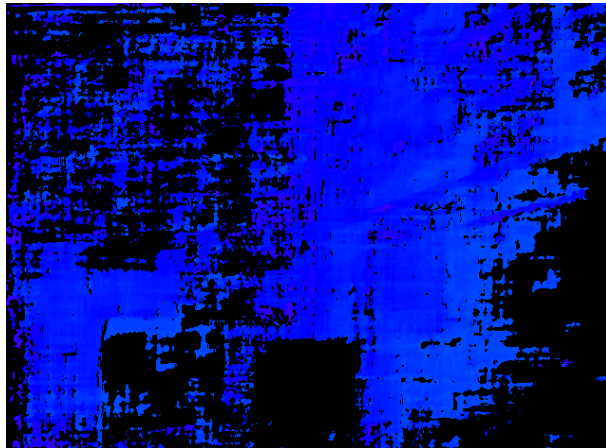


Figure 3.10.a: Distant Field Before Processing

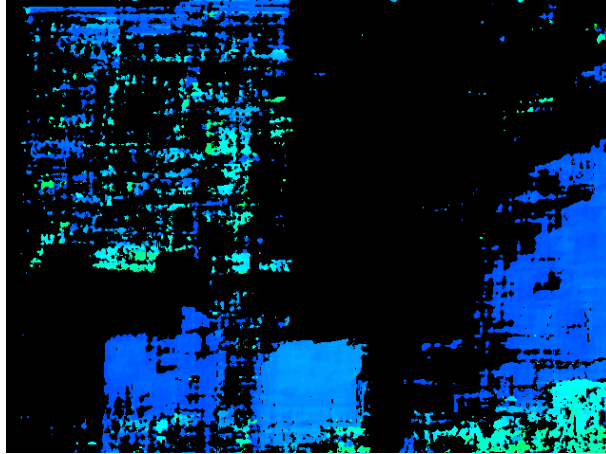


Figure 3.10.b: Medium Field Before Processing

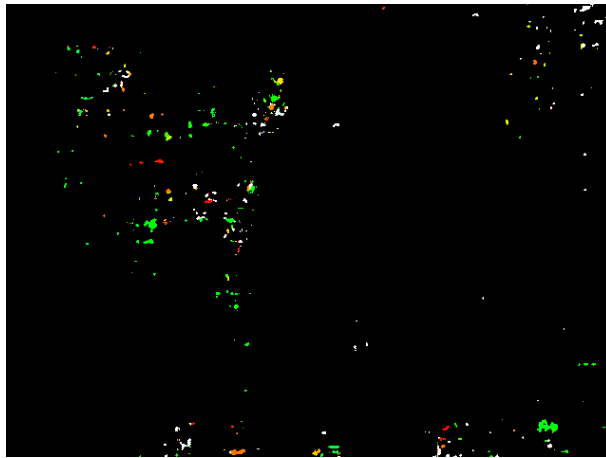


Figure 3.10.c: Close Field Before Processing

Contours area created for each object in each distance region. Contours with a very small area are filtered out as noise and places them in the distant field. This tends to clean the distant region that falsely detects small objects. Following this procedure, the distant and medium fields are shown (Figure 3.11),

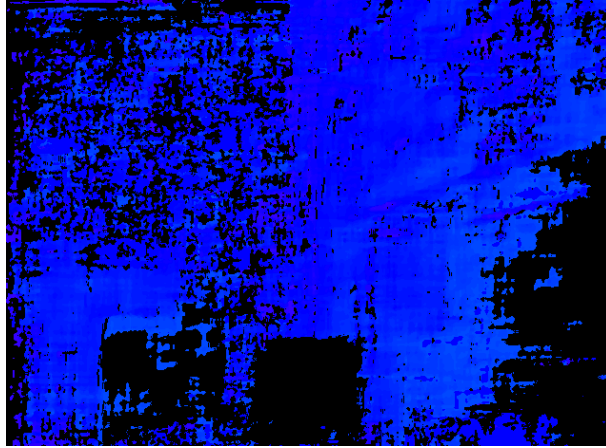


Figure 3.11.a: Distant Field After Processing

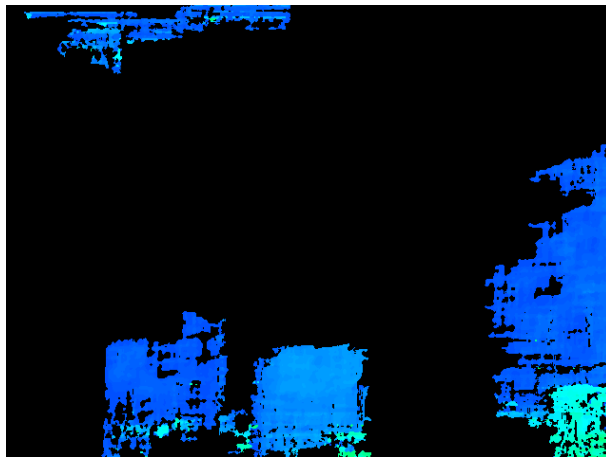


Figure 3.11.b: Medium Field After Processing

From the processed images, each of the three obstructions and a cabinet representing a wall have been detected in the “Medium” field. Once the images have been cleaned and obstructions detected, a hop path can be chosen.

Beginning with the distant field, if there is a large enough region with no obstructions, the robot will hop in that direction. The field is split into 80 “slices” vertically, and each slice is evaluated for an obstruction. The slice is an open region if there are no obstructions. Each open region has its neighboring regions checked if they are open. If enough open regions are next to each other, the middle slice is chosen as a valid slice to hop to. If multiple valid slices are found, one is randomly selected. This reduces the likelihood of the robot turning around and hopping in the direction from which it came.

The robot will hop to a maximum distance such that obstructions not previously detected due to their distance will now be in range. Thus, the robot does not over-hop into an unknown region.

If no path is detected, the “Medium” region is analyzed for a path to hop. If a viable direction is chosen, the robot will hop a shorter distance, so it does not encounter a closer obstruction. If no

path is selected, the robot will lift straight up, yaw 30° and begin the detection process again. In this way, a new scene is analyzed as the stereo camera is not a true 3D point cloud of the robot’s entire surrounding.

The Pi can be used to start the hopping experiment by sending SSH commands over Wi-Fi. This allows for all processes to take place on-board with no external processing required, simulating an autonomous sequence. To minimize changes to the Crazyflie’s firmware architecture, the drone is connected to the Pi via the USB OTG connection for both data and power.

To connect to the drone, the Pi scans for all interfaces and saves the URI of the drone found over USB. As the Flow deck is a motion sensor that integrates x-y movements to obtain the position, errors accumulate that must be reset for each new run. The x-y position is not a true position, but the height is because it uses a range finder.

The Crazyflie is able to receive “set point” commands in a variety of modes: absolute roll-yaw-pitch-thrust, translational velocities and yaw rate, constant height motion, and final position. AMIGO-like quasi-ballistic hops use the velocity set point to simulate an impulsive burn to lift off from the surface. The position is found from the Flow deck to compare accuracy.

These initial velocities are found by a parabolic trajectory to the desired final position. AMIGO uses a single shot algorithm to solve the Lambert Orbital Boundary Value Problem (Equation 3.4) for the irregular, complex gravity fields on small body surfaces.

$$\ddot{r} + 2\omega \times \dot{r} + \omega \times (\omega \times r) + \dot{\omega} \times r = g + d + u \quad (3.4)$$

Where,  $r$  is the position vector,  $\dot{r}$  and  $\ddot{r}$  are the first and second derivative of the position vector,  $\omega$  is the angular velocity vector of the asteroid,  $g$  is the gravitational acceleration,  $d$  is the disturbance acceleration such as SRP and third body perturbations, and  $u$  is the control acceleration. For the test model, a simple parabolic trajectory is used due to lack of disturbing forces encountered at asteroids. Once the dynamics of the model are well known and disturbances (mainly drag and non-rigid effects) are characterized, a full simulation using the single shot method can be used.

A different set point is used for the mode of rotating the robot to a new heading. In this mode, the robot hovers 10 cm above the surface and yaws to its new heading. The hover setpoint is used, with inputs being the desired hover height, yaw rate, and zero velocity in x and y.

Testing is done on a simulated asteroid surface with objects placed in the test area to mimic boulders to avoid. Due to the limited test area, the maximum number of hops is set to three. The position of the robot is logged through the Crazyflie’s Kalman estimation algorithm. Height measurements are absolute, while translation is integrated from sensed motion.

The trajectory of the robot through its three hops is shown in Figure 3.12 as a 3D view, while Figure 3.13 shows an above view with obstacles approximately where they were placed in the real world.

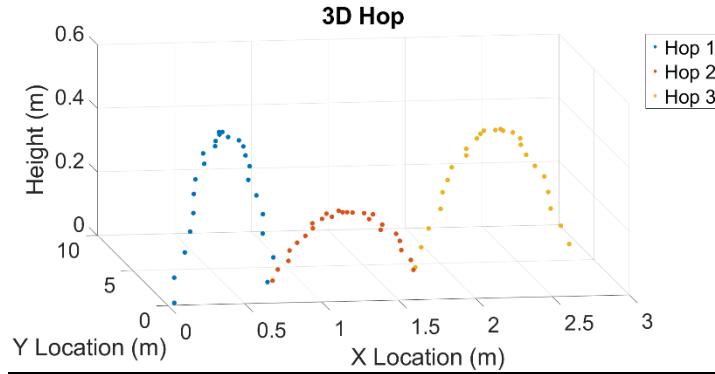


Figure 3.12: 3D View of Consecutive Hops

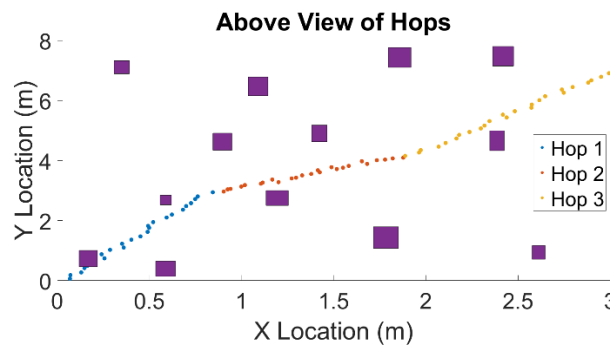


Figure 3.13: Aerial View of Hops

The robot is able to successfully navigate between objects on the ground level. By detecting areas to avoid, the robot hops to safe locations and gains a new vantage point from which to observe. This would correlate to AMIGO hopping from destination to destination and collect science data from a more diverse range.

The first and third hops are to the “Distant” field with an unobstructed path to the set maximum distance to hop. The intermediate hop is to the “Medium” field, where there was no area with sufficient area to hop the maximum allowable distance.

Interestingly, the robot’s first hop path brought the robot very close to an object. As the robot hopped over the top of it, there was no risk of collision. However, more buffers need to be in place to ensure the robot does not come so close to a forbidden region of the obstacle field.

The shakiness in the plots are from two sources: error accumulation (minor) and wobble during flight (major contributor). The use of the helium balloon causes slight disturbances that causes the robot to wobble. This could cause the robot to deviate from its course and bring it to a non-optimal position in the obstacle field.

The robot is successfully able to hop using the slicing method of examining a depth map. By first splitting the depth map into three layers, the “Distant”, “Medium, and “Close” fields, objects

of varying distances can be found and avoided. Each layer is then examined by vertical slices to find open areas.

In searching these open areas as groups, a large enough area to fit the robot through can be found. The algorithm must be updated to ensure the robot does not hop near the edges of objects that disturbances would be sufficient to cause a collision.

Future work will include addition of topography information. Thus far, it has been assumed that there is a flat ground plane that the robot lifts off from and returns to at the same height. On a rough asteroid surface, this is obviously not the case from data gathered by the *Hayabusa-II* and *OSIRIS-Rex* missions.

Another development will be in creating maps of where the robot has explored. Constant feed images and depth maps can be used and stitched together to create a 3D representation of the asteroid surface and obstacles. Currently, snapshots are used when the robot is on the ground to determine the desired hop location, while no images or processing occurs during a hop.

## 4. Sublimate Regenerative Micropropulsion System and Micronozzle Design

The motivation for a mobility system for *AMIGO* has been outlined in both *Chapter 2* and *Chapter 3*. For *AMIGO* to collect science data at various locations, a system to both actuate hops and control authority is required. Multiple types of mobility have been proposed and even successfully implemented.

A propulsion system is deemed necessary to gain mobility on a small asteroid's surface over other methods previously discussed for hopping robots. Rovers are simply non-viable in microgravity environments with rough and unknown terrains. Mechanical systems are also reliant on surface characteristics of which little is known. Although internally actuated hoppers have been used successfully, notable on the *Hayabusa-2* mission, it is desired to not send the robot into a tumble due to dependence on the inflatable structure.

Three main requirements drive the design of the propulsion system: the propulsion system mass must be less than 20% of the total mass of *AMIGO*, the system must occupy a volume of less than 0.2 U and must meet the lift-off thrust and  $\Delta v$  requirements. By discretizing the nozzle into multiple nozzles on the same bottom-mounted thruster chip, attitude control can be gained (Figure 4.1). Each black circle represents an individually actuated nozzle.

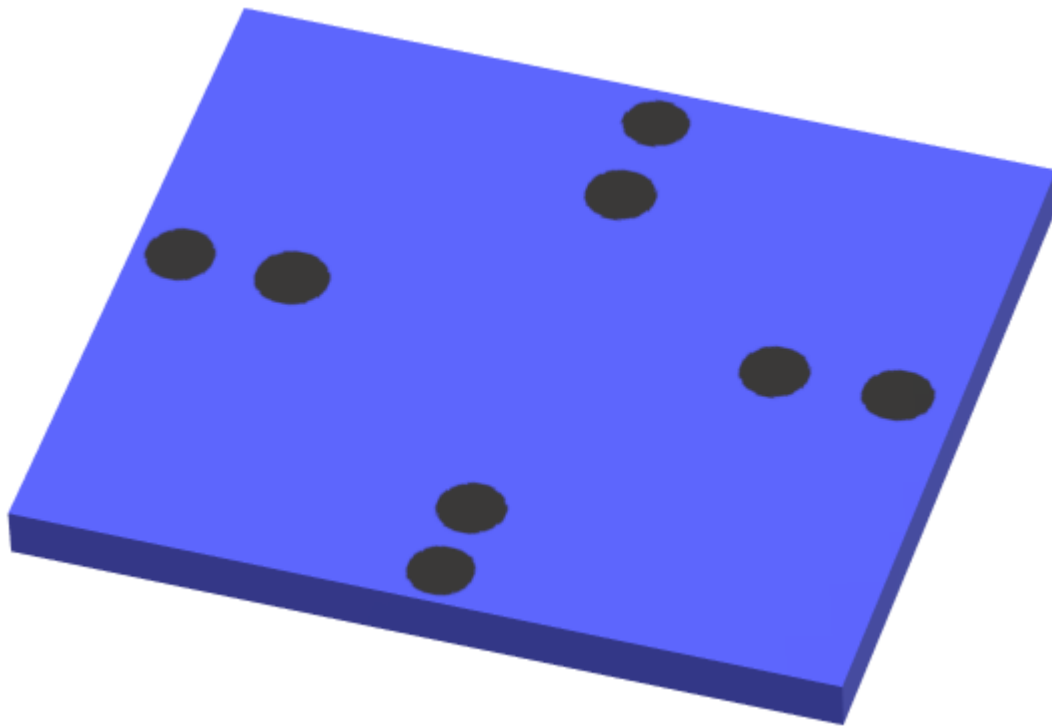


Figure 4.1: Micronozzle Chip.

The system design relies on a few functional requirements largely drawn from the *CubeSat Specification* [4.1]. Principle requirements include allowable operating pressures, materials, and exhaust properties, outlined in Table 4.1. *AMIGO* shall comply with all *CubeSat Specification* requirements even though the operation is not reliant on using traditional CubeSat deployment and

stowage techniques. This is because *AMIGO* and its enabling propulsive and inflatable technologies will first be tested in space where compliance is required. General trends include lower operating pressure requires less extensive range safety verification, less extreme and toxic exhaust chemicals, and minimizing volume and mass to conform to their respective budgets.

| <b>Requirement</b>   | <b>Comments</b>  |
|--|--|
| All parts shall remain attached to the CubeSats during launch, ejection and operation. No additional space debris will be created. | <i>CubeSat Specification</i> 3.1.2. Restricts solids in exhaust.   |
| No pyrotechnics shall be permitted.  | <i>CubeSat Specification</i> 3.1.3. Limits combustion without waiver.  |
| Any propulsion systems shall be designed, integrated, and tested in accordance with AFSPCMAN 91-710 Volume 3.                      | <i>CubeSat Specification</i> 3.1.4. Influences testing procedures and general safety precautions for handling and storage. |
| Propulsion systems shall have at least 3 inhibits to activation.   | <i>CubeSat Specification</i> 3.1.5. A series of valves is needed to eliminate premature actuation.                         |
| Total stored chemical energy will not exceed 100 Watt-Hours.   | <i>CubeSat Specification</i> 3.1.6. Certain chemicals are not permitted, especially for combustion-type systems.           |
| CubeSat hazardous materials shall conform to AFSPCMAN 91-710, Volume 3.  | <i>CubeSat Specification</i> 3.1.7. Limits on pressure chambers, safety factors, and material requirements.                |
| Propulsion system mass shall be less than 200 grams  | Must fit within mass allocation.   |
| Propulsion system volume shall be less than 0.2 U.   | Must fit within volume allocation.   |
| Propulsion system must have simple, reliable actuation method with response time <50 ms.   | This critical system shall have well-known characteristics to operate autonomously.  |
| The system shall provide capability for at least 5 hops.   | Provides <i>AMIGO</i> the capability of collecting robust science data and surface characterization.                       |
| The system shall provide 7-12 milli-Newtons of thrust for hopping capabilities.  | <i>AMIGO</i> must be able to hop to a variety of locations.  |

Table 4.1: Micropropulsion System Requirements

#### 4.a Literature Review: Other Micropropulsion Systems

Current chemical propulsion systems in development for use in CubeSats largely focusses on advancing green monopropellants. A monopropellant is the simplest combustion engine, requiring only one storage tank and set of valves and some pressurizing inert gas to maintain tank pressurization (Figure 4.2). Hydrazine has been used effectively in the past and many systems are highly matured (TRL 9). The drawback is that hydrazine is toxic, posing a danger to ground crew during testing, assembly, and fueling. Green monopropellants would increase the viability of using chemical propulsion in CubeSats, especially for student teams. One such effort is by Aerojet Rocketdyne, in their development of the AF-M315E green monopropellant in use for their GR-1 system. Their propellant has a much higher density  $I_{sp}$  (specific impulse, a measure of rocket efficiency) than hydrazine with a much lower freezing point [4.2]. The GR-1 provides 1 N of thrust with an  $I_{sp}$  of 235 s. The system is quite efficient for CubeSats, though is currently too large for use in smaller satellites. This is a common characteristic of chemical propulsion, and they often only have one nozzle so more than one unit is needed for attitude control. Another potential monopropellant would be hydrogen peroxide. The lower performance to hydrazine is balanced with the relative safety, especially in that the exhaust products are gaseous oxygen and water.

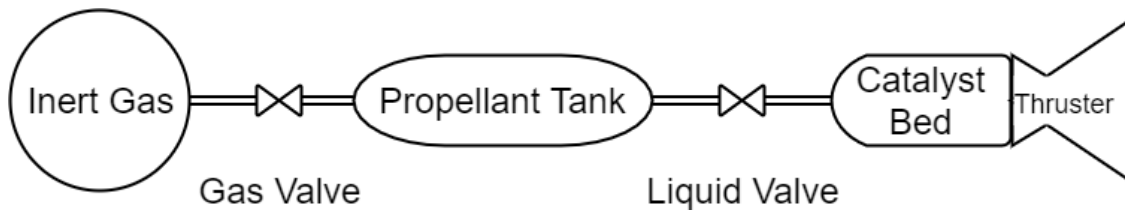


Figure 4.2: Monopropellant Block Diagram

Bipropellant systems tend to be even more bulky and complex than their monopropellant counterparts. They tend to be more efficient than monopropellant configurations with higher chamber temperatures, which has a material compatibility downside. Two reservoirs, one for fuel and one for oxidizer, are needed with more piping and pressure monitoring systems (Figure 4.3). Simply, these systems are too complex to be used reliably and within the volume and mass budgets. Another limiting factor is that combustion products, including various oxides of nitrogen, carbon monoxide, carbon dioxide, and water would interact significantly with the organic asteroid surface. This chemical interaction has the possibility of obscuring some of the science data to be collected, especially by the orbiter spacecraft.

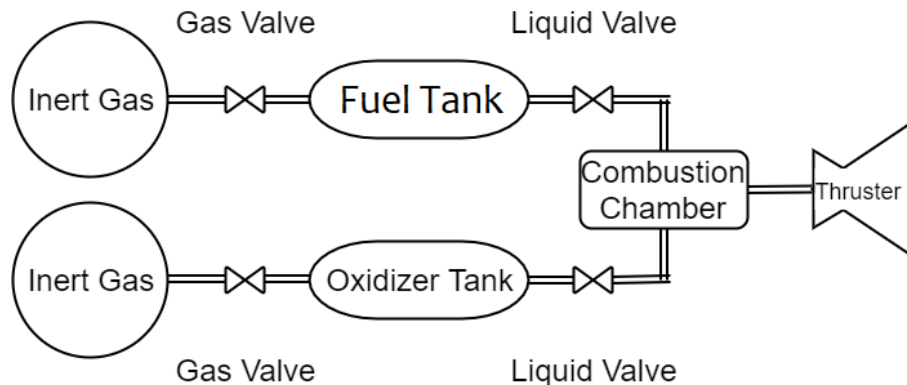


Figure 4.3: Bipropellant Block Diagram

Traditional solid propellant formulations have less complex fluidic systems than a bipropellant but again has the pitfalls of combustion products. One interesting development is the use of electrically actuated solid propellants, ePropellants. In this demonstrated concept, a concentric cathode sandwiches the propellant with an insulation layer that burns away slightly ahead of the exposed propellant surface to allow combustion only of the exposed area (Figure 4.4) [4.3]. Various propellants have been able to achieve over 200 s  $I_{sp}$ . The key distinction between ePropellants and regular solid propellants is the ability to rapidly ignite and shut off, allowing for the fine control required of a hopping robot.

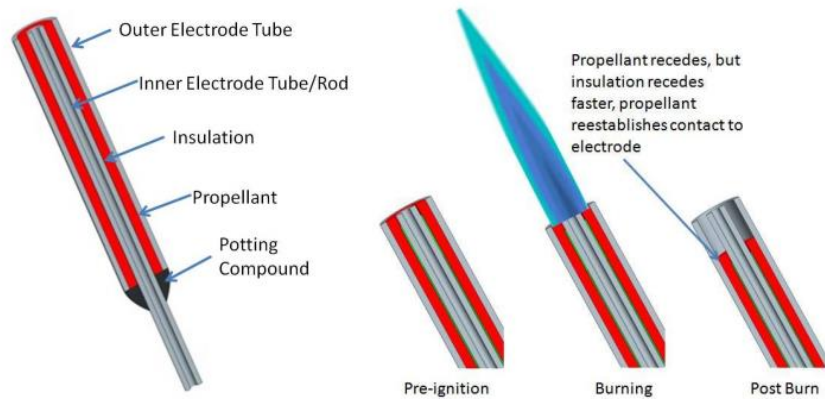


Figure 4.4: ePropellant Cathode [4.3]

Use of electrospray thrusters, such as the Microfluidic Electrospray Propulsion (MEP) [4.4] system, has been explored as they tend to offer quite high efficiencies while tending to be low mass. The delta-v capabilities of the system are promising, and low thrust provided is conducive to attitude control for larger satellites. These systems tend to be quite small and produce thrust in the micro-Newton range. MIT has developed a 1x1x1 cm MEP system that can operate on a variety of ionic liquids [4.5]. Of concern is the high velocity ions emitted, as they may negatively interact with surface regolith to be studied. The fine particles are electrostatically active, so it is desirable to not interfere with the natural processes as much as possible, as ejected ions may alter surface characteristics. Although each MEP module has an array of emitters, they units themselves do not provide attitude control as all emitters are actuated at once.

Cold gas systems tend to be the simplest propulsion systems, essentially consisting of a pressurized gas, control valves, and acceleration nozzles. GOMSpace has developed a butane cold gas propulsion system for 2-3 U CubeSat missions [4.6]. The system itself occupies 0.5 U of volume, which limits the use cases to CubeSats of form factor 3 U+. There are four individually actuated nozzles that provide coarse attitude control. The operating pressure within the storage tank is 2-5 bar. The system does contain multiple performance sensors, such as a flow rate sensor, pressure sensors, and heaters for improved  $I_{sp}$ . Each of these adds to the complexity and size of the system. By resistive heating of the gas, the system becomes known as a resistojet.

An extension of cold gas systems is to store the propellant as either a liquid (called liquid-vapor systems) or as a solid (sublimate systems). The benefits of these is that there is no need to store the gas at a high pressure; instead, the vapor from the condensed phase is the exhaust gas. A variety of liquid-vapor systems have been developed. Typically, the vapor pressure is controlled by heating the two-phase system. The Canadian Nanosatellite Advanced Propulsion System

provides station keeping and formation control for swarm systems of CubeSats [4.7]. The system provides 18 m/s of  $\Delta v$  from 260 g of SF<sub>6</sub>. Another take on the liquid-vapor storage option is a propulsion system used on the SNAP 1 mission, utilizing butane as the liquified gas [4.8]. The vapor pressure of butane is 2 bar at 25° C, allowing for thin walls in the storage tank, characteristic of other non-gaseous storage techniques.

Utilizing the resistojet concept, heating of the vapor in a liquid-vapor cold gas system increases performance. The Free Molecule Micro Resistojet [4.9] utilizes electrical heating of individual molecules. Instead of a converging-diverging nozzle, propellant passes through an array of electrically heated slots. The slot geometry is smaller than the mean free path of the molecules, heating the molecules when they come in contact with the wall. An interesting comparison of two systems, CHIPS and AMR, using the same propellant R-134a resulting in differing thrust and specific impulse [4.10, 4.11]. CHIPS has a lower specific impulse with higher thrust contrasting to AMR's results. The CHIPS system would be able to lift a heavier robot of the surface of some small solar system body, while AMR can efficiently propel smaller systems. From the Tsiolkovsky rocket equation, AMR can provide more delta-v, thus extending the life of a hopping systems or low Earth orbit missions.

A Vaporizing Liquid Microthruster uses resistive heating to vaporize a liquid and expel it through a nozzle. The VLM under development at JPL is a three-laminate chip targeted for use as an attitude controller on small spacecraft [4.12]. Liquid enters the inlet channel, is heated and vaporized in the middle laminate, and is accelerated through the nozzle laminate. Various liquids have been tested, including water, hydrazine, and ammonia, with current performance goals being thrust of 0.1 to .05 milli-Newtons and  $I_{sp}$  under 100 s. Another VLM design has been tested by Silva et. al [4.13] and tested for a wide variety of candidate propellants. Water produced the best results in terms of  $I_{sp}$  and  $\Delta v$ . This model is a planar approach, in which the inlet area, vaporizing chamber, and outlet nozzle all lie in the same plane.

The Micro Solid Propellant Thruster (MSPT) developed by Lee et al. [4.14] is an array of one-time use thrusters utilizing sublimate concepts. The operating principal is that a solid propellant is heated by a platinum ignition coil to build pressure behind a diaphragm. As the pressure reaches some critical burst pressure of the diaphragm, the diaphragm bursts and releases the gas to provide thrust. Ignition of the sublimate was able to produce a max thrust of 3619 milli-Newtons. Mechanical design is fairly simple as there does not need to be any flow channels or control valves between the storage tank and nozzle due to clever design. The negative of this design is that each nozzle can only be used once, limiting the mission duration. The thrust is also uncontrolled, as once the solid is ignited, there is no stopping or throttling the process.

| Type                    | System                           | Propellant         | I <sub>sp</sub> [s] | Thrust [mN] | Volume       | Attitude Control |          |
|-------------------------|----------------------------------|--------------------|---------------------|-------------|--------------|------------------|----------|
| Chemical                | Aerojet GR-1 [4.2]               | AF-M315E           | 235                 | 1000        | -            | No               |          |
| Electrospray            | MEP [4.4]                        | Indium             | > 3000              | 0.1         | 0.009 U      | No               |          |
|                         | MIT Electrospray [4.5]           | Ionic Liquids      | 760                 | 0.0125      | 0.001 U      | No               |          |
| Cold Gas                | GOMSace NanoProp 3U [4.6]        | Butane             | 60-100              | 10          | 0.5 U        | Coarse           |          |
| Liquid-Vapor Cold Gas   | CNAPS [4.7]                      | SF <sub>6</sub>    | 45                  | 10-50       | Large        | No               |          |
|                         | SNAP 1 [4.8]                     | Butane             | 43                  | 50          |              | No               |          |
| Liquid-Vapor Resistojet | FMMR [4.9]                       | Water              | 79                  | 1.7         |              |                  |          |
|                         | CHIPS [4.10]                     | R-134a             | 82                  | 30          |              |                  |          |
|                         | AMR [4.11]                       | R-134a             | 150                 | 10          |              |                  |          |
|                         | JPL VLM [4.12]                   | Water              | < 100               | 0.1-0.5     |              |                  | Possible |
|                         | VLM Silva et al. [4.11]          | Water              | 120                 | 0.68-1      |              |                  | Possible |
| Sublimate               | T <sup>3</sup> μPS [4.15] [4.16] | Water, Nitrogen    | 100                 | 0.5-3       | 0.2 U        | No               |          |
|                         | MSPT [4.14]                      | Lead-Styphenate    | 62                  | 3600        | 2.1 mm thick | Yes              |          |
| ePropellant             | DSSP [4.3]                       | ABIP, ASPEN, HIPEP | 225-260             |             |              | Possible         |          |

Table 4.2: Performance of Other Micropropulsion Systems

#### 4.b: Significance of the Asteroid Environment

Even though the gravitational acceleration experienced on small solar system bodies on the scale of 101955 *Bennu* or 25143 *Itokawa* is 6 orders of magnitude smaller than that on Earth, it is still the dominant force of hoppers especially over their relatively short exposure to gravitational disturbances. Considering a 101955 *Bennu* sized object with mass  $7.3 \cdot 10^{10}$  kg and average radius 260 m, the escape velocity is  $\sim 0.19$  m/s.

$$v_{esc} = \sqrt{\frac{2Gm_{ast}}{r_{ast}}} \quad (4.1)$$

Where  $G$  is the gravitational constant,  $m_{ast}$  is the asteroid mass, and  $r_{ast}$  is the radius of the asteroid. It is desired to be able to hop distances on the range of  $x_f = 10-50$  m. Thus, the  $\Delta v$  per hop is around 5 cm/s to obtain 36 m hop distance with launch angle  $45^\circ$  assuming parabolic trajectory.

$$x_f = \Delta v * \cos(\theta) * t_{hop} \quad (4.2)$$

Where  $t_{hop}$  is the time of the parabolic hop,

$$t_{hop} = \frac{2\Delta v * \sin(\theta)}{g_{ast}} \quad (4.3)$$

Where  $g_{ast}$  is the gravitational acceleration of the asteroid, assumed uniform and neglecting lumpy gravity fields,

$$g_{ast} = \frac{G * m_{ast}}{r_{ast}^2} \quad (4.4)$$

Assuming a 5-10 second fire, well within the hop time so one can assume an impulse for first order calculations, results in a thrust of 7-12 milli-Newtons.

$$F = \frac{m_{ast} * \Delta v}{t_{burn}} \quad (4.5)$$

It is desired to have sufficient capabilities to conduct at least 5 hops, allowing for some fuel to be spent on attitude control. The propulsion system as a hopping actuator and control actuator eliminates the need for a full 3 axis reaction wheel, instead requiring either 1 or 0.

The exhaust propellant should also have limited reactivity with the asteroid's surface characteristics. The surface of asteroids tends to be carbonaceous, with potential water ice layers on outer main belt asteroids [4.17, 4.18]. Asteroid 101955 *Bennu* has shown evidence of underlying hydrated materials that cause dust to be kicked up from the surface [4.19]. In the goal of minimizing surface interaction, many types of propellants are not considered such as hydrazine or those with highly ionized exhausts. Also of main concern are combustion products that typically result in various oxides of carbon and nitrogen that would affect spectral measurements.

#### 4.c: Cold Gas Systems

As opposed to chemical, electrical, and other propulsion methods, cold gas systems rely solely on stored enthalpy to accelerate gas through a nozzle to provide thrust. Propellant gas is stored in a pressurized chamber, and the pressure differential to the nozzle exit drives the flow to supersonic speeds. Performance values, including delivered thrust and specific impulse, is lower than chemical rockets because the energy stored in chemical bonds is not utilized. The chamber pressure is also limited to 100 psi unless special, expensive testing and certification is done to flight-qualify the pressurized storage tank. Otherwise, these components are classified as hazardous flight hardware [4.20].

The lower performance is offset by the reduction of logistical challenges. Cold gas systems have fluid flow at much lower temperatures compared to chemical methods, often measuring up to 400-500° C instead of 1000s° C. The actuation of these systems is simple, requiring only valve operation instead of valving plus some sort of ignition or catalytic system.

Cold gas systems tend to be the simplest in design amongst propulsion technology. In its simplest form, the only required components are a storage tank, isolation valve, and nozzle. Electrothermal systems, namely resistojets, can be thought of as a cold gas system with heat addition either in the storage tank or flow ducts. Examination of the isentropic relations [4.21] provides insight into nozzle geometry and propellant selection. Delivered thrust is

$$F = \lambda \dot{m} v_e + (p_e - p_a) A_e \quad (4.6)$$

Where  $F$  is the thrust,  $\lambda$  is the conical nozzle correction factor accounting non-axial flow,  $\dot{m}$  is the mass flow rate of propellant,  $v_e$  is exhaust velocity,  $p_e$  is nozzle exit pressure,  $p_a$  is ambient pressure, and  $A_e$  is the nozzle exit area.  $\lambda$  is based on the semi-vertex angle  $\sigma$  of the conical nozzle,

$$\lambda = \frac{1 + \cos(\sigma)}{2} \quad (4.7)$$

Conical nozzles are considered for their ease of manufacturing with available techniques over more efficient but complex shapes, such as *de Laval* and parabolic nozzles. Ideally, the smaller the semi-vertex angle, the more efficient the conical nozzle. With practical limits, this would lead to a longer nozzle for a given area ratio, whereas increasing the angle for a shorter nozzle might induce flow separation. The equation for exhaust velocity is:

$$v_{ei} = \sqrt{\frac{2\gamma R_{univ} T_c}{M(\gamma - 1)} \left(1 - \frac{T_e}{T_c}\right)} \quad (4.8)$$

The equation for mass flow rate is:

$$\dot{m}_i = A_t p_c \gamma \sqrt{\frac{\left(\frac{2}{\gamma + 1}\right)^{\frac{\gamma+1}{\gamma-1}}}{\gamma R T_c}} \quad (4.9)$$

Where  $\gamma$  is the specific heat ratio,  $R_{univ}$  is the universal gas constant,  $T_c$  is the chamber temperature,  $T_e$  is the exit temperature,  $M$  is the molecular mass of the gas,  $A_t$  is the nozzle throat area,  $p_c$  is the chamber pressure, and  $R$  is the gas constant for a specific gas. The  $i$  subscript refers

to isentropic assumptions. For cold gas systems, the ideal specific impulse  $I_{sp}$  is analyzed to compare efficiency of potential propellants,

$$I_{sp} = \frac{v_e}{g_0} \quad (4.10)$$

| <b>Gas</b>                     | <b><math>\gamma</math></b> | <b>M (g/mol)</b> | <b><math>I_{sp}</math> (s)</b> |
|--------------------------------|----------------------------|------------------|--------------------------------|
| SF <sub>6</sub>                | 1.11                       | 146              | 76                             |
| Air                            | 1.4                        | 28.97            | 91                             |
| N <sub>2</sub>                 | 1.4                        | 28.01            | 85                             |
| Ar                             | 1.66                       | 39.95            | 57                             |
| H <sub>2</sub>                 | 1.41                       | 2                | 296                            |
| CH <sub>4</sub>                | 1.32                       | 16               | 114                            |
| C <sub>4</sub> H <sub>10</sub> | 1.09                       | 58.12            | 80                             |
| I <sub>2</sub>                 | 1.26                       | 253.8            | 40                             |

Table 4.3:  $I_{sp}$  of Cold Gas Propellants

Except for hydrogen, which is not used in practice due to storage issues, cold gas systems are limited to 115s  $I_{sp}$ . In actual systems, the limitation is to 80 s due to losses. Resistojets increase  $I_{sp}$  by increasing the chamber temperature. This in turn leads to higher exhaust velocities. In general, lower molecular weight and higher specific heat ratio leads to a higher efficiency. Some resistojets can achieve an  $I_{sp}$  over 200 s [4.22].

Conventionally, cold gas propellant is stored as a gas, common with systems utilizing nitrogen or hydrogen. The issue with gas storage is that the storage tank must be at high pressures to contain an appreciable amount of fuel for longer mission durations. Higher pressure systems are prone to leak much more than lower pressure tanks, as leak rate is proportional to the storage pressure. This means components must be bulkier to withstand stress and the increased volume of gas. Two other methods of cold gas storage are liquid phase and solid phase. These two approaches work on the principle of vapor pressure equilibrium; for any given temperature, the gas will exert some pressure on the condensed phase. For liquids, this is referred to as evaporation; solids sublime into a gas phase. Both storage schemes have the benefit of lower pressure tanks compared to gas storage, though some additional components are required.

The vapor pressure for liquids tends to be higher than solids for a given temperature. Liquid storage has been utilized to great effect, notably with water in various vaporizing liquid microthrusters and sulfur hexafluoride (SF<sub>6</sub>) for the NANOPS system of the Can-X2 mission [4.23]. The downside compared to sublimates is the issue of “sloshing,” where the liquid freely moves in the storage tank causing inertial instabilities and potential clogging of the tank exit to flow channels. Sublimates are able to be fixed in place to the storage tank and deserve consideration.

#### 4.d: Sublimate Propulsion

For substances below their triple point in a phase diagram, a solid can phase transition to a gas without transitioning to an intermediate liquid phase in a process called sublimation; the opposite process is deposition. For any pressure and temperature the solid is subjected to, there exists an equilibrium vapor pressure, or solid-gas equilibrium pressure, that the gaseous state exerts on the solid. This pressure is not to be confused with the ambient pressure, which is the pressure exerted on the entire two-phase system. The vapor pressure is a nonlinear function of temperature, and can be approximated by the Clausius-Clapeyron Relation:

$$\frac{dP}{dT} = \frac{L}{T\Delta v} \quad (4.11)$$

Where  $P$  is the pressure,  $T$  is temperature,  $L$  is specific latent heat, and  $v$  is specific volume. There are multiple derived forms of this equation, such as the Antoine Equation whose coefficients  $A$ ,  $B$ , and  $C$  are derived empirically:

$$\log_{10}P = A - \frac{B}{C + T} \quad (4.12)$$

There are a few candidate propellants examined for potential use (see Figure 4.5). Considerations include high chamber pressure with a low temperature and material compatibility with system components.

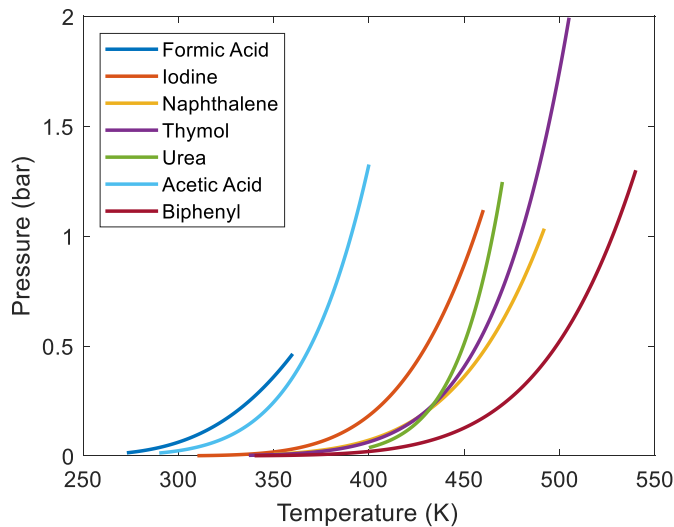


Figure 4.5: Vapor Pressure vs. Temperature of Sublimate Substances (data from NIST [4.24])

Sublimation is an endothermic process, requiring heat addition often by resistive heating for molecules to escape attractive forces. As the temperature of the system increases, the vapor pressure increases. This leads to one of the large advantages of using sublimating propellant as opposed to gas storage: the sublimate acts as its own pressure regulator through temperature control (until a sufficiently low mass of solid is left later in the propulsion system's life). In a gas storage system, thrust monotonically decreases as propellant is used due to lower chamber pressures after each thrusting maneuver. The sublimation vapor pressure is more stable, thus

decreasing complexity of the system. There is no need for an external pressure regulator or for the system to be externally pressurized. Constant chamber pressure increases reliability of the system, resulting in lower error in delivered thrust.

The resultant propulsion system is shown in Figure 4.6. Storage density of a sublimate substance is much higher than gas storage, leading to a longer mission lifetime. The vapor pressure tends to be low compared to gaseous storage [4.25], up to a few bars for more volatile substances such as dry ice or urea. The positive effect of this is a simpler storage tank design, as the tank can have thinner walls and be lighter. Leak rate will also be slower, as that is dependent on the storage pressure. Lower chamber pressure does decrease the deliverable thrust however, as mass flow rate is proportional to chamber pressure. This will tend to limit sublimate systems to operation in a vacuum, such as attitude control or asteroid exploration. Further analysis on candidate propellants is needed to characterize replenishing time and pressure obtained via temperature control. Previous groups have established that under sufficiently low operating pressures, sublimate systems can thrust continuously for 20 hours, well beyond the requirement for AMIGO's hop and attitude control timing [4.25].

There are two added design complexities of utilizing sublimate propellant. The storage tank must be temperature regulated and very well insulated to ensure proper control of chamber conditions. Heating of the tank can be done through Joule heating, such as nichrome wires wrapped around the tank or an incandescent film inserted into the propellant/ gas, such as in the Aerojet MR-501 rocket engine. Heating increases specific impulse, as specific impulse is proportional to chamber pressure.

To prevent two phase flow, as there will almost certainly be small particles of solid propellant flowing with the gas, a filter must be used upstream to prevent clogging of downstream components. Pressure losses induced by a filter will negatively affect thrust, so careful consideration of minimal impact must be balanced with filtering the required solid particulates. The mesh sizing will change dependent on each mission's requirements, largely the geometry and sizing of the propulsion system. Figure 4.6 is a representative schematic of the system, highlighting the few components and simplicity,

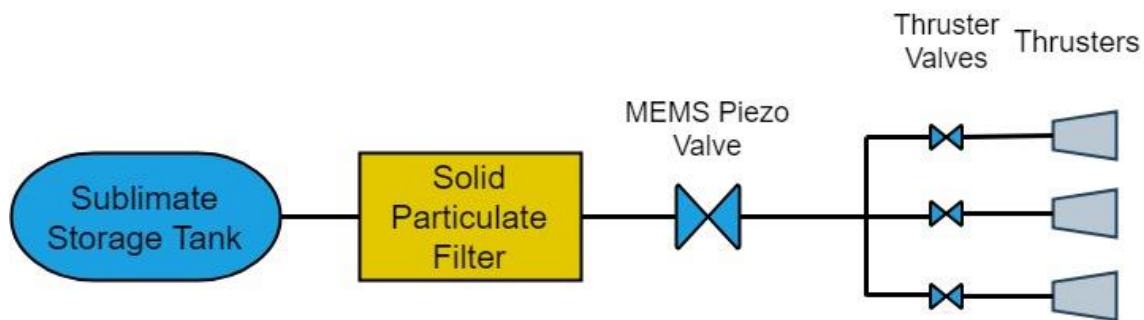


Figure 4.6: Sublimate Propulsion System Schematic

#### 4.e: Micronozzle Design

The purpose of a thruster system is to convert mechanical energy in the form of a pressurized gas into kinetic energy of the gas leaving the spacecraft. In accordance with Newton's Third Law, this exhaust gas imparts momentum onto the spacecraft in the opposite direction, resulting in motion. Given some storage conditions of the gas, the most effective way to convert the mechanical energy to kinetic is in use of a supersonic converging-diverging nozzle. An increase of the effective exit velocity corresponds to an increase in efficiency for the same mass flow rate and contributes more thrust. Thus, the most efficient and powerful nozzles are ones that produce the fastest exhaust gas. A conical nozzle diagram with design parameters is shown in Figure 4.7.

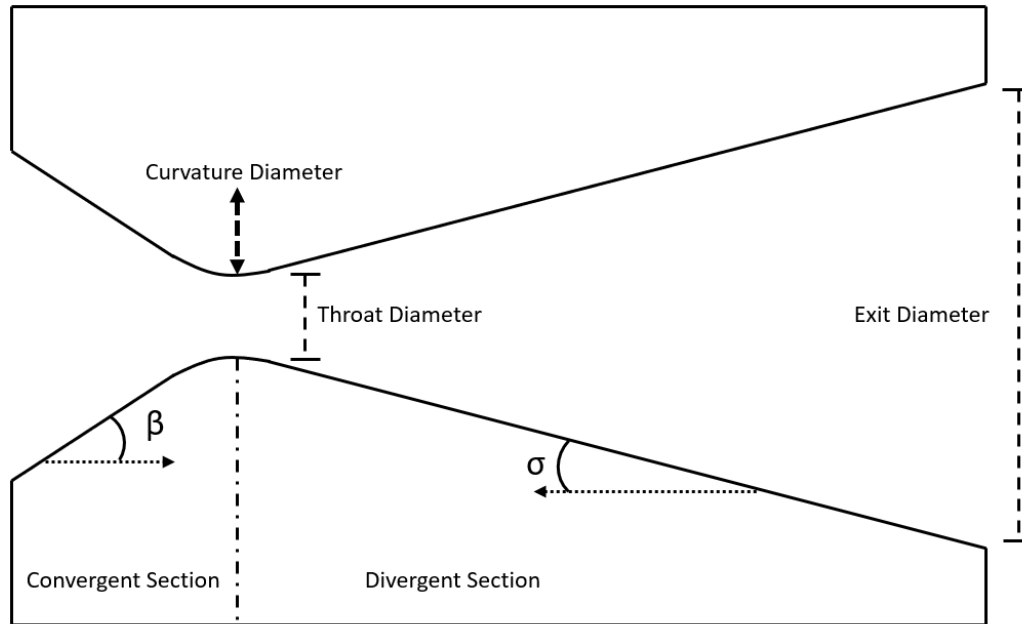


Figure 4.7: Converging-Diverging Nozzle

Upstream gas is considered to have high pressure and little velocity. The gas flow enters the convergent section at subsonic velocities, increases velocity according to Bernoulli's principle until it reaches Mach 1 (speed of sound) at the throat for sufficient storage temperatures compared to ambient conditions, and goes supersonic in the divergent section. The principle mechanism to optimize a propulsion system is to optimize the nozzle. Primarily of importance is the divergent section as the main role of the convergent section is to provide a smooth flow with little boundary layer growth or risk of flow separation. This section explains how the nozzle is designed, broken up into the divergent section and its optimization then the convergent and throat geometry.

#### 4.e.i: Quasi-Isentropic Analysis with Microfluidic Effects

Conventional nozzle design on large scale rockets is done through isentropic relations. The assumptions in derivation are homogeneous, perfect, single phase, adiabatic gas flow, a lack of discontinuities from internal shock waves, axial exhaust flow, and friction/ boundary layer effects are neglected [4.21]. However, the flow in micro-nozzles can have vast differences than this idealized rocket model. Principally, micro-nozzles have a large surface area-to-volume ratio compared to large-scale rockets which reduces the Reynolds number. This is due to the thrust requirements for small propulsion systems necessitating a reduction in the nozzle size, as thrust is proportional to the square root of the nozzle throat diameter. The surface area is proportional to the square of the diameter, while the nozzle volume is proportional to the cube of the throat diameter. This increase in surface area-to-volume ratio causes and vastly decreased Reynolds number cause a large increase in viscous losses and boundary layer growth [4.26, 4.27]. Another important factor is the height of surface imperfections on the nozzle's interior, as their size is no longer negligible compared to the boundary layer thickness as opposed to conventionally sized rocket nozzles. An interesting result from this is a decrease in the effective semi-vertex angle as the boundary layer grows along the length of the nozzle. These three effects contribute to an overall loss of efficiency of the nozzle and a drop in thrust produced when using an isentropic model.

Another consideration for these small nozzles is the Knudsen number, a comparison between some characteristic length (throat diameter) to the mean free path of the molecular gas (Equation 4.13). The mean free path is the average distance molecules in travel before interacting with another gas particle. The Knudsen number is defined as

$$Kn = \frac{\ell}{d_t} \quad (4.13)$$

Where  $\ell$  is the mean free path of the gas and  $d_t$  is the nozzle throat diameter. The Knudsen number is especially important for MEMS devices and microfluidics, as the lower pressures and smaller characteristic lengths can be on the same order as the molecule's mean free path. Four regions of  $Kn$  are considered to determine the correct fluid modelling to use, either statistical or continuum. For  $Kn < 0.01$ , the mean free path is much smaller than nozzle geometries and the flow is in the continuum regime. Here, fluid dynamics can be analyzed using traditional methods such as isentropic analysis. For  $0.01 < Kn < 0.1$ , the flow is in the slip-flow regime. Away from boundaries, the flow can still be analyzed with continuum mechanics, but the boundary flow must be treated with care. The gas flow near the walls is still dominated by intermolecular collisions, rather than collisions with the wall; however, some slip at the wall is experienced. The gas flow enters the transition or rarified regime for  $0.1 < Kn < 1$ . The fluid-structure and fluid-fluid interactions are equally important, and a combination of statistical and continuum methods are required, adding significant complexity to the problem. When  $Kn > 1$ , the flow is in the free molecular regime. The molecules will be dominated by fluid-structure interactions and require statistical mechanics. The mean free path is estimated by Equation 4.14,

$$\ell = \frac{kT}{\sqrt{2\pi p}d_m^2} \quad (4.14)$$

Where  $k$  is the Boltzmann's constant,  $T$  is the chamber temperature,  $p$  is the chamber pressure, and  $d_m$  is the molecular diameter. Assuming chamber conditions of 0.75 bar and 350 K, reasonable

assumptions from candidate propellants, and a throat diameter of 500 microns, the Knudsen number can be approximated for various candidate propellants and summarized in Table 4.4,

| Propellant  | Kn                   | Continuum? |
|-------------|----------------------|------------|
| Nitrogen    | $2.88 \cdot 10^{-5}$ | Yes        |
| Iodine      | $7.4 \cdot 10^{-6}$  | Yes        |
| Formic Acid | $5.9 \cdot 10^{-6}$  | Yes        |
| Naphthalene | $2.8 \cdot 10^{-7}$  | Yes        |
| Thymol      | $2.3 \cdot 10^{-7}$  | Yes        |
| Urea        | $5.2 \cdot 10^{-7}$  | Yes        |
| Acetic Acid | $4.5 \cdot 10^{-7}$  | Yes        |
| Biphenyl    | $2.4 \cdot 10^{-7}$  | Yes        |

Table 4.4: Knudsen Number of Various Propellants

From the desired performance results in 4.b: *Significance of the Asteroid Environment*, Equation 4.15 is used, assuming near optimal expansion so the pressure term may be neglected (in reality, the nozzle would be under-expanded due to vacuum ambient pressure on an asteroid). The most efficient conversion of mechanical energy in the form of the fluid's static pressure to kinetic energy by expanding the pressure to the ambient vacuum conditions requires either an infinitely small throat diameter or infinitely long nozzle to obtain the required infinite expansion ratio. This would also cause problems in the fluid's temperature, as it would cross into the deposition regime in which the flow returns to solid form and adheres to the nozzle surface. This leads to decreasing efficiency over time and increased surface roughness. The pressure term is still negligible compared to the velocity portion of the thrust equation due to the low exit pressure. Thus, for a conical nozzle the thrust becomes

$$F = \lambda \dot{m} v_e \quad (4.15)$$

From Kundu *et al.* [4.28] the optimal conical semi-vertex angle was found to be  $28^\circ$  as opposed to the normal optimal angle of  $15^\circ$  for macro-nozzles due to microfluidic effects. However, other angles are considered due to limitations in MEMS fabrication processes. Anisotropic etching results in pre-defined nozzle angles due to dependence on crystal structure of the substrate [4.29]. For example, silicon wafer anisotropic wet etching results in an angle of  $35.3^\circ$ , the angle of the  $\langle 111 \rangle$  plane to vertical. A chamber pressure of 1 bar is used in further calculations, as it is easily attainable as shown in Figure 4.5. Another consideration is in the increased effect of the boundary layer at such small scales; longer nozzles have larger boundary layer growth that limits the effective area of the nozzle to decrease mass flow rate while increasing viscous losses. This is largely due to a weird flow regime where the main flow is supersonic but there exists a relatively large subsonic boundary layer compared to macro nozzles. Typically, micro-nozzles have an optimal angle greater than that of macro-nozzles due to these two effects. A design exit pressure of 100 Pa is used. Further correction due to viscous effects are needed, as the flow will have a low Reynolds number and a boundary layer displacement thickness approaching the order of the nozzle diameter [4.13]. These effects are captured in a corrected thrust coefficient  $C_F$ ,

$$C_F = C_{F_i} - C_{F_v} \quad (4.16)$$

Where  $C_{F_i}$  is the isentropic thrust coefficient,

$$C_{F_i} = \frac{F_i}{p_c A_t} \quad (4.17)$$

Where  $F_i$  is the isentropic thrust produced by the nozzle,  $p_c$  is the chamber pressure, and  $A_t$  is the nozzle throat area. The thrust coefficient is defined as

$$C_F = \frac{F}{p_c A_t} \quad (4.18)$$

Where  $F$  is the real thrust produced.  $C_{F_v}$  is the thrust coefficient loss due to viscous effects. The thrust coefficient is a measure of how well a nozzle expands the flow to produce thrust compared to a nozzle truncated at the throat. From the same chamber conditions and throat area, the divergent sections of nozzles can be compared. From experimentation on conical nozzles with cold gas flow [4.30], the viscous loss term can be determined as

$$C_{F_v} = \frac{17.6e^{0.032\varepsilon}}{\sqrt{Re_{t,w}}} \quad (4.19)$$

Where  $\varepsilon$  is the nozzle exit to throat area ratio and  $Re_t$  is the Reynolds number at the throat near the wall.

$$Re_{t,w} = Re_t \left( \frac{T_t}{T_{t,w}} \right)^{\frac{5}{3}} \quad (4.20)$$

Where  $Re_t$  is the Reynolds number at the throat,  $T_t$  is the throat temperature, and  $T_{t,w}$  is the throat wall temperature. An adiabatic wall is assumed, though a typical micro-fabrication material like silicon tends to conduct heat away from the flow. The temperature ratio is assumed [4.30],

$$\left( \frac{T_t}{T_{t,w}} \right)^{5/3} = 0.857$$

Reynolds number at the throat, assuming ideal gas flow as an approximation, can be found by

$$Re_t = \frac{v_t d_t}{\nu_t} \quad (4.21)$$

Where  $v_t$  is the throat flow speed (Mach = 1),  $d_t$  is the throat diameter, and  $\nu_t$  is the throat kinematic viscosity. Under ideal gas flow, the throat speed is sonic,

$$v_t = \sqrt{\gamma R T_t} \quad (4.22)$$

Kinematic viscosity, using the ideal gas law, can be defined as

$$\nu = \frac{\mu}{\rho} = \frac{\mu}{p} \frac{p}{RT} \quad (4.23)$$

Kinematic viscosity at the throat is related to the stagnation condition through temperature,

$$\frac{\nu_t}{\nu_0} = \frac{\mu_t p_0}{\mu_0 p_t} \left( \frac{T_t}{T_0} \right) \quad (4.24)$$

From *Spisz et al.* [4.30], dynamic viscosity is related to temperature by

$$\frac{\mu_t}{\mu_0} = \left( \frac{T_t}{T_0} \right)^{\frac{2}{3}} \quad (4.25)$$

From isentropic relations, the pressure ratio can be converted to a temperature ratio

$$\frac{p_0}{p_t} = \left( \frac{T_0}{T_t} \right)^{\frac{\gamma}{\gamma-1}} \quad (4.26)$$

Thus, the kinematic viscosity ratio is

$$\frac{\nu_t}{\nu_0} = \left( \frac{T_t}{T_0} \right)^{\frac{-\gamma}{\gamma+1} + \frac{5}{3}} \quad (4.27)$$

From the stagnation to throat temperature ratio,

$$\frac{T_t}{T_0} = \frac{1}{1 + \frac{\gamma-1}{2} M^2} = \frac{2}{\gamma+1} \quad (4.28)$$

Where at the throat,  $M = 1$  (sonic). Thus, given some initial kinematic viscosity, the Reynolds number at the throat can be approximated by

$$Re_t = \sqrt{\gamma R T_t} d_t \left( \frac{T_t}{T_0} \right)^{\frac{-\gamma}{\gamma+1} + \frac{5}{3}} \nu_0^{-1} \quad (4.29)$$

The Reynolds number at the wall is found by

$$Re_{t,w} = 0.857 \sqrt{\gamma R T_t} d_t \left( \frac{T_t}{T_0} \right)^{\frac{-\gamma}{\gamma+1} + \frac{5}{3}} \nu_0^{-1} \quad (4.30)$$

The area ratio is limited by MEMS manufacturing techniques; although large expansion ratios increase efficiency, they defy the purpose of miniaturizing nozzles and silicon wafers tend to be less than 775 microns thick. Stacking of wafers to increase nozzle length will inherently produce manufacturing errors due to wafer alignment limitations, so the thickness should be limited to a non-optimal state. Correction to the mass flow rate from isentropic conditions is done iteratively through the discharge coefficient  $C_D$  [4.31],

$$\dot{m} = C_D \dot{m}_i \quad (4.31)$$

$$C_D = 0.8825 + 0.0079 \ln(Re_t) \quad (4.32)$$

With these correction factors for low  $Re$  flow, MATLAB is used to determine geometric properties of the divergent section of the converging-diverging nozzle. Analysis begins by

calculating the desired thrust from Equation 4.15 and fixing chamber pressure at 1 bar and chamber temperature at 400 K. Ranges of throat area and area ratio are used to calculate a range of exit areas

$$A_e = \varepsilon A_t \quad (4.33)$$

From this geometry, the expected viscous loss thrust coefficient is calculated based on the throat Reynolds number. Nitrogen is assumed stored at 400 K, 1 bar with kinematic viscosity  $26.35 \times 10^{-6} \text{ m}^2/\text{s}$ . Knowing the real thrust coefficient and loss coefficient, the isentropic thrust coefficient can be calculated.

$$C_{F_i} = C_F + C_{F_v} \quad (4.34)$$

This is an iterative process, as the isentropic nozzle will influence the viscous losses. For each design candidate, the calculations are iterated to match the isentropic results with the viscous results. The chamber pressure and throat area are the same for both the real and isentropic geometry. Thus, the required isentropic thrust required is calculated by

$$F_i = C_{F_i} p_c A_t = \lambda \dot{m}_i v_{e,i} \quad (4.35)$$

Mass flow rate is calculated by Equation 4.36, using isentropic analysis with the correction for discharge,

$$\dot{m} = C_D A_t p_c \gamma \sqrt{\frac{\left(\frac{2}{\gamma+1}\right)^{\frac{\gamma+1}{\gamma-1}}}{\gamma R T_c}} \quad (4.36)$$

Thus, for some exit area calculated from throat area and area ratio, the required exit velocity can be calculated as

$$v_{e,i} = \frac{\dot{m} R T_e}{p_e A_e} \quad (4.37)$$

A combination of isentropic nozzle geometry, exit velocity, and mass flow rate corresponds to some real thrust. As can be seen, this process of accounting for viscous losses is an iterative process. Each nozzle is evaluated for the viscous losses and mass flow rate until they correlate to each other's conditions.

To gain an understanding of how the area ratio and throat diameter affect performance, Figure 4.8 shows the plots of  $I_{sp}$  and thrust versus those two variables with a fixed semi-vertex angle of  $32^\circ$ . With traditional nozzles, an infinite area ration maximizes thrust and specific impulse when exposed to vacuum ambient conditions. Due to the nature of low Reynold's number flow, a maximum in specific impulse is reached when accounting for viscous losses much earlier. Output thrust is expectedly linear with throat diameter and area ratio. This figure also shows the low performance of nozzles with such small divergent angles.

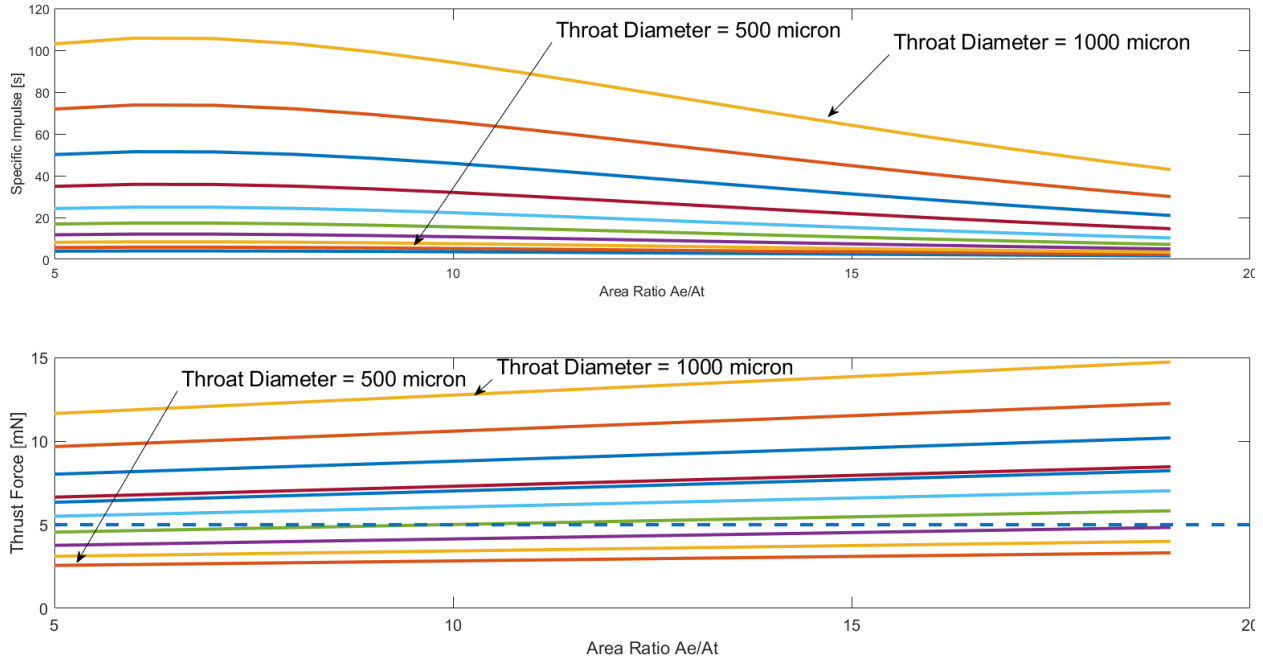


Figure 4.8: Performance of 32° Conical Micronozzles

As the problem is formulated with three design variables (divergent semi-vertex angle, throat diameter, and area ratio), an optimization process is preferable to a simple 2D array search. This also extends the potential to add more variables to the problem. The nozzle is optimized for specific impulse and length while adhering to constraints for required thrust and intuitive limits on semi-vertex angle and area ratio. This process is detailed in *Section 4.e.ii: Constrained Particle Swarm Optimization*. Table 4.5 shows the results of nozzle optimization with expected performance when nitrogen is the working fluid. Of note, performance will drop when sublimate chemical are used due to larger molecule size and mass.

| Parameter          | Value                     |
|--------------------|---------------------------|
| Throat Diameter    | 870 $\mu\text{m}$         |
| Area Ratio         | 8                         |
| Semi-vertex Angle  | 32°                       |
| Expected $I_{sp}$  | 71.2 s                    |
| Expected Thrust    | 10.1 mN                   |
| Expected $\dot{m}$ | $1.28 \cdot 10^{-5}$ kg/s |

Table 4.5: Designed Micronozzle

#### 4.e.ii: Constrained Particle Swarm Optimization

An optimization scheme is needed to determine the best geometry of the conical nozzle based on the design parameters of throat diameter, conical semi-vertex angle, and expansion ratio to optimize some cost function. The cost function encapsulates the performance of the nozzle and its size. The problem as shown in 4.e.i is discontinuous and nonlinear, meaning derivative-based optimization techniques, such as Lagrange Multipliers and the Pontryagin Principle, can no longer be used. A simple formulation of optimization might be to create a grid of potential solutions made of ranges of acceptable values of the design parameters and checking the optimality of each point in the grid. This becomes cumbersome and computationally expensive for problems with more than two parameters, so a more efficient formulation is necessary.

Particle Swarm Optimization (PSO) is a technique that simulates social behavior in search of a global or boundary optimum condition [4.32]. An initial swarm of “particles” has a position and velocity evenly distributed over the exploration space [4.33]. The position of these particles represents a vector of possible geometric configurations, while the velocity dictates how the position of the particle changes. The velocity is analogous to Genetic Algorithms, in which mutations move the particle to a new position to evaluate the cost function. At each fictitious time step, the velocity moves the particle to a new position and the cost function is evaluated. The cost function entails weighted factors for specific impulse, thrust, and nozzle length. Each particle stores its history on the best position to optimize the cost function, while there is also a global best solution which is the best of each of those individual particle’s best solution.

Constraints add complexity to the problem. As the nozzle design algorithm is not based on an actual fluid-flow analysis and only utilizes losses to an otherwise isentropic process, constraints must be in place to ensure the nozzle will actually perform as intended. The main concern is in flow separation at the nozzle throat, as a sharp change in curvature may cause separation. To control this, a constraint is place on the semi-vertex angle to be limited from  $10^\circ$  to  $35^\circ$ . If the design settles on the upper limits of semi-vertex angle, further investigation is needed in the next portion of design for the convergent section and throat radius of curvature and analysis in a CFD program. Knowing the constraints and cost function, the optimization can be formulated as

$$\min(f(\vec{x})), \quad \vec{x} \in S \in \mathbb{R}^n$$

Where  $n$  is the number of design parameters, and subjected to the  $m$  number of constraints

$$z_i(\vec{x}) \leq 0, \quad i = 1, \dots, m$$

$$z_1 = 50 - d_{throat}(\mu - meter) \leq 0$$

$$z_2 = d_{throat} - 1000(\mu - meter) \leq 0$$

$$z_3 = 10^\circ - \sigma \leq 0$$

$$z_4 = \sigma - 35^\circ \leq 0$$

$$z_5 = 5 - \varepsilon \leq 0$$

$$z_6 = 50 - T(\mu N) \leq 0$$

Where  $\sigma$  is the semi-vertex angle,  $d_{throat}$  is the diameter of the throat,  $\varepsilon$  is the area ratio, and  $T$  is thrust, with a cost function

$$F(\vec{x}) = -\alpha_I * I_{sp} + \alpha_l len$$

Where specific impulse  $I_{sp}$  is measured in seconds and the length of the nozzle  $len$  is measured in milli-meters. The minimum will be approached with a more efficient nozzle with high thrust and small length. The scaling parameters  $\alpha$  ensure the efficiency and thrust produced are weighted as more important than the length. The values of efficiency and length are of the same order when measured on the correct scales ( $I_{sp}$  in seconds, length in milli-meters).

The constraints on throat diameter limit microfluidic effects (keeping the assumption on Knudsen number valid) while maintaining small dimensions. Constraints on semi-vertex angle minimize the possibility of flow separation due to sharp changes in geometry. Constraints on expansion ration ensures the flow will be supersonic with a high enough pressure expansion ratio. The thrust constraint ensures the robot will have enough thrust to hop on the surface. There is no upper limit on thrust, as the chamber pressure will be able to be reduced to produce a lower thrust. This is more important for the attitude control of the robot, as smaller impulse bits lead to more accurate control with reduced chattering.

A common method to deal with constraints is a penalty function, which transforms the problem from constrained to unconstrained and established techniques are utilized. If the constraints are not met, the cost function is a non-optimal value. This selectivity means that the search space is split into feasible and non-feasible spaces. The difficulty is in prescribing the penalty value, where too low of a penalty and particles might find optima in an unfeasible region; too high of a value, and particles might randomly jump to a feasible region and converge to a local optimum [4.34]. To overcome this issue, a dynamic penalty function is used in which the penalty for searching in an unfeasible region is increased over time to allow adequate searching at the beginning of the algorithm [4.35]. An augmented cost function is used [4.32],

$$f(\vec{x}) = F(\vec{x}) + h(k)H(\vec{x})$$

Where  $h(k) = k\sqrt{k}$  is the dynamic modification to the penalty,  $k$  is the algorithm's current iteration, and  $H(\vec{x})$  is the penalty,

$$H(\vec{x}) = \sum_{i=1}^m \theta(q_i(\vec{x}))q_i(\vec{x})^{\gamma(q_i(\vec{x}))}$$

Where  $q_i(\vec{x}) = \max\{0, z_i(\vec{x})\}$ ,  $i = 1, \dots, m$  is the relative violated function of the constraints,  $\theta(q_i(\vec{x}))$  is the multi-stage assignment function, and  $\gamma(q_i(\vec{x}))$  is the power of the penalty. The multi-stage assignment portion means that the more violated a constraint is, the higher the penalty, rather than some arbitrarily large non-optimal value assigned [4.36]. With influence from *Yang et al.*, the multi-stage values can be assigned as

$$\theta(q_i(\vec{x})) = \begin{cases} 10, & q_i(\vec{x}) \leq 0.001 \\ 20, & q_i(\vec{x}) \leq 0.1 \\ 100, & q_i(\vec{x}) \leq 1 \\ 1000, & q_i(\vec{x}) > 1 \end{cases}$$

Due to numerical accuracy, a constraint is considered violated if  $z_i(\vec{x}) > 10^{-5}$ . This multi-stage penalty increases the penalty for being further and further from the constraint. The powers of the penalty are

$$\gamma(q_i(\vec{x})) = \begin{cases} 1, & q_i(\vec{x}) < 1 \\ 2, & q_i(\vec{x}) \geq 1 \end{cases}$$

The main parameters for the PSO model are inertia weight  $\omega$ , self-confidence  $C_1$ , swarm confidence  $C_2$ , maximum particle velocity  $V_{\max}$ , and swarm size  $S$ . The self-confidence parameter affects how a particle's own experience influences its current trajectory, while the swarm-confidence parameters affects how the best solution in the particle's neighborhood influences a particle's trajectory. "Particles" are potential solutions to the optimum and have position  $\vec{x}$  and velocity  $\vec{v}$ . A population of particles, the swarm  $S$ , is initialized with random position and velocities. The set  $N$  defines points within the swarm considered to be "neighbors". In this formulation, the entire swarm of particles are neighbors,  $N = S$ . The particles also have memory, comprising the best fitness to the cost function that the individual particle has experience  $\vec{p}(t)$  and the best fitness of the entire neighborhood  $\vec{g}(t)$ . Initially,  $\vec{x}(0) = \vec{p}(0) = \vec{g}(0)$ . This is the portion of the method that behaves as a social simulator, as each particle is able to communicate with its neighbors as to where the best solution is. The particles are globally sharing the experiences together to arrive at some global optimal solution to the cost function. Two numbers  $\varphi_1$  and  $\varphi_2$  determine the influence of the particle's history in velocity updates. To compute the update of position and velocity for the  $j^{\text{th}}$  dimension of the  $i^{\text{th}}$  particle,

$$\begin{cases} v_{ij}(t+1) = \omega v_{ij}(t) + C_1 \varphi_1 (p_{ij}(t) - x_{ij}(t)) + C_2 \varphi_2 (g_{ij}(t) - x_{ij}(t)) \\ x_{ij}(t+1) = x_{ij}(t) + v_{ij}(t+1) \end{cases} \quad (18)$$

The  $i^{\text{th}}$  dimension refers to which particle is updated and evaluated, while the  $j^{\text{th}}$  dimension is in reference to a design parameter of the particle. The algorithm checks the optimality of the solution  $\vec{x}_i$  at each step and updating the  $\vec{p}(t)$  and  $\vec{g}(t)$  positions if necessary. If the new cost changes a small amount, subject to some tolerance, between consecutive candidate solutions, the algorithm is terminated, and the optimal solution has been found. Initial values are selected based on analysis in [4.33] and papers cited within,  $\omega = 0.9$ ,  $V_{\max} = \pm 4$ ,  $S = 20$ ,  $C_1 = C_2 = 1.494$ ,  $\varphi_1 = \varphi_2 = 1$  [4.37]. The only value that changes during the optimization is the inertia factor, which dictates how the particle's previous velocity impacts the new velocity. In general, a high inertia allows exploration of the entire search space, while low inertia allows exploitation of fine-tuning the local area of the particle. By varying this parameter to be large at the beginning of the search to small towards the end, the swarm can avoid premature convergence to a local optimum as opposed to the more desirable global optimum while still maintaining a good rate of convergence. Initialization for semi-vertex angle and expansion ratio is a linear distribution across the allowable values, while the throat diameter is a logarithmic distribution due to the orders of magnitude of allowable values. This distributes the particles as evenly as possible across the search space without the need of a cumbersome initialization algorithm. The algorithm is described by the following pseudo-code:

**Initialize** particle position, velocity, weight parameters, particle and global best costs

**While** termination condition is not met

**For**  $i = 1$  to # particles,

        Evaluate cost function

        Update  $\vec{p}(t)$  and  $\vec{g}(t)$  if necessary

        Update particle velocity

        Update particle position

    Increase iteration count  $k$

**End while**

For this formulation, the termination condition should ensure each particle has reached the neighborhood of the global optimum. A vector of the difference between a particle's most recent best cost function evaluation and its previous best cost function value is stored. When each particle has reached the neighborhood of the global optimum, the norm of the difference vector will be small. The terminating condition is that the norm of the difference vector is  $10^{-3}$ . Figure 4.9 shows how each particle converges to the same global optimum with the particle's best cost function shown at each iteration.

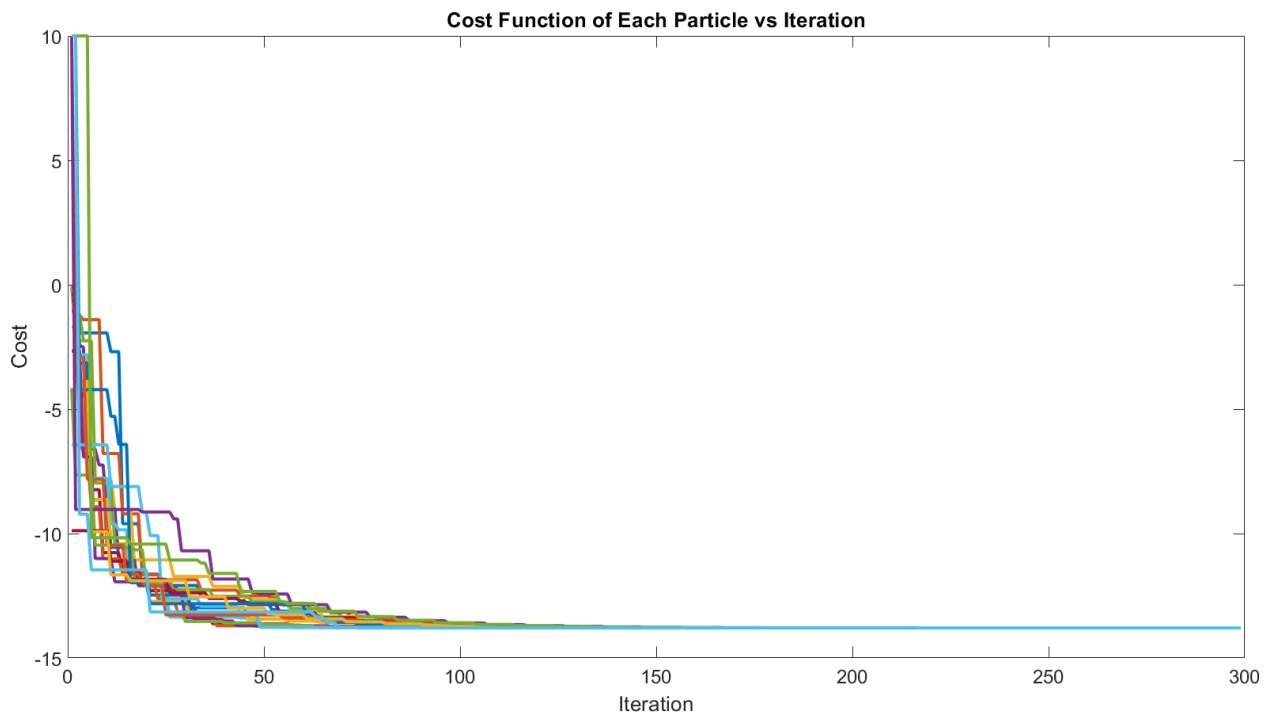


Figure 4.9: Cost Function of Each Particle showing Convergence

#### 4.e.iii: Convergent Section and Throat Geometry Design

Much of the development of micro-nozzles is focused on the divergent section as that has the most impact on performance of the nozzle. However, the other two portions of the nozzle, the throat and converging section, can have a significant impact on the performance of the system as well.

The role of the convergent section is to provide smooth flow to the throat and divergent section. The contour of this section has a minimal impact on performance compared to the throat and divergent section [4.21]. The main design to be done on the converging section is to make it as short as possible without abrupt geometry change and to ensure the flow path is large enough such that the upstream pressure losses do not choke the flow at any region other than the throat. Too steep of a convergent angle would likely cause throat separation as the flow turns and does not “stick” to the nozzle walls. Generally, the convergent angle can be much higher than the divergent angle because the flow is still subsonic in this region. The flow experiences large favorable pressure gradients, and some systems even use almost perpendicular contours to the throat as the convergent section. For each design analyzed, the convergent semi-vertex angle will be  $45^\circ$  and the channel opening will be dictated by the valve designs to be shown in *Chapter 5*.

The throat diameter has been determined through the nozzle optimization code described previously in this chapter. The geometry can still be modified by adding curvature to the throat in the aim of reducing sharp geometry changes for smoother flow with favorable pressure gradients. Analytical methods are not available to optimize the throat curvature, but in general, any added curvature provides a thinner boundary layer. The throat is designed to have a radius of curvature equal to half the throat radius to minimize the change in geometry to the divergent section. The curve is smoothed to meet tangentially to the convergent and divergent sections with as small of a discontinuity as possible.

#### 4.f: Computational Fluid Dynamics

Computational Fluid Dynamics (CFD) simulations are used to further refine previously developed models to predict nozzle performance. An actual fluid flow model can help visualize how the flow develops and potential areas that need to be redesigned. These can include investigating boundary layer growth which might necessitate a shorter nozzle, flow separation at the throat or downstream, and plume analysis.

The geometry of the problem is a 2D fluid domain with modeling for the nozzle and ambient regions. Only half of the nozzle is modeled as it is a symmetric problem and reduces simulation computational time. The geometry is created as a face in SolidWorks and imported into ANSYS Fluent. The nozzle as designed from the optimization process is split into the inlet region, converging region, and divergent region. The exhaust is split into the main exhaust region and far field (Figure 4.10). This enables refining the mesh in more important regions, such as the throat compared to the far field.

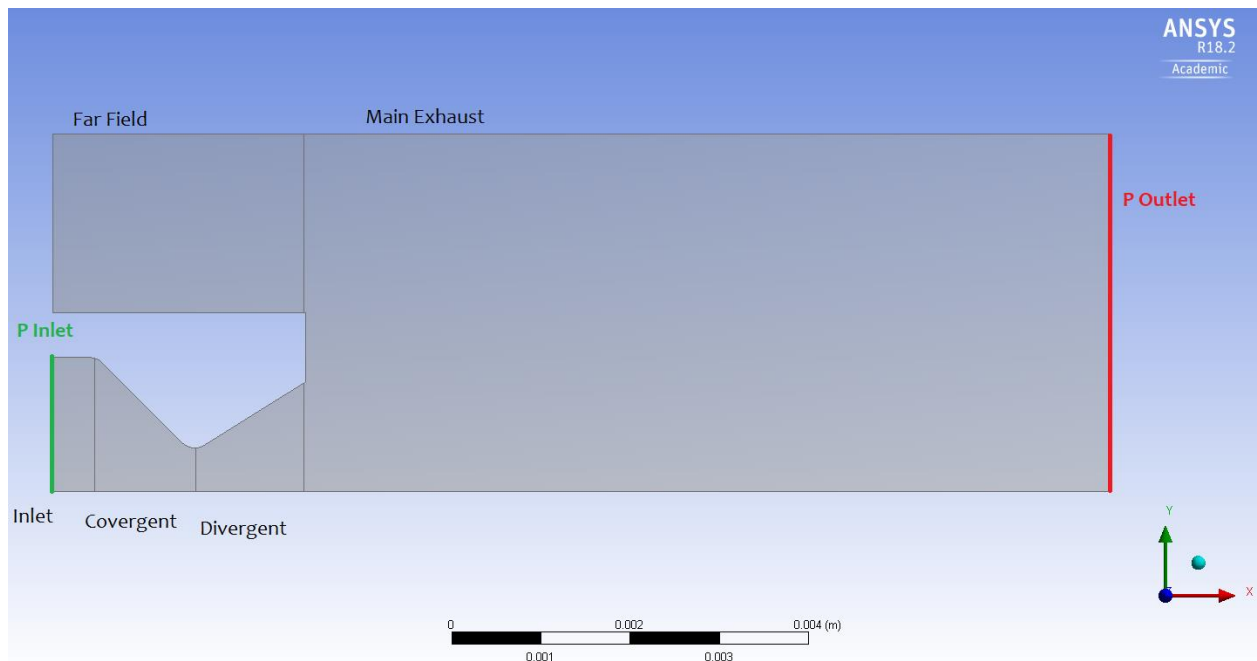


Figure 4.10: Nozzle CFD Geometry

The next step in the process is to mesh the geometry. A bias is applied within the nozzle to make the mesh denser around the wall and less dense along the symmetry axis. The mesh in the exhaust region is made to be less dense, and even sparser in the far field region to reduce run time in these less important regions. The resulting mesh is shown in Figure 4.11.

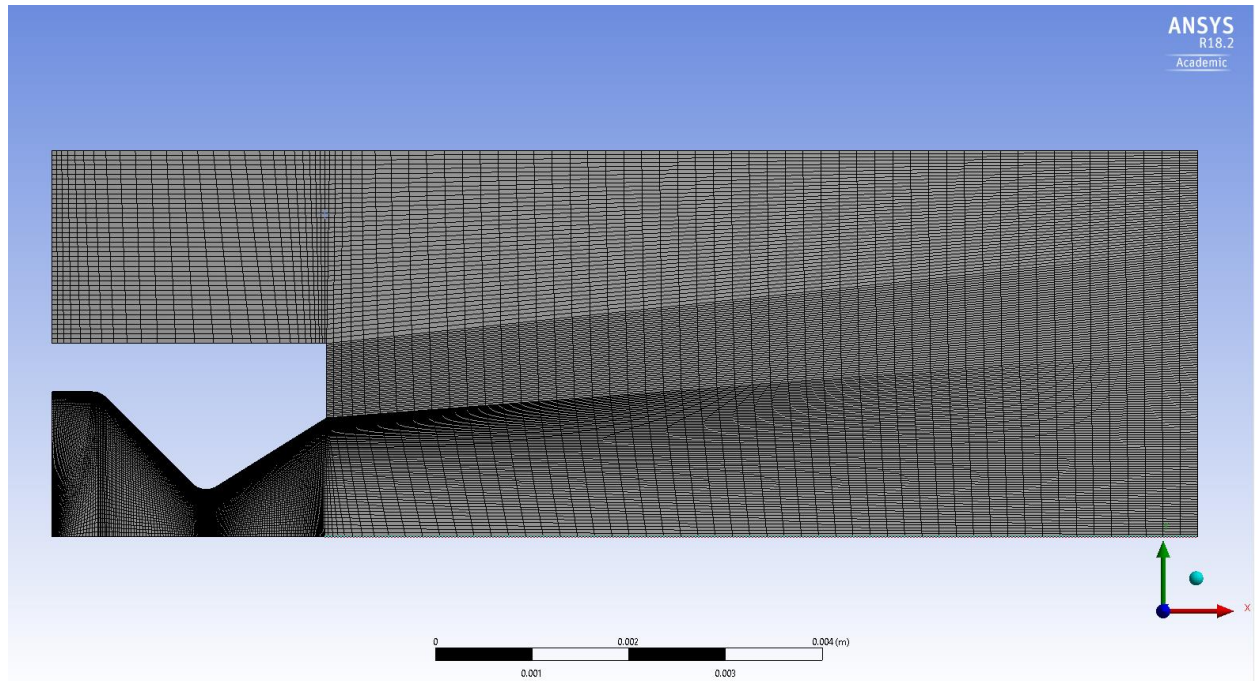


Figure 4.11: Nozzle CFD Mesh

The problem is now ready to set up working fluid, input conditions, and to select a turbulence model. The pressure inlet is set to slightly less than the total chamber pressure assuming the fluid is already flowing at this point. The pressure outlet is set to vacuum conditions. The symmetry axis is set as a symmetrical boundary condition, while the two walls are set as wall boundaries.

The turbulence model is an important consideration that dictates validity of the model. Turbulence models are based on Reynold's Averaged Navier Stokes (RANS) methods, notably the k-omega and k-epsilon models. Essentially, a k-epsilon model predicts well near the vicinity of a wall, while k-omega predicts well when away from the wall. *Menter* first devised the SST model which is a combination of these two models so boundary layer flow and flow way from the walls can be accurately predicted [4.38]. This model also tends to fix the overpredicted flow separation of the k-omega model. Thus, the SST k-omega model is used in ANSYS Fluent.

The setup parameters are modified for this specific application. The Solution is density based with the energy equation on. The turbulence model uses the Transition SST model for the reasons stated above. Nitrogen is used as the working gas with a Sutherland viscosity model, polynomial specific heat model, and ideal gas density model.

The boundary conditions are set as pressure conditions with the pressure inlet set to 0.5 bar and 400 K with nitrogen as the working fluid. The pressure outlet is set to near vacuum

The solution is modified to be second order upwind in flow, turbulent kinetic energy, and turbulent dissipation rate gradients. Convergence criteria are set to  $10^{-4}$  for accuracy. A standard initialization calculated from the pressure inlet is used. The simulation is initialized and set to 5500 iterations. The Mach number is plotted in Figure 4.12, with residuals well within tolerance shown in Figure 4.13.

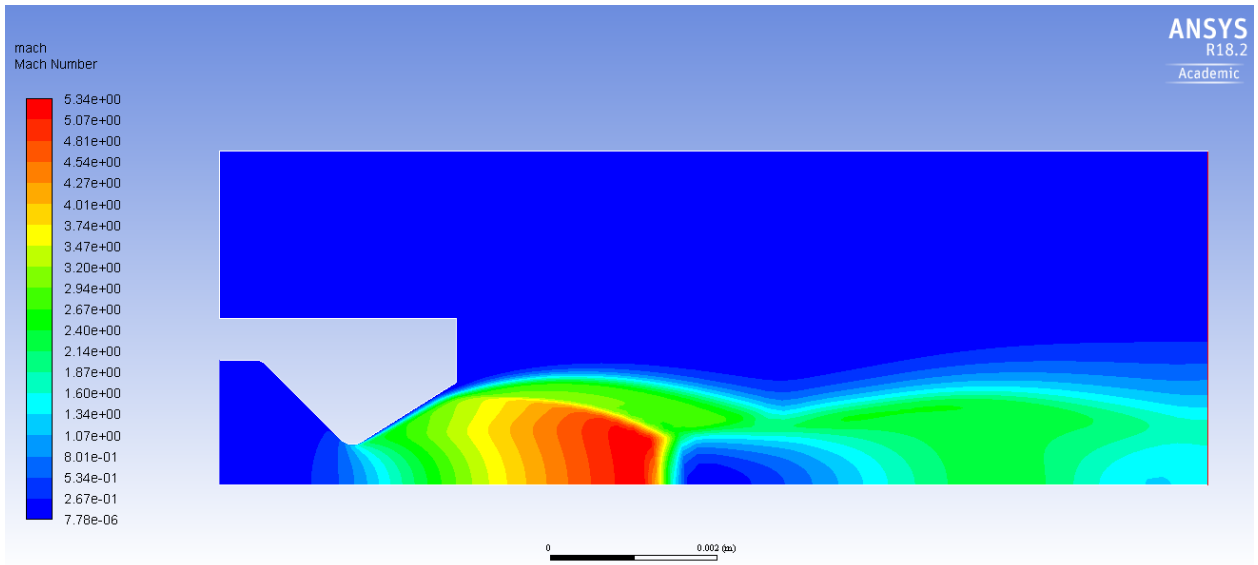


Figure 4.12: Mach Number Plot

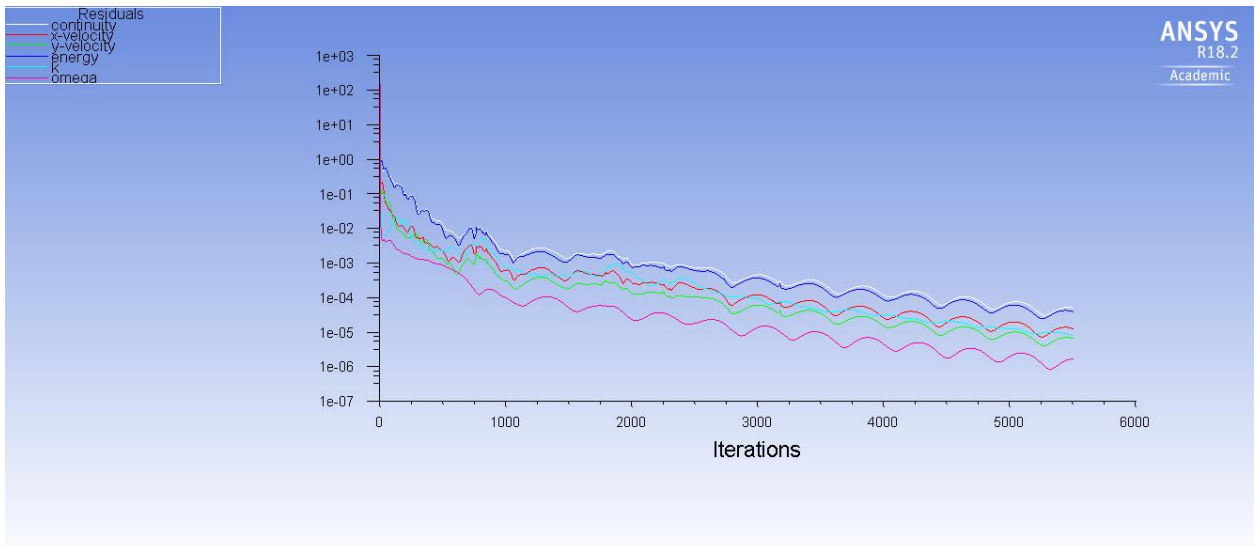


Figure 4.13: CFD Residuals

From Figure 4.12, it can be seen that the flow reaches sonic condition at the throat and is under-expanded at the exit, as expected for vacuum ambient conditions. There is a large bow shock directly downstream of the maximum Mach location with expansion fans propagating downstream. There is no flow separation at the throat, meaning the throat radius is sufficient. The thrust profile as a function of distance from the centerline is presented in Figure 4.14.

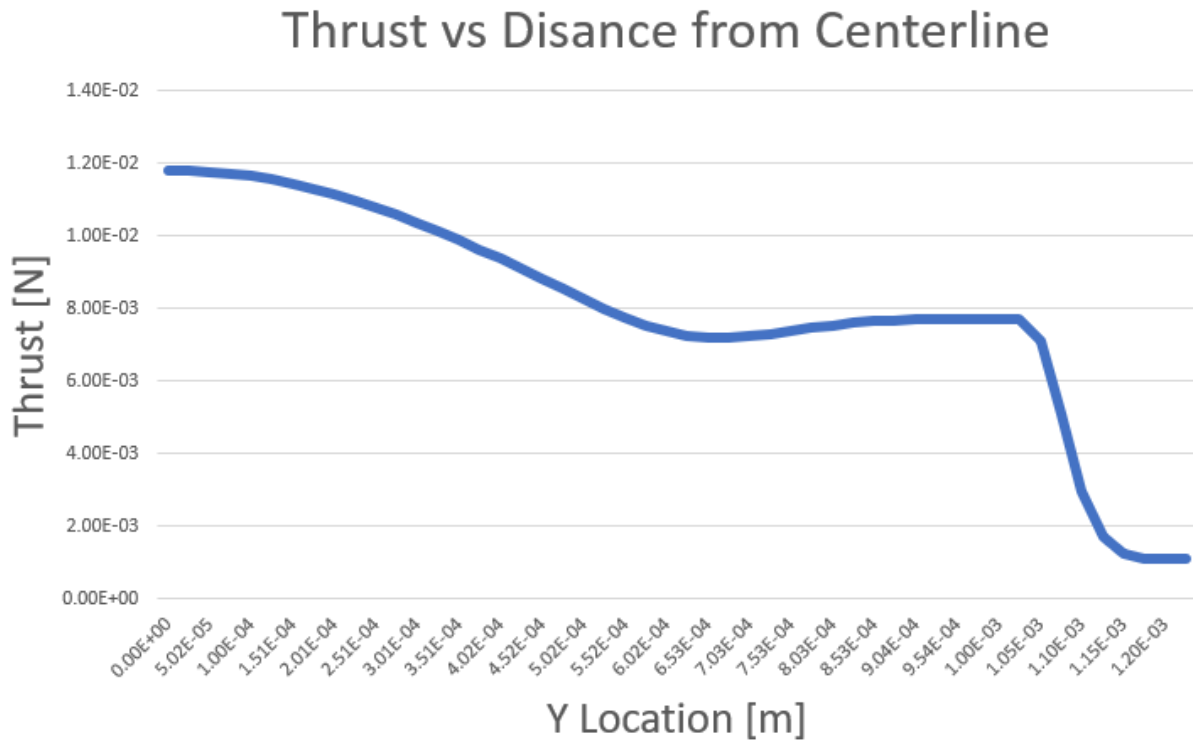


Figure 4.14: Thrust Profile along Nozzle Exit

The results from Fluent, being axial velocity, pressure, and density, are exported and analyzed for mass flow rate and thrust. The results are shown in Table 4.6.

| Parameter        | Value                     | % error |
|------------------|---------------------------|---------|
| Thrust           | 8.02 mN                   | 19 %    |
| Specific Impulse | 64 s                      | 10.1 %  |
| Mass Flow Rate   | $1.05 \cdot 10^{-5}$ kg/s | 17%     |

Table 4.6: CFD Results of Micronozzle

All values are within 20% from CFD results to the quasi-isentropic flow analysis. It appears there are extra losses not captured in the analysis presented in *Section 4.e.i* that can be accounted for when nozzles are fabricated and tested. Ideally, the models should be within 10% error from each other.

#### 4.g: Nozzle Fabrication Methods to Explore

Multiple methods exist to manufacture the micronozzles. The goal of manufacturing is to produce a silicon micronozzle chip with an array of desired micronozzles in a desired arrangement. Silicon or glass are desired for easier integration with other valve chips, though the thermal conductivity could contribute to a loss in efficiency.

The two major considerations for nozzle fabrication are geometry control and surface finish. Each nozzle must adhere to the desired geometry for the convergent section, throat, and divergent section while producing minimal surface imperfections. Proper sizing of the throat will produce the designed mass flow rate, while the correct geometry for the divergent section results in designed pressure ratio and exhaust velocity.

The surface roughness is especially important for features on such small scales because the imperfections are relatively large, potentially to the point of protruding past the boundary layer. A rougher surface will also tend to increase the boundary layer thickness, reducing the effective area of the nozzle. This presents a risk of flow separation and downstream shock waves which would further violate isentropic flow assumptions [4.21, 4.27, 4.39].

Each manufacturing method explored in this section has potential to produce a designed micronozzle to varying degrees of acceptability. The methods discussed will include traditional MEMS techniques, micro-milling, abrasive blasting, and femtosecond laser machining. Some of the most promising methods will be tested to produce single nozzles and then evaluated to determine the best path to manufacture a production chip. Visual inspection will include assessing the fidelity of the original design onto the final part and the surface roughness of the nozzle interior.

Typical MEMS processing uses wet or gaseous chemical etching to remove or bombard desired material according to a certain pattern. This process in general is called lithography. A photolithographic process makes use of polymeric photoresists to first transfer the pattern onto a barrier material, often silicon dioxide for a silicon substrate. Photoresists is a light sensitive polymer that imparts the desired pattern from a mask where UV light penetrates to the exposed areas. For most resist applications, the exposed polymer is washed away when developed to expose the underlying material, called a positive resist. What determines the resists to be positive or negative is that a positive resist scissions the originally cross-linked polymer chains when exposed to UV light, whereas a negative resist forms cross-linked chains when exposed. The underlying surface is then able to be processed.

Chemical etching is used to remove material not protected by the remaining resist layer. A high degree of selectivity is usually favored such that only the desired material is removed and not the photoresist or other surface layers. A wet etching process usually involves highly selective chemicals though the drawbacks of contamination, poor process control, and isotropic nature tends to limit its applications to “noncritical” processes [4.40]. A common wet etching technique is to deposit a surface layer of silicon dioxide onto a silicon wafer and apply the resist on top off that, then etch the silicon dioxide with a diluted hydrofluoric acid mixture. To directly etch silicon in a bulk micromachining process, a solution of hydrofluoric acid, nitric acid, and water is used.

Isotropic etching is a wet etching technique in which the material to be removed recedes at an equal rate in all directions. The examples of the HF and HF-HNO<sub>3</sub> given above are isotropic. Wet etching is usually used for larger features compared to other MEMS fabrication techniques [4.29].

Per Figure 4.16, isotropic etches result in undercutting of the mask layer due to lateral etching and is desirable for certain processes, especially creating cantilever beams.

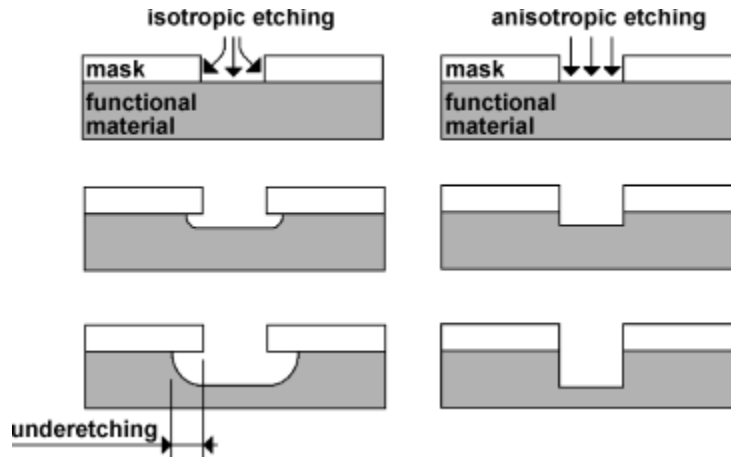


Figure 4.16: Wet Etching

Wet isotropic etching is a perfectly suitable manufacturing method for nozzles. A conical geometry can be created by using concentric masks and leveraging the parabolic side walls (Figure 4.16). By controlling both the window width of each mask ring and the exposure time in the solvent, 3D quasi-conical geometries can be created with small surface imperfections where the influence of one mask ring meets another.

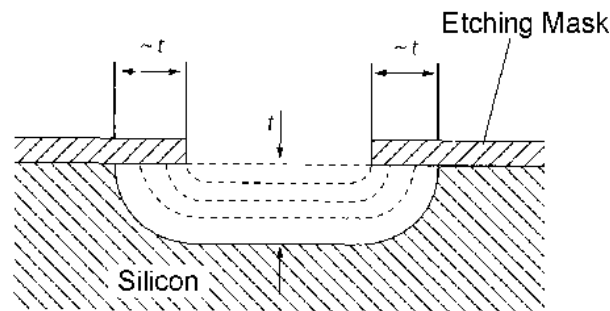


Figure 4.16: Isotropic Etch Single Profile

Anisotropic etching is another wet etching technique to selectively remove material exposed to the etchant chemical. This method is highly dependent on the crystal structure of the substrate. An anisotropic etchant will selectively etch along a specific crystal plane at a much faster rate than the other planes. This method can create sharp and flat geometries. A typical example would be a potassium hydroxide (KOH) etchant, which etches the  $\langle 100 \rangle$  crystallographic plane of silicon much faster than the  $\langle 111 \rangle$  plane, resulting in a 2D cone with semi-vertex angle of  $35.26^\circ$  (Figure 4.17). Due to selectivity of KOH, silicon nitride is commonly used as the masking layer. The downside to this method is that it only creates extruded 2D geometries, so there will certainly be losses from non-axisymmetric effects.

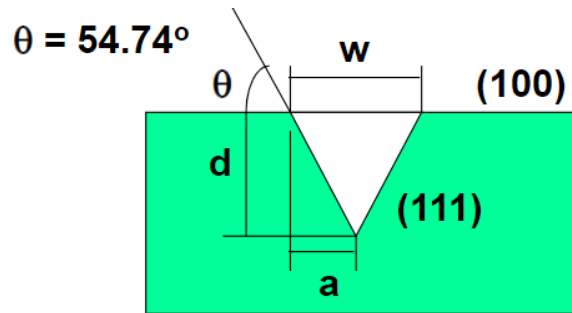


Figure 4.17: 2D Extrusion Cone via Anisotropic Etching

Deep Reactive Ion Etching (DRIE) is a combination of plasma and sputtering etching processes resulting in highly anisotropic and potentially large aspect ratio profiles [4.29]. DRIE involves three steps (Figure 4.18). The first step is to deposit a passivation layer, often octafluorocyclobutane ( $C_4F_8$ ) on the sides and bottom of an exposed area. Then, ions bombard the bottom of the profile to attack and sputter the passivation layer and do so much more effectively than the side walls. This results in the bottom of the profile being exposed. Lastly, the substrate is isotropically etched with sulfur hexafluoride ( $SF_6$ ). This process is repeated many times with each cycle lasting only a few seconds. If the etch time is kept constant through each cycle, a cylindrical cavity is formed with small discontinuities where each layer meets. However, decreasing the etch time of each cycle will create slimmer and slimmer cavities to make a conical cavity. Each cycle usually etches 1 micrometer at a time leading to relatively small surface ripples or “scallops”. This method can produce reliable and accurate dimensions but has the highest cost associated with all the MEMS techniques considered.

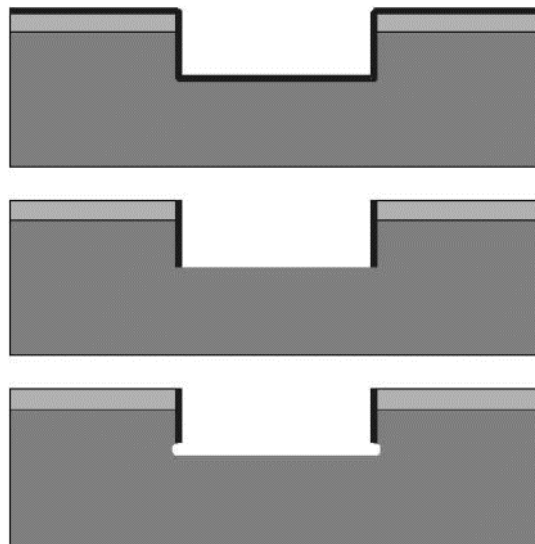


Figure 4.18: DRIE Etching in 3 Steps

Abrasive blasting is gaining increasing traction as a cheap manufacturing method. It relies on blasting the brittle silicon with micro-abrasive particles in an air jet stream. It uses a similar masking concept to etching, in which a mask covers the sections of the workpiece to not have material removed. Abrasive blasting methods are well suited to produce conical nozzles by precise

control of the jet [4.41]. *Achstnick et al.* have developed models that accurately predicts the final surface including roughness of both conical and de Laval nozzles [4.41].

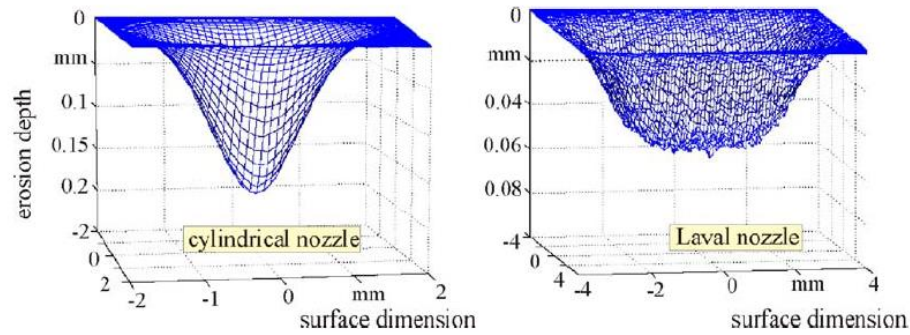


Figure 4.19: Blasting Profiles with a Standstill Nozzle [4.41]

A major downside to using this method is the lack of in-house experience and equipment to prototype the nozzles. Actual manufacturing would rely on entirely outside sources. This would greatly increase the development stage of micronozzles of rues in the propulsion system.

Micro-milling is a mechanical subtractive manufacturing process that removes material by rotating a cutting tool against the stock workpiece. The rotating tool is usually an end mill, commonly ball or tapered end mills. The mill is rotated at high rpm (often >10,000 for micro-milling) by a spindle, which also controls the height of the cutting tool. The workpiece is placed on the worktable, which provides planar control of the workpiece positioning. The high spindle rates must be balanced by ensuring heat transfer to the workpiece is not substantial to cause expansion of the silicon. Milling can create fully 3D conical nozzles for any desired nozzle by rotating the piece over for the convergent and divergent sections.

Complications for micro-milling come about due to the brittle nature of silicon; traditional milling techniques usually result in brittle fractures and large imperfections [4.42]. *Rusnaldy et. al* have discussed many of the difficulties in machining a brittle material at such small scales that must be overcome [4.43]. Without proper control, fractures can propagate tens of microns into the surface of the nozzle as the primary mode for material removal is usually chipping. Ductile regime chipping has been used in silicon but struggles for single-crystal silicon chips. In their work, they detail the setup for obtaining ductile machining and the spindle rate, feed rate, and depth of cut to produce promising contours [4.43]. If ductile-mode machining is not obtained, it is often recommended to use climb-milling instead of conventional-milling for brittle materials [4.44].

Three main control parameters are used for a single type of end mill to influence surface finish. In general, a higher spindle rate, smaller depth of cut, and smaller feed rate per tooth lead to less surface roughness [4.45]. For *Golshan et al.*'s investigation with CBN coated end mills, feed rate had the largest effect while spindle rate requires a large change to significantly affect the roughness. In their work, polished silicon chips were used to mitigate the micro-variations in depth of cut for the top portion that could have induced undesirable chattering. Lower feed rates and depth of cut tend to induce ductile-mode machining [4.45]. *Cai et al.* have developed a method to determine machining parameters based on a new model of acceptable surface characteristics. They have shown new methods in modelling the surface for CFD analysis to better predict what the performance will be before prototypes are tested [4.46, 4.47].

Three methods of fabrication will first be assessed. They include wet isotropic etching, DRIE, and micromilling. These methods are most likely to succeed with repeatability while being accessible.

## 5. Valve Designs

The control of gas flow from the storage chamber to the nozzles is dictated by two sets of valves. The first valve encountered downstream of the storage chamber is the main sealant valve, which should be rapidly actuated with a strong sealing force. This high force provides long term storage and low leak rates, as it could be months to years from initial spacecraft construction to deployment on the asteroid. The second valve is a set of valves to individually actuate each micronozzle. These valves do not require a high sealing force but should still be actuated quickly for more precise robot control. This faster opening would allow for a smaller impulse-bit during attitude control, equating to finer control of the spacecraft's pose. This chapter details the methodology and design of the two types of valves to be used in the micropropulsion system.

## 5.a: Literature Review of MEMS Valves

The low impulse-bit and mass flow rate requirements for micro-nozzles necessitate rapidly actuated and low-leak valves. Valves precisely regulate the fluid's ability to flow to downstream components from the pressurized storage chamber. These actuators must be integrable with other components of the propulsion system to minimize the overall size and mass. Commercially available microfluidic valves do not meet this requirement, thus demanding the design of custom valves. There are six main active MEMS valve actuation methods investigated: shape memory alloys, phase change pinchers, pneumatic pincher, burst, solenoid, and piezoelectric.

Shape memory alloys are materials that can be deformed when at a cold temperature and return to their un-deformed position when heated. SMAs have large force to volume ratios, meaning they are quite well suited to miniaturized valve actuators. Their high energy density also allows for high sealing forces and stroke in a short temperature range [5.1]. *Cheng et al.* have developed a normally-closed SMA valve that operates by applying a current across a nitinol wire, causing a phase change and subsequent contraction of the wire [5.2]. The wire is embedded in a cylindrical plug, connected to deformable PDMS that lifts up and opens a flow channel (Figure 5.1). Another method developed by *Megnin et al.* is to use a planar wire that contracts back to its un-deformed position by electrical heating, causing motion of a spherical plunger (Figure 5.2) [5.3]. This method can be used to make both normally-open or normally-closed valves, the latter requiring assistance of an outside mechanical force that is overcome by the SMA deflecting with enough force to its original position.

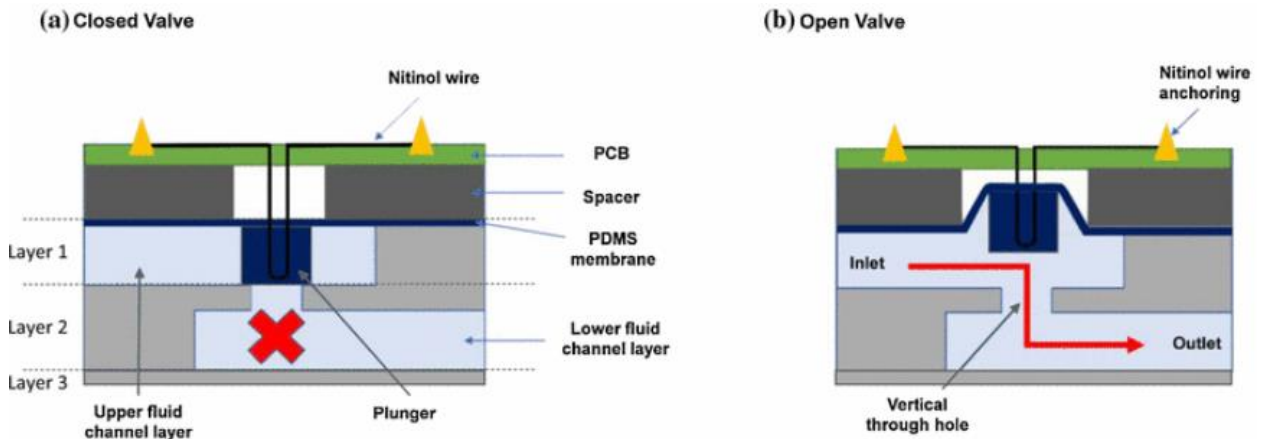


Figure 5.1: SMA Valve 1 [5.2]

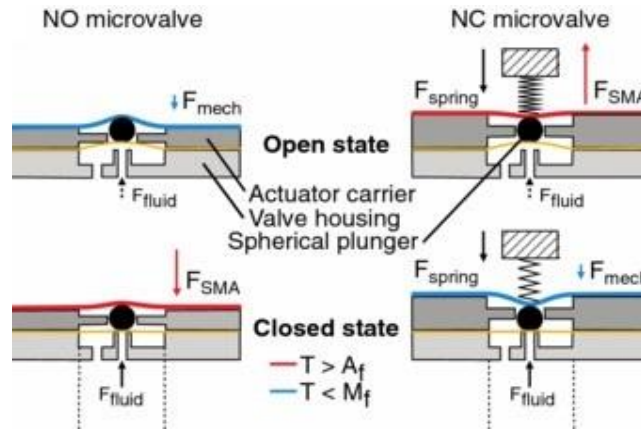


Figure 5.2: SMA Valve 2 [5.3]

Another method of thermal actuation is to exploit solid-to-liquid phase change materials like paraffin wax. Paraffin wax has a low melting point that is easily tunable to fit the environment to be operated in [5.4]. When the wax melts, the volume expands and pinches the flow channel closed (Figure 5.3). The channel is slightly elastic, so the valve can return to its initial open state when needed, unlike earlier phase-change valves that could only operate once. Most phase change valves are normally-open, which exclude them from use in a micropropulsion system that requires normally-closed architectures.

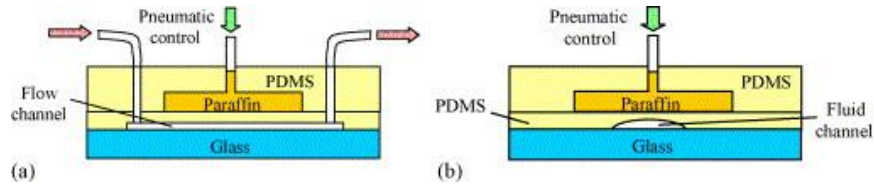


Figure 5.3: Cross Sections (a) along and (b) Across the Flow Channel Paraffin Valve 1 [5.4]

Pneumatic pinch valves utilize similar concepts to the phase change valves, though do not have to be thermally actuated. The pneumatic control line is filled with gas or liquid (to prevent the control fluid leaking into the main fluid line) that exerts pressure on a deformable membrane that can pinch a flow line closed. Most normally-closed pneumatic valves require a vacuum source for actuation, but check valves rely on a different method. They have a constant source fluid flow over the valve with higher pressure exerted on a flap than the fluid to be controlled. By throttling the control fluid, the controlled fluid can overcome the pressure difference and open the flap, allowing flow to the outlet (Figure 5.4) [5.5]. This method relies on laminar flow to prevent mixing of the two fluids. All pneumatic valves are unrealistic for space applications, as they require external pressurization and unnecessary complexity.

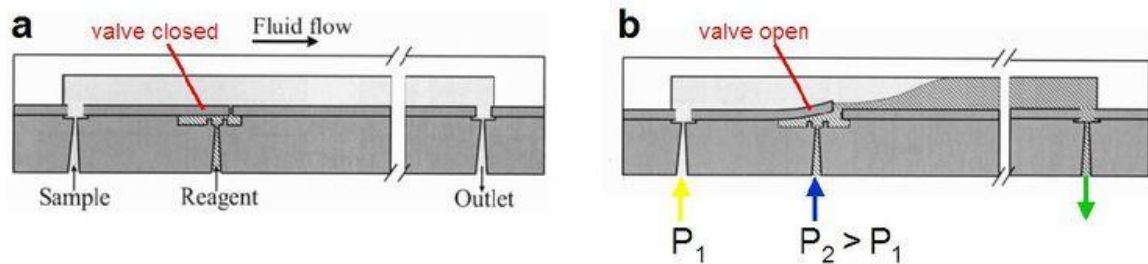


Figure 5.4: Pneumatic Check Valve [5.5]

Burst microvalves are one-time use valves that have been used successfully on a micro-propulsion system, the Micro Solid Propellant Thruster. These valves operated by pressurizing a chamber to the burst limit of a glass membrane, causing the flow channel to open [5.6]. In their design, a solid propellant is either heated directly by resistive heaters (Figure 5.5 a) or indirectly by heating the sacrificial membrane which heats the propellant (Figure 5.5 b). Once these valves are used, they can not be reset and used again, negating the possibility of attitude control.

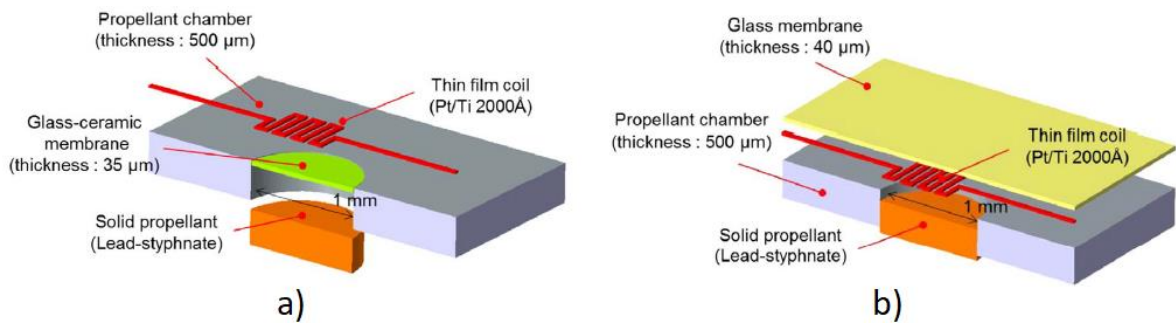


Figure 5.5: MSPT Burst Valves [5.6]

Electrically actuated valves have rapid response times, high sealing forces, and repeatability. They contrast with thermal actuators, which have much slower cycle times and require careful control of ambient temperatures. They are also quite resilient to shock, thermal fluctuation, and vibrations and do not require any cooling systems. Electromagnetic valves usually involve solenoid actuation, inducing a magnetic field to deflect a magnetic and deformable thin film material. They are typically limited to low pressure systems and can achieve response times under 1 milli-second and deflection on the order of tens of microns [5.7]. Work has been done on the development of bi-stable solenoid valves which would reduce power required to very low levels except during operation [5.8]. A cantilever EM valve was designed and tested by *Ren and Gerhard*, showing a low sealing force with high deflection (Figure 5.6) [5.9]. This low sealing force, low power design would be well suited to downstream valves in a cascade sequence, relying on a more robust valve upstream.

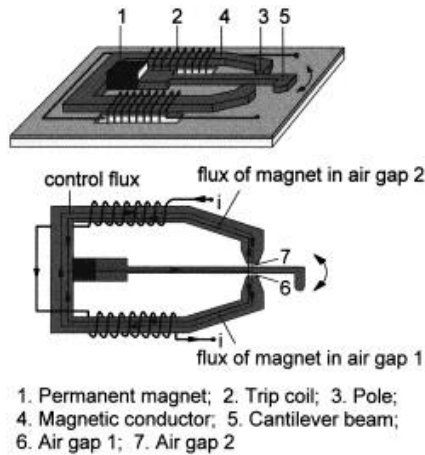


Figure 5.6: EM Valve 1 [5.9]

Piezoelectric devices work by applying a voltage across the piezo crystal to induce mechanical strain and vice-versa [5.10]. Piezoelectric crystals are often stacked together to increase the deflection for a given input voltage to reduce the voltage that needs to be applied [5.10]. Characteristics of these devices include fast actuation, high life cycles before failure, low power consumption, and high sealing forces [5.10]. The low power comes from the fact that an applied voltage is only needed when the actuator is in motion, thus having near-zero power consumption when open or closed.

The two feasible methods of implementing this actuation in a micro-valve are diaphragm and cantilever designs. In a diaphragm valve, the piezoelectric stack is connected to a deformable material, often PDMS, that deflects to open a flow channel between the inlet and outlet ports. An illustration of this is shown in Figure 5.7.

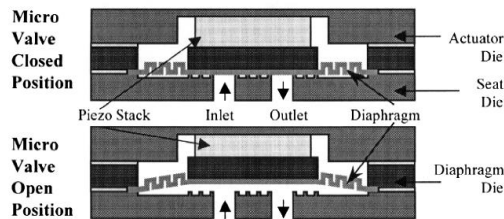


Figure 5.7: Piezoelectric Diaphragm Valve 1 [5.10]

A piezoelectric diaphragm design has three main components: the actuator (piezoelectric stack), diaphragm, and seat. The seat is where the diaphragm presses against while in its normally-closed position. There are various designs explored in [5.10], including a flat surface with non-deformable surfaces and a concept of a series of rings “valleys” to trap particles. This reduces the chances of trapped particles scratching and compromising the sealing surface, which would otherwise encourage further imperfections and increasing leak rates.

Another method to exploit the electro-mechanical diaphragm concept is in having a piezoelectric actuator with an inactive zone sandwiched between two active zones (Figure 5.8) [5.11]. When the two active zones are actuated, they expand upwards. The connected inactive

zone lifts with them, but does not deform, thus releasing it from the seating rings. These rings are used for the same purpose of trapping stray particles and reducing the contact area, thus increasing the sealing pressure. The figure shown is a side view, with the inlet and outlet holes lying in the same plane perpendicular to the picture.

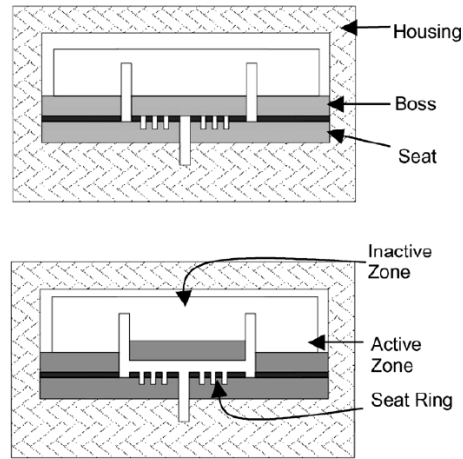


Figure 5.8: Piezoelectric Diaphragm Valve 2 [5.11]

Another piezoelectric valve utilizes cantilever beams instead of diaphragms to achieve larger max deflections than otherwise possible. The main method of actuation is through the transverse effect, in which application of an electric field through the thickness of the beam causes expansion and contraction in the layers along its length. For example, applying a voltage to a layer of piezoelectric material attached to some flexible substrate will cause the layer to elongate or shrink along the beam. If the piezo layer contracts as in Figure 5.9, the beam will deflect upwards. The drawback to the high deflection mechanism is a low blocking force compared to piezo stacks.

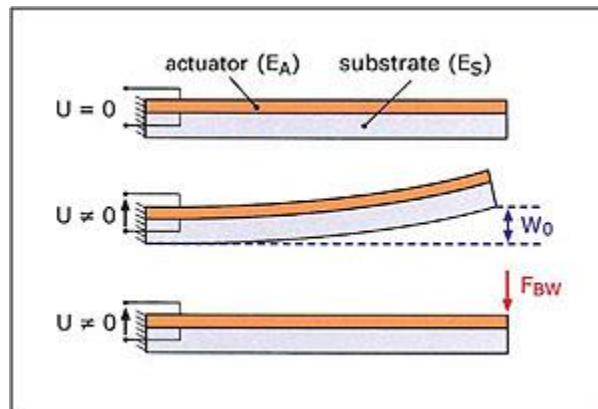


Figure 5.9: Piezoelectric Cantilever Valve

## 5.b: Individual Nozzle Actuation Valves Design and Fabrication Process

From literature review, the most viable option for the individual actuation valves is to utilize the indirect piezoelectric effect for rapid actuation with low hysteresis. The indirect piezoelectric effect is that for certain crystals and polymers, application of an electric field across the material causes strain [5.12]. The two main methods of piezoelectric actuators are diaphragms and cantilever beams. As diaphragms typically give low deflection compared to cantilever beams, the cantilever design is explored.

When heated above the Curie temperature, piezoelectric ceramic and polymer elements exhibit no dipole moment; when below the Curie temperature, the elements transform to a symmetric tetragonal structure with some random dipole moment [5.13]. The piezoelectric material will have no net poling direction despite individual grains (collections of adjoining dipole regions) having a net dipole, meaning no piezoelectric effect can be observed or induced. During the poling process in manufacturing of these actuators, the material is held just below the Curie temperature and a strong electric field is applied. This aligns the majority of the grains to be poled in the same direction, resulting in a net poling direction along the electric field (Figure 5.10).

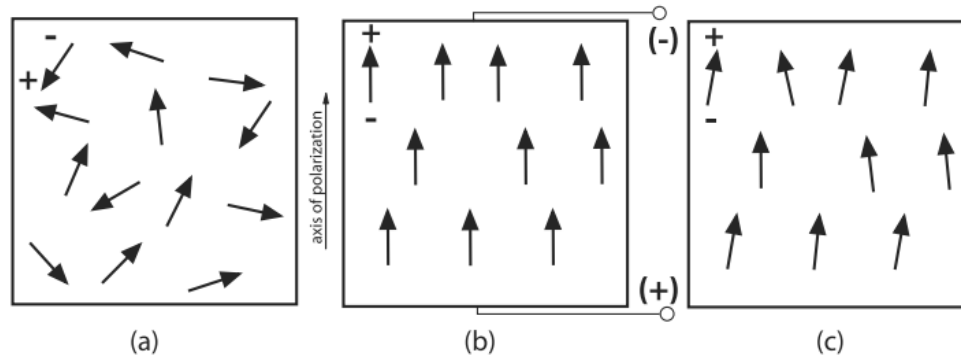


Figure 5.10: Poling process: a) random grain orientation before process; b) large electric field applied to align pole direction of grains; c) net poling after process is complete [5.13].

The piezoelectric material deforms according to the poling direction of the material and the applied electric field. In piezoelectric materials, the application of some gradient field will cause strain (the *indirect* effect), while an electric field can be generated by inducing a strain (the *direct* effect) [5.14]. The direct method is used for sensors, while the indirect effect is used for actuators.

By convention, a cartesian coordinate body-fixed coordinate system is used for the piezoelectric material with the z-axis pointing along the poling direction (Figure 5.11) When considering materials common for piezoelectric actuators, such as lead zirconate titanate (PZT), application of an electric field parallel to the poling direction causes elongation along the poling direction and contraction of the x-y plane. Conversely, applying an electric field anti-parallel to the poling direction causes contraction along the z axis and elongation in the x-y plane [5.15]. This is not a coupled effect due to the Poisson effect relating transverse and axial strain; rather, it is due to the piezoelectric strain coefficients, relating applied voltage to induced strain.

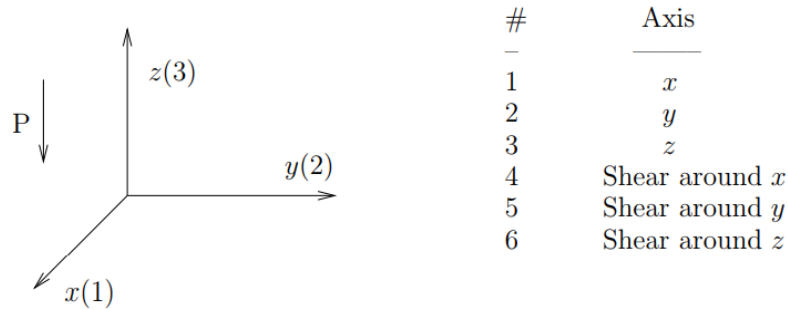


Figure 5.11: Axis Convention

The coupling between mechanical strain and applied electric fields is shown in the constitutive equations. The equations describing coupled electromechanical effects for linear piezoelectric materials (in Einstein notation) are

$$\varepsilon_i = S_{ij}^E \sigma_j + d_{im} E_m \quad (5.1)$$

$$D_m = d_{mi} \sigma_i + \epsilon_{ik}^\sigma E_k \quad (5.2)$$

Where  $\varepsilon$  is the strain vector,  $D$  is the electric displacement vector,  $S$  is the compliance tensor,  $\sigma$  is the stress vector,  $d$  is the piezoelectric strain matrix,  $E$  is the applied electric field, and  $\epsilon$  is the permittivity of the material. The superscripts  $E$  and  $\sigma$  refer to the coefficients being measured at constant electric field and stress, respectively. The indices  $i, j = 1 \dots 6$  and  $k, m = 1 \dots 3$  refer to the direction as defined in Figure 5.11.

The piezoelectric strain matrix  $d_{mi}$  relates the applied electric field in the  $m$  direction to the induced strain in the  $i$  direction. For piezoelectric materials considered, most of the components are zero. The non-zero components are longitudinal (along the poling direction)  $d_{33}$ , transverse  $d_{31}$  and  $d_{32}$ , and shear  $d_{24}$  and  $d_{15}$ . For transverse isotropic ceramics, such as PZT, the constants in the transverse direction are equal and further simplified,  $d_{31} = d_{32}$  and  $d_{15} = d_{24}$ . Because piezoelectric materials are typically thin films, there is no plane stress.

The elastic compliance tensor  $S_{ij}$  relates the strain in the  $i$  direction to the stress in the  $j$  direction. It is the inverse of the stiffness tensor in Hooke's Law,

$$\varepsilon_i = S_{ij} \sigma_j \quad (5.3)$$

By convention, subscripts 1,2,3 refer to normal stress and strain, while subscripts 4,5,6 refer to shear stress and strain. There are three modes of actuation to exploit the electromechanical coupling of strain and electric field to bend a piezoelectric beam: longitudinal, transverse, and shear bending (Figure 5.12). Elongation (also called extension) and contraction can be achieved using either longitudinal or transverse modes, while pure bending will be achieved with shear modes. To actuate these devices, an electrode is deposited along the face of the film and not on the thin sides. Longitudinal actuation is ruled out as a possibility because it would be too difficult to affix an electrode on the thin face compared to the x-y face, and the electric field is much more predictable when applied through the z axis. They also do not provide nearly as much tip deflection as the other methods.

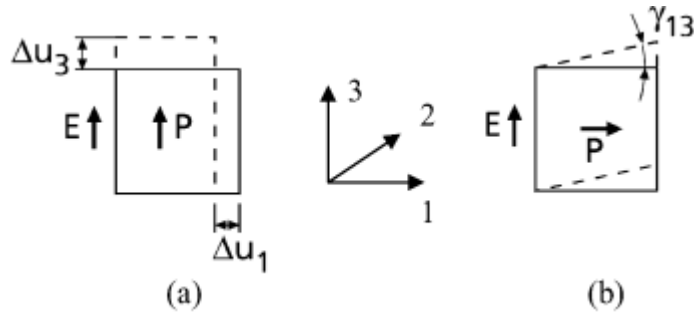


Figure 5.12: a) Longitudinal ( $d_{33}$ ) and Transverse ( $d_{31}$ ) and b) Shear ( $d_{15}$ ) Piezoelectric Effects [5.14]

Using the transverse effect and the  $d_{31}$  coefficient, application of an electric field along the poling axis causes elongation and contraction in the x-axis direction, perpendicular to the poling direction, provided the  $d_{31}$  coefficient is negative. A positive coefficient implies elongation. A single layer of piezo material is free to expand or contract in the other directions as well, though the effect is usually small compared to the tip deflection. The piezo material can be either attached to an elastic substrate or another piezoelectric layer. When one piezo layer extends and the other substrate or piezo layer contracts, the beam curves. Transverse piezoelectric benders can be of three types: monomorph, bimorph, and multimorph. In a monomorph beam, there is only one layer of piezoelectric material fixed to some substrate. Bimorph benders, the most common, consist of two piezoelectric layers joined together or to the opposite sides of some center shim. The center, if necessary, assists in mechanical stability and inhibits potential delamination during large deflections [5.16]. Piezoelectric materials with higher stress levels during deflection can be greatly assisted with a center shim, while lower stress materials, such as polyvinylidene fluoride (PVDF), don't require the extra stability [5.17]. Multimorph beams have more than two piezoelectric layers, and are more complex in modelling, fabricating, and controlling. In these configurations, the piezo layers are still free to expand and contract along the poling axis; however, the strain is small compared to the tip deflection.

Bimorph beams offer significant tip deflection with relatively low complexity. Bimorphs can be connected either in series or parallel with poling directions showed in arrows (Figure 5.13) [5.15]. Both inward and outward series result in the same tip deflection; the only difference is in the electrical configuration. For inward, the poling direction points towards the center of the beam. Outward series beams have poling directions pointing away from the center. The electric field is the applied voltage divided by the thickness of the two layers. A parallel bimorph has an electrode between the two layers. The electric field is the voltage applied divided by the thickness of just one layer.

$$E = \begin{cases} V/H, & \text{series} \\ 2V/H, & \text{parallel} \end{cases} \quad (5.4)$$

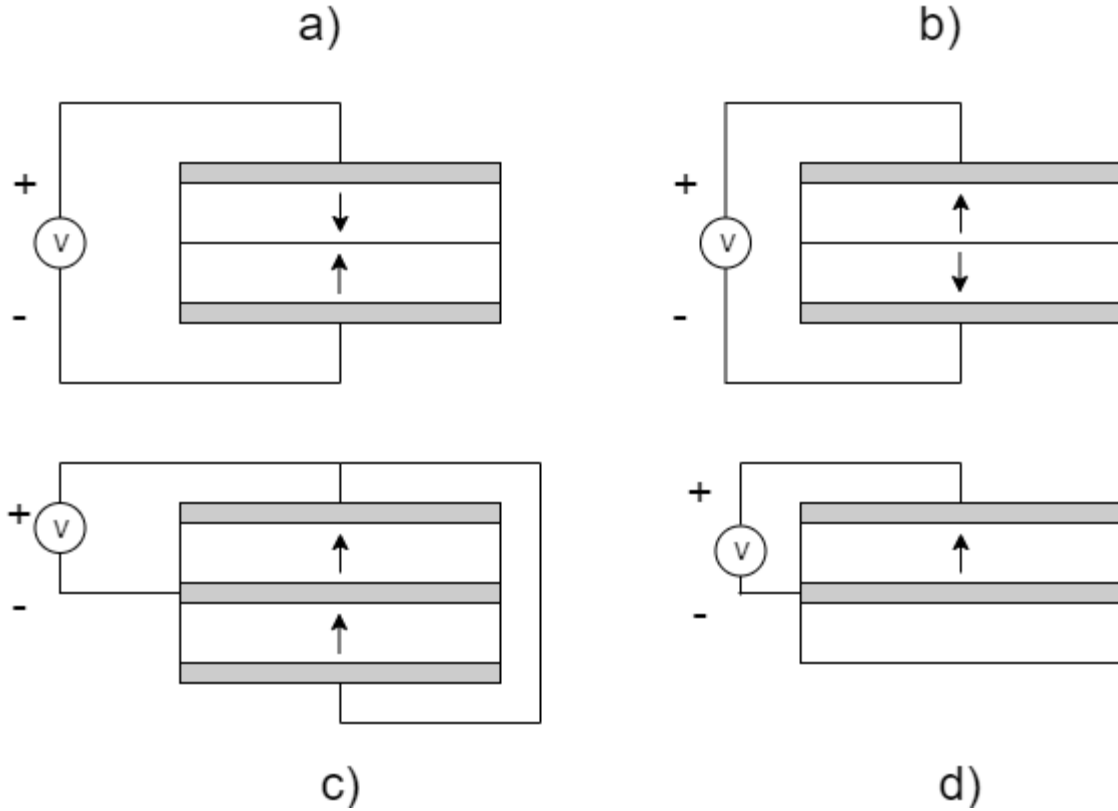


Figure 5.13: Configurations of Bimorph Cantilevers: a) Inward Series; b) Outward Series; c) Parallel; d) Monomorph

For the piezoelectric polymer PVDF, the  $d_{31}$  coefficient is positive, as opposed to most piezoceramics like PZT where it is negative. This means application of an electric field along the poling direction will cause an elongation in the x-axis direction. This is exploited in benders, where PVDF is the common material of choice for transverse bimorph benders. They also lack environmental concerns over lead-based ceramics [5.17].

As derived in *Smits et al.*, the constitutive equation for tip deflection can be calculated for a bimorph transverse actuation piezoelectric beam assuming Euler-Bernoulli theory [5.15],

$$\delta = \frac{3d_{31}L^2}{2H}E \quad (5.5)$$

Where  $\delta$  is the tip deflection in meters,  $L$  is the length of the beam in meters,  $H$  is the height of the beam in meters, and  $E$  is the applied electric field in Volts/m. This derivation assumes a linear evolution of the electric field through the thickness of the piezoelectric layer, which has been found to actually be a superposition of linear and quadratic evolution through the thickness [5.18]. This is from the induced electric field from a mechanical strain. A more complex formulation of the electric field is shown in by *Benjeddou et al.*, which accounts for this effect [5.18],

$$E_{i3} = -\frac{\tilde{\varphi}_i}{h_i} + (z - z_i) \frac{e_{31}^{i*}}{\epsilon_3^{i*}} w'', \quad i = A, B \quad (5.6)$$

Where  $E_{i3}$  is the electric field on the  $i^{th}$  face in the 3-axis direction,  $i$  refers to either the top or bottom piezoelectric layer,  $h_i$  is the thickness of the layer,  $\tilde{\varphi}_i$  is the relative/ difference potential of the layer,

$$\tilde{\varphi}_i = \varphi_i^+ - \varphi_i^- \quad (5.7)$$

$Z$  is the distance from the center of the beam,  $e$  is the piezoelectric stress constant,  $\epsilon$  is the dielectric constant, and  $w''$  is the second derivative of the deflection of a point along the beam. In literature, the induced effect is ignored because it tends to be much smaller than the linear distribution. The model further assumes the electrodes fully cover the face they are attached to and there is negligible variation in the thickness of the electrode and piezoelectric layers.

A shear mode bender utilizes the  $d_{15}$  coefficient. Usually, the piezoelectric material is sandwiched between two elastic materials. In this form, a monomorph shear bender causes tip deflection. An advantage of this formulation is that for the same tip deflection, less internal stress is induced compared to elongation methods [5.19]. However, shear mode benders tend to be more efficient for thicker beams, while transverse beams are more efficient for thin films [5.20]. Transverse materials are also much more developed and well understood. *Poizat et al.* have developed a simple solution to the tip deflection of shear mode beams [5.14],

$$\delta = L\gamma_{13} \quad (5.8)$$

Where  $\delta$  is the tip deflection,  $L$  is the length of the beam, and  $\gamma_{13}$  is the shear angle,

$$\gamma_{13} = d_{15}E \quad (5.9)$$

Where  $E = \frac{V}{H}$  for a monomorph and  $E = \frac{2V}{H}$  for a bimorph. As opposed to extension mode benders, shear benders have a linear change of electric potential through the thickness of the beam [5.14]. For sandwich structures, the elasticity of the sandwich material must be incorporated. In the sandwich structures, tip deflection is linear with applied voltage [5.18].

From simulations in *Poizat et al.*, it is possible to combine the extension and shear effects into an extension-shear bender to create an even larger tip displacement [5.14]. This is done by controlling the angle of polarization,  $\alpha$ . This angle dictates how far displaced the tip poling direction is from vertical (Figure 5.14).

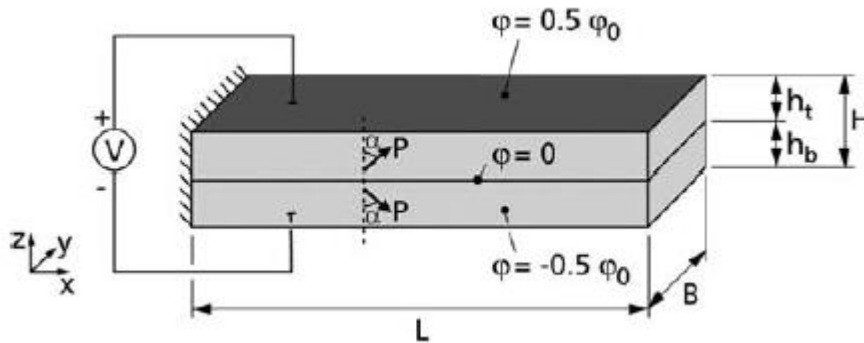


Figure 5.14: Extension-Shear Bender [5.14]

The cosine of the angle refers to the influence of bending modes, while the sine refers to the influence of shear modes (Figure 5.15).

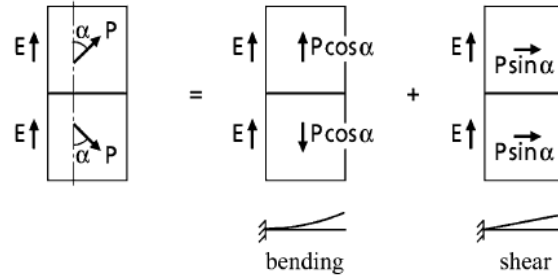


Figure 5.15: Bending and Shear Modes in an Extension-shear Bender [5.14]

By combining the  $d_{15}$  and  $d_{31}$  effects, the tip deflection for an extension-shear bimorph bender can be approximated as

$$\delta = 3d_{31} \frac{L^2}{H^2} V \cos(\alpha) + 2d_{15} \frac{L}{H} V \sin(\alpha) \quad (5.10)$$

For  $\alpha = 0^\circ$ , the result is an extension bender, and  $\alpha = 90^\circ$  is a shear bender. For smaller length-to-height ratios ( $L/H = 5$ ), polarization angle of up to  $\sim 30^\circ$  increases tip deflection. For larger length-to-height ratios, less polarization (less shear actuation) increases tip deflection. Equation 6 is in good agreement with the 3D FEA ABAQUS models developed, as found by *Poizat et al.* [5.14].

The two most commonly used piezoelectric materials in piezo actuators are PZT based and PVDF. To select which material to use for a bender, the electromechanical and material properties first must be compared (Table 5.1). The piezoelectric strain coefficients  $d_{15}$ ,  $d_{31}$ , and  $d_{33}$  relate applied voltage to the developed deformation, in pico-meters per Volt. The coupling coefficients  $k_{15}$ ,  $k_{31}$ , and  $k_{33}$  are measures of the efficiency of converting electrical energy to mechanical energy; the larger the number, the more efficient. The relative permittivity (or dielectric constant, historically)  $\epsilon_r$  is the ratio of absolute permittivity compared to the permittivity of vacuum. Listing the material properties,  $\rho$  is the density,  $Y$  is the Young's modulus, and  $\nu$  is Poisson's ratio.  $T_c$  is the Curie temperature of the material, the point at which the material becomes de-polarized.

From Table 5.1, the most likely candidates for a piezo bender are PZT-5H and PZT-5A. PZT-5H is softer than PZT-5A. These were selected based on the high piezoelectric strain coefficients compared to the other materials. Softer ceramics are more susceptible to stress-induced change, reducing reliability for large strains [5.27]. PZT-5H also exhibits a lower Curie temperature that could be within the operating range of propellants, negating the possibility of using them [5.30]. Per *Hooker*, PZT-5A has reduced piezoelectric strain coefficients, up to 50% decrease, when cooled to  $-150^\circ \text{C}$  [5.30]. The performance steadily increases to the highest temperature tested,  $250^\circ \text{C}$ . Thus, PZT-5A has great performance over a wide range of temperatures, which is necessary for space applications. For these reasons, PZT-5A is the material of choice for the design. Initial sizing for a parallel bimorph extension mode beam is done through Eqn. 5.5. To prevent choking the system in the valve instead of the nozzle, the flow channel through the valve to the nozzle chip should be at least three times the size of the nozzle throat area.

| Property        | Units             | PVDF<br>[5.21 5.22] | PZT-4A [5.23<br>5.24] | PZT-5A [5.24-26 5.29] | PZT-5H [5.24 5.26<br>5.27 5.29] | BaTiO <sub>3</sub><br>[5.26 5.27] | AlN [5.28] |
|-----------------|-------------------|---------------------|-----------------------|-----------------------|---------------------------------|-----------------------------------|------------|
| d <sub>15</sub> | pm/V              | -27                 | 496                   | 584                   | 741                             | -                                 | -          |
| d <sub>31</sub> | pm/V              | 23                  | -123                  | -171                  | -274                            | 78                                | -2.65      |
| d <sub>33</sub> | pm/V              | -33                 | 286                   | 374                   | 593                             | 149                               | 3.4-5.1    |
| k <sub>15</sub> | -                 | -                   | .71                   | .69                   | .68                             | -                                 | -          |
| k <sub>31</sub> | -                 | .12                 | .33                   | .31                   | .39                             | .21                               | -          |
| k <sub>33</sub> | -                 | .15                 | .7                    | .71                   | .75                             | .48                               | .21        |
| ε <sub>r</sub>  | -                 | 12                  | -                     | 1200                  | 3400                            | 1700                              | 9.5        |
| ρ               | g/cm <sup>3</sup> | 1.78                | 7.8                   | 7.75                  | 7.5                             | 5.7                               | -          |
| Y               | GPa               | 8.3                 | 55                    | 66                    | 64                              | -                                 | 345        |
| ν               |                   | .29                 | .3                    | .3                    | .3                              | -                                 | -          |
| T <sub>c</sub>  | °C                | 190                 | -                     | 370                   | 195                             | -                                 | -          |

Table 5.1: Properties of Various Piezoelectric Materials

To achieve this requirement, the tip deflection of beams of various lengths is explored to determine the required width of the opening (Figure 5.16). A rectangular opening is assumed such that the tip deflection and width of the beam should be at least three times the throat area. The throat diameter is assumed to be 1 mm, the upper range of size from *Chapter 4*.

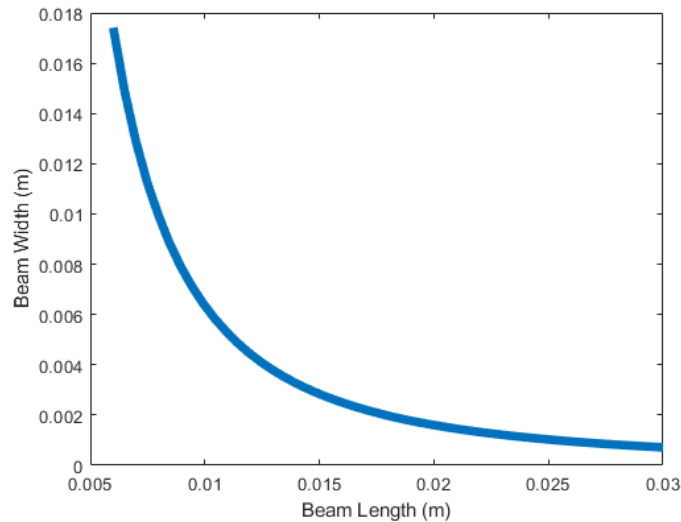


Figure 5.16: Beam Width vs Beam Length to Satisfy Opening Area Requirement

To produce the desired opening size, the minimum area of the piezoelectric element, that is, its length and width, is found that satisfies the opening requirement. A beam length of 1.5 cm, width of 3 mm, and thickness 100 microns is chosen. This results in a tip deflection of 277 microns. Thus, flow channels shall be 3 mm wide to negate geometry changes that would induce pressure

losses. Shown in Figures 5.17-5.19 are the beam deflection, piezoelectric element thickness change, and the voltage distribution of this selected element. The small thickness change compared to the beam deflection shows that effect can be neglected and barely contributes to the opening area.

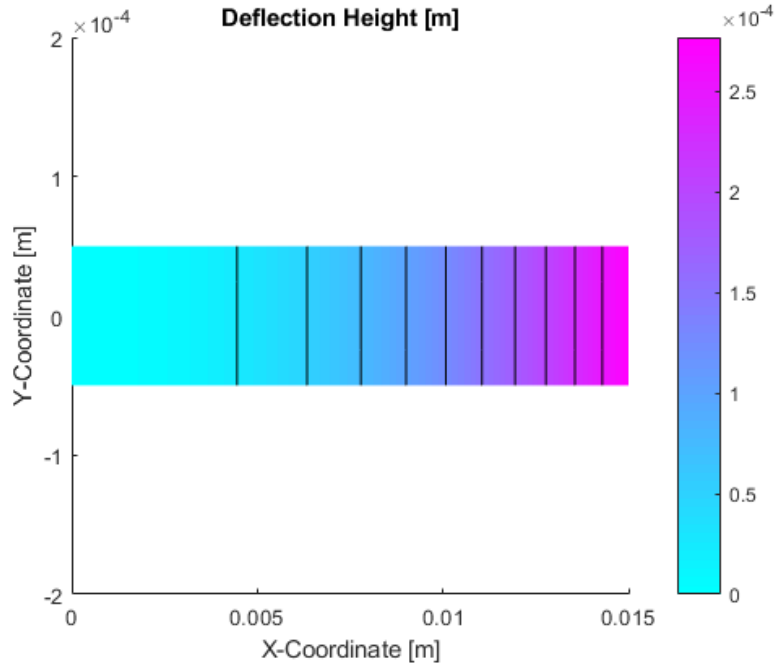


Figure 5.17: Beam Deflection Height

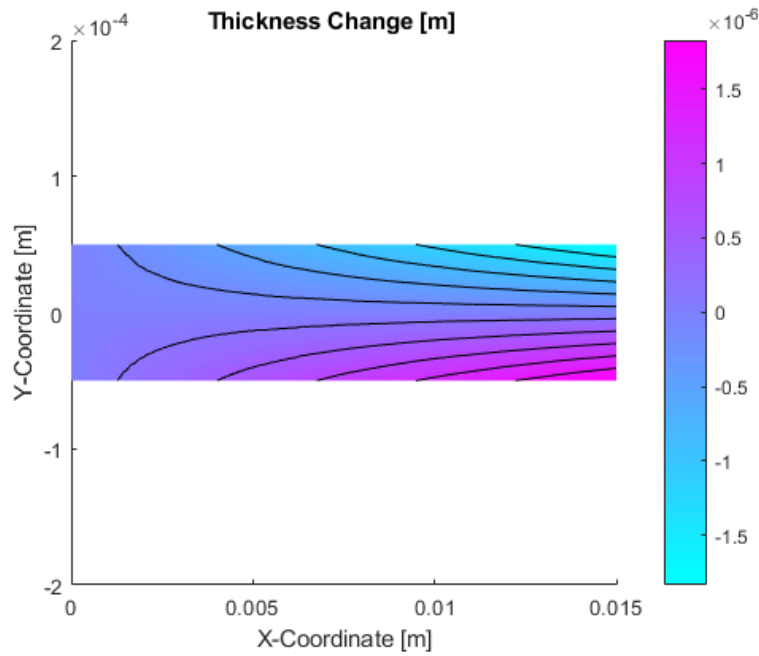


Figure 5.18: Piezoelectric Element Thickness Change

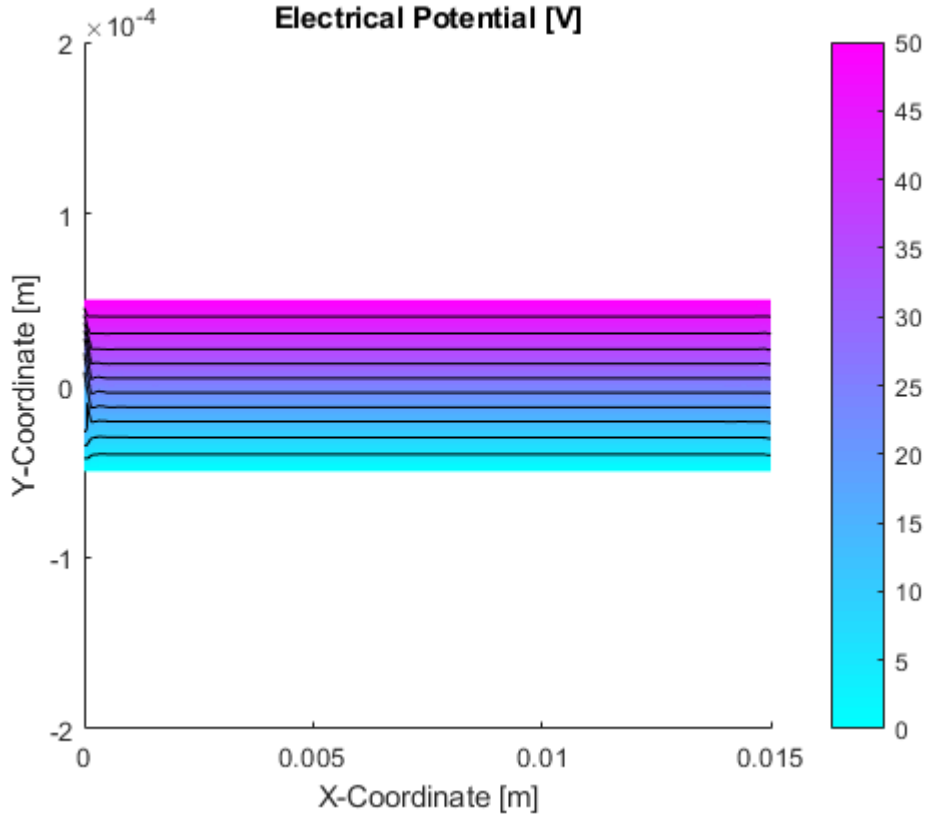


Figure 5.19: Electric Potential Through-Thickness Distribution

To refine the design, a 3D model is required. Further material properties for a z-poled PZT-5A beam are needed per Equations 1 and 2. For the transversely isotropic ceramic, simplifications are:

$$\begin{aligned}
 S_{11} &= S_{22} \\
 S_{13} &= S_{31} = S_{23} = S_{32} \\
 S_{12} &= S_{21} \\
 S_{44} &= S_{55}
 \end{aligned} \tag{5.11}$$

For easier implementation into ANSYS APDL, the problem is reformulated to include the stiffness matrix and piezoelectric stress coefficients [5.14],

$$\sigma_i = C_{ij}^E \varepsilon_j + e_{im} E_m \tag{5.12}$$

$$D_m = e_{mi} \sigma_i + \epsilon_{ik}^\sigma E_k \tag{5.13}$$

Where  $e$  is the piezoelectric stress coefficient. Previous simplifications result in the material matrices for elastic stiffness  $C$ , piezoelectric stress constants  $e$ , and relative permittivity  $\epsilon_r$ ,

$$C = \begin{bmatrix} 99.201 & 54.016 & 50.778 & 0 & 0 & 0 \\ 54.016 & 99.201 & 50.778 & 0 & 0 & 0 \\ 50.778 & 50.778 & 86.856 & 0 & 0 & 0 \\ 0 & 0 & 0 & 21.100 & 0 & 0 \\ 0 & 0 & 0 & 0 & 21.100 & 0 \\ 0 & 0 & 0 & 0 & 0 & 22.600 \end{bmatrix} GPa$$

$$e = \begin{bmatrix} 0 & 0 & -7.21 \\ 0 & 0 & -7.21 \\ 0 & 0 & 15.12 \\ 0 & 12.32 & 0 \\ 12.32 & 0 & 0 \\ 0 & 0 & 0 \end{bmatrix} \frac{C}{m^2}$$

$$\varepsilon_r = \begin{bmatrix} 1728 & 0 & 0 \\ 0 & 1728 & 0 \\ 0 & 0 & 1694 \end{bmatrix}$$

From ANSYS APDL results, the tip deflection would be 283 microns, a difference of 2% (Figure 5.20). Thus, this finite element MATLAB model is a decent approximation for fast results.

```
1
DISPLACEMENT
STEP=1
SUB =1
TIME=1
DMX =.283E-03
```

**ANSYS**  
R18.2  
Academic

OCT 31 2019  
14:19:59



PiezoBimorphBender

Figure 5.20: ANSYS Model of Piezoelectric Bimorph Bender under 50 V

The next portion of discussion is in the fabrication of these valve chips. The final assembly of the valve chip, flow channel chip from the main sealant valve, and the nozzle chip are shown in Figure 5.21.

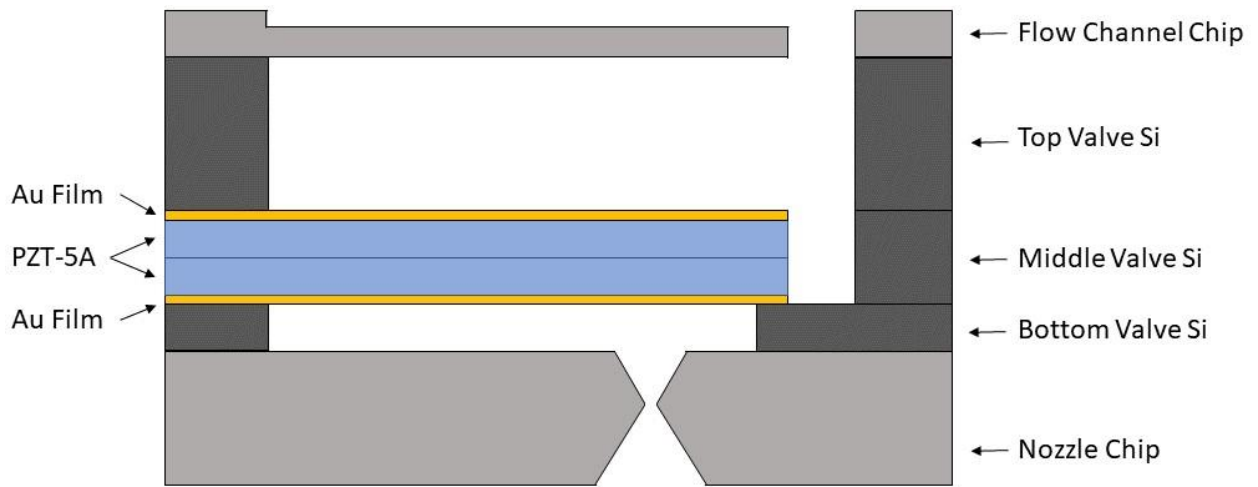


Figure 5.21: Individual Actuation Valve Overview

It is desired to bond the PZT-5A to the silicon substrate at low temperatures because of the difference in thermal expansion. It is difficult to grow sufficiently thick layers (100 microns) by sputtering, sol-gel, or CVD, so the option left is to bond the pre-made, bulk piezoelectric ceramic to Si by using an intermediate layer [5.31]. Otherwise, the temperatures required would degrade some other aspects of the circuitry in the chip. *Sun et al.* have determined that a gold intermediate layer is a good option for the bond strength and conductivity of the film [5.31]. Thus, a thin 1-2 micron film of gold will be used as the intermediate layer and electrodes for piezoelectric actuation. A thicker layer is more conducive to a strong, flat bonding surface for the bulk PZT ceramic.

Gold is used for the eutectic bonding of PZT to Si. The process will follow a procedure outlined in *Tanaka et al.* [5.32]. Firstly, a layer of gold is deposited on both the surface of PZT and Si to be bonded by vacuum evaporation. The two surfaces are put in contact under pressure and on top of a hot plate. The chips are heated to 400-550 °C, during which the poling process of PZT can also occur.

The process of valve chip fabrication is shown in Figure 5.22. Firstly, the silicon nitride sacrificial layer is deposited into the base silicon wafer. Then, the bottom gold film is deposited on the wafer. The PZT bimorph beam with the top gold layer already affixed is then placed on top of the gold film. The assembly is then eutectic bonded together. After this, the middle silicon wafer with an etched cavity with borosilicate glass on top and bottom is positioned over the bottom wafer and anodic bonded. The top silicon wafer with a cavity for the beam to deflect into is then positioned and anodic bonded. The combination of these three silicon wafers provides clamping conditions on one end of the beam with sufficient room for the gas to flow and the beam to deflect. The final two steps are to etch the bottom flow channel of the chip and the silicon nitride to lift the free end of the beam. The valve chip is then ready for integration to the nozzle wafer and flow channel wafer, assuming gold bonds have been integrated for interfacing with the voltage supply control.

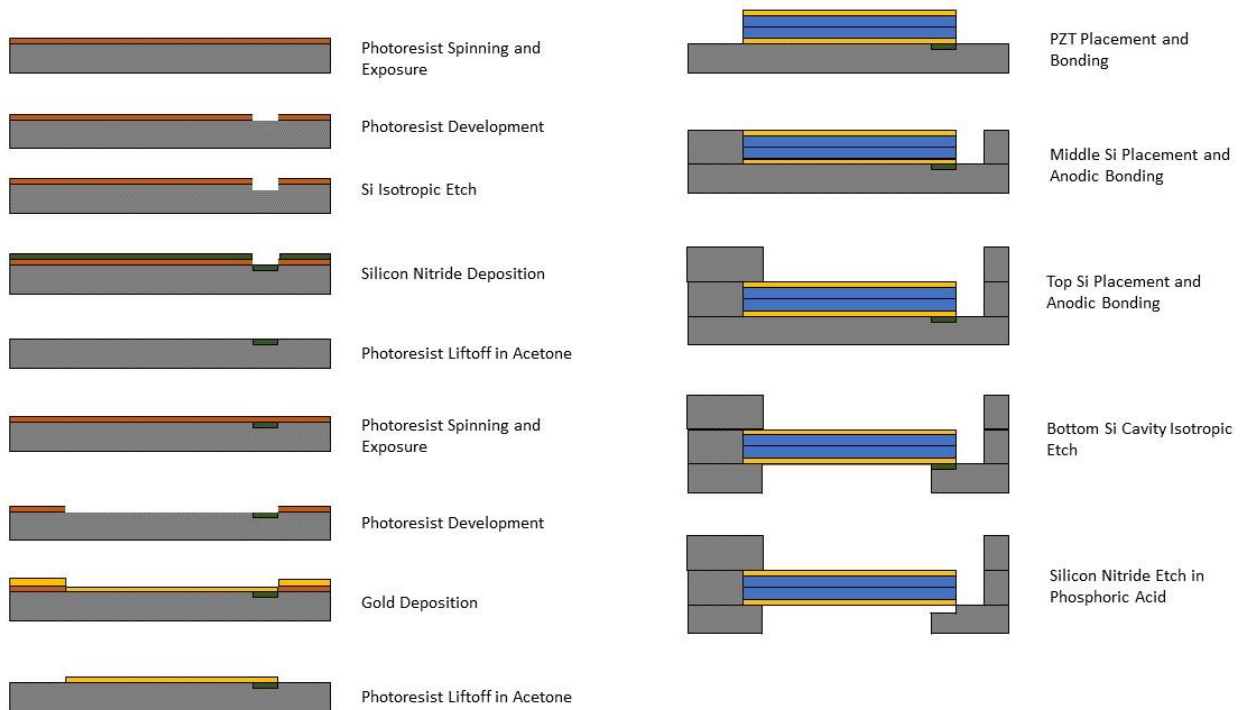


Figure 5.22: Valve Chip Fabrication Process

Once the valve chip is complete, it can be bonded to the nozzle chip and flow channel chip. Both cases involve a Si-Si wafer bond. Annealing is to be avoided to prevent raising the piezo elements above their Curie temperature, leaving anodic bonding as a suitable choice. A borosilicate layer is sputtered onto the bottom of the valve chip and placed in contact with the nozzle chip and bonded at 300° C. Then, glass is sputtered onto the top side of the valve chip and bonded to the flow channel chip. Thus, the full assembly of the valve chip to the nozzle and flow channel chips is complete.

### 5.c: Main Sealant Valve Design and Fabrication Process

The main sealant valve provides long term storage for the propulsion system with low leak rates while enabling rapid actuation during firing. The main sealant valve will also rely on piezoelectric actuation for much of the same reasoning for the individual actuation valve. The difference lies in that this valve does not exploit piezo benders which tend to have much lower sealing forces. Instead, this actuator uses a stack of elements that deflect longitudinally to the applied voltage. A cross section of the valve is shown in Figure 5.23.

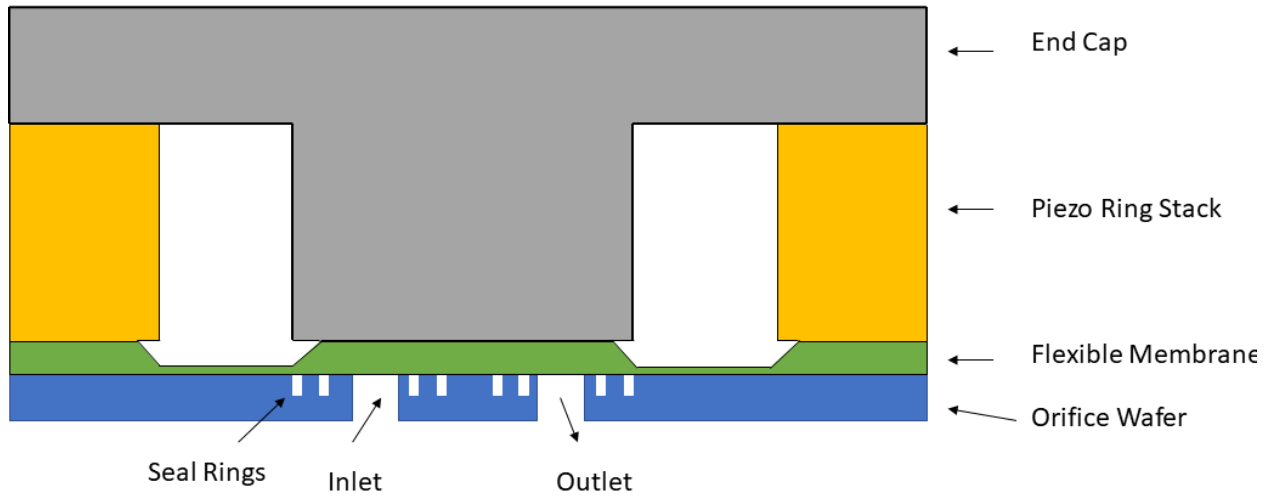


Figure 5.23: Piezoelectric Ring Valve

This valve operates using a stack of piezoelectric rings connected to a rigid end cap on their top and a flexible membrane on the bottom. The end cap is bonded to the flexible membrane in the middle of the valve. When actuated, the piezo stack extends upwards. This motion drives the end cap upwards, which bends the flexible membrane. When the membrane flexes, it opens a flow channel from the inlet to the outlet in the orifice wafer. Seal rings are etched into the orifice wafer layer to increase the sealing pressure and provide a trap for particles that may leak [5.11]. This decreases leak rates and extends mission lifetime by reducing micro-abrasions from trapped particles.

Circular actuators do not experience large stress concentrations like rectangular stacks do at their sharp corners. The force is applied uniformly across the entire surface. The reduced stress allows for ring actuators to be formed as thinner films, producing a larger stroke for the same applied voltage as a rectangular device [5.33].

The requirements for the main sealant valve are driven by the mass flow rate for nozzle operation while firing all eight nozzles, overestimated to be  $1 \cdot 10^{-3}$  kg/s.

The mass flow rate of the valve is dependent upon the fluid density and variable resistance [5.34],

$$\dot{m} = \varphi_v \rho \quad (5.14)$$

Where  $\varphi_v$  is the volumetric flow rate dependent on the pressure differential across the valve, static resistance, and variable resistance,

$$\varphi_v = \frac{\Delta P}{R_s + R_v} \quad (5.15)$$

Where  $\Delta P$  is the pressure differential from chamber to ambient,  $R_s$  is the static resistance of the flow channel, and  $R_v$  is the variable resistance of the orifice opening. This formulation of the problem allows for analysis of the actuator independent of the upstream flow channel. The variable resistance dictates how much fluid can flow through the valve by actuating the device. When the valve is closed, resistance is infinite; when the valve is fully opened, the variable resistance is at its lowest. When using a ring-type piezo actuator, the variable resistance can be calculated as

$$R_v = \frac{6\mu l n \left( \frac{a_2}{a_1} \right)}{\pi h^3} \quad (5.16)$$

Where  $\mu$  is the fluid dynamic viscosity (assumed to be chamber conditions),  $a_2$  is the outer ring radius,  $a_1$  is the inner ring radius, and  $h$  is the opening height, also known as the stroke of the actuator in its final configuration [5.34]. The final configuration takes into account expected stroke per the manufacturer's documentation and the stiffness of the flexible membrane [5.35]. A correction factor is applied to the manufacturer's stroke length,

$$\varepsilon = \frac{k_p}{k_p + k_m} \quad (5.17)$$

Where  $k_p$  is the piezoelectric stack's stiffness and  $k_m$  is the stiffness of the membrane. Thus, the actual stroke height can be found as the product of the stiffness factor  $\varepsilon$  and manufacturer's free stroke height  $h_f$ ,

$$h = \varepsilon h_f \quad (5.18)$$

From Equation 5.16, the values of inner and diameter are based on commercially available piezoelectric ring stacks. The stroke is dependent on the stack height and applied voltage. The higher the applied voltage (within the actuator's limit) and higher the stack, the higher the stroke. The inner and outer diameters have negligible influence on the linearity of stack extension. Large stroke and inner diameter reduce the variable resistance, meaning there is a larger area for fluid to pass through from inlet to outlet and will not be constricted as much.

The static resistance accounts for energy loss in the fluid flow channel leading to the inlet orifice. The static resistance should be minimized within the geometrical constraints of the valve. The static resistance is found through derivation of results by [5.36]

$$R_s = \left( \frac{128}{3\pi} - \frac{8\pi}{3} \right) \frac{\mu L}{(\pi r_c^2)^2} \quad (5.19)$$

Where  $L$  is the length of the channel and  $r_c$  is the channel's radius. A circular flow channel is approximated assuming results from MEMS wet manufacturing. From previous results, the flow channels will be 3 mm wide. It is assumed the orifice chip height is 500 microns thick. An available COTS piezo stack is used from *Noliac* for representative calculations [5.37]. This stack has inner diameter of 9 mm, outer diameter of 15 mm, and available stack heights from 4-150 mm.

| Parameter  | Value                      |
|------------|----------------------------|
| $\dot{m}$  | $9 \cdot 10^{-4}$ kg/s     |
| $\Delta P$ | 0.75 bar                   |
| $\mu$      | $1.325 \cdot 10^{-5}$ Pa-s |
| $a_1$      | 9 mm                       |
| $a_2$      | 15 mm                      |
| $L$        | 0.5 mm                     |
| $r_c$      | 1.5 mm                     |

Table 5.2: Main Valve Design Parameters

Knowing these parameters, the required stroke height can be calculated to produce at least the required flow rate.

$$\varepsilon h_f = \left( \frac{6\mu * \ln\left(\frac{a_2}{a_1}\right)}{\pi \left(\frac{\rho \Delta P}{\dot{m}} - R_s\right)} \right)^{1/3} \quad (5.20)$$

From Kirchoff plate theory, the bending stiffness of a thin membrane can be approximated as

$$k_m = \frac{E_{mem} t_{mem}^3}{12(1 - \nu_{mem}^2)} \quad (5.21)$$

Where  $E_{mem}$  is the membrane material's Young's modulus,  $t_{mem}$  is the membrane's thickness, and  $\nu_{mem}$  is the membrane's Poisson ratio. The piezo stack's stiffness is provided by the manufacturer. However, each stack provides lower stiffness with increased height. Thus, it is necessary to iterate through combinations of stroke height and stack stiffness to find the correct stack height.

After searching through combinations from PiezoDrive [5.35], it has been determined that the piezoelectric ring stack needs to have an inner radius of 9 mm, outer radius 15 mm, and stack height 38 mm.

The next step is to develop a fabrication process for the valve chip. One silicon chip is used to form the orifice wafer, and a PDMS flexible membrane is fabricated to serve as the flexible diaphragm. The piezo ring stack is then bonded to the PDMS, and the end cap is bonded to the piezo stack and middle of the PDMS.

Fabrication of the orifice layer begins by growing a thin oxide layer on both sides of the chip. This seals the chip from etching when submerged in the wet etchant. A photoresist layer is spun on the top side and developed to expose the inlet and outlet holes. The holes are then etched in an isotropic wet etching bath. Once completed, or until only a few microns remain, the same process is done to etch the seal rings.

The PDMS layer is fabricated by a casting process. A thick layer of photoresist is spun on a glass wafer to serve as the mold. The photoresist is then exposed and developed to create the

negative cast shape. PDMS is then mixed and spun over the mold and cured. The PDMS layer can be removed by dipping the wafer in an acetone bath to dissolve the photoresist [5.38]. The membrane layer is then epoxied to the orifice layer. Bond strength of typical epoxies easily exceeds the operating pressures of the microfluidic system, often requiring multiple bars of tension to delaminate the surfaces [5.39]. The piezo ring stack and end cap can likewise be bonded to the PDMS layer and each other to complete the valve chip.

## **6. Control Systems for Hopping, Attitude, and Up-Righting**

This chapter presents high level control systems for three separate mobility modes of AMIGO on the surface of an asteroid during nominal mission operations. The first mobility mode is determining the launch parameters of a quasi-ballistic hop to move an AMIGO from one location to another within some pre-determined maximum transit time. This allows for accurate surface hopping to various points of interest while avoiding obstacles. The second control mode is that of AMIGO in flight during its transit. The attitude control system must keep AMIGO upright and provide safe landing such that the robot is not damaged and is capable of performing science operations and subsequent hops. The final mobility mode is up-righting maneuvers. In case an AMIGO does not land upright and must be corrected, the lander must have the capability of correcting its orientation to continue its mission.

## 6.a: Hopping Algorithm

A simplified model of a robotic lander’s dynamics on the surface of an asteroid is used to demonstrate hop planning to some desire point of interest or for obstacle avoidance. The dynamic equations of motion of the robot in the asteroid’s body fixed coordinate system is expressed as:

$$\ddot{r} + 2\omega \times \dot{r} + \omega \times (\omega \times r) + \dot{\omega} \times r = g + d + u \quad (6.1)$$

Where,  $r$  is the position vector,  $\dot{r}$  is the velocity vector,  $\ddot{r}$  is the acceleration vector,  $\omega$  is the angular velocity vector of the asteroid,  $g$  is the gravitational acceleration,  $d$  is the disturbance acceleration such as solar radiation pressure (SRP) and third body perturbations, and  $u$  is the control acceleration from the thruster. For simplified first-order analysis, the asteroid is considered to have a fixed angular velocity, so  $\dot{\omega}$  is equal to zero. Although gravity in smaller bodies is much weaker than on Earth, it still is the dominant force on robots. Other perturbations do exist, including SRP, third body effects, non-rigid robot dynamics, and lumpy gravity fields. The polyhedral model is the most accurate gravity model for smaller irregular bodies which leverages the divergence theorem to exactly model the gravitational potential ( $U$ ), gravitational acceleration ( $g = \nabla U$ ), gradient ( $\nabla \nabla U$ ) and Laplacian ( $\nabla^2 U$ ) of a constant density polyhedron as a summation over all facets and edges of the surface mesh.

The goal is for the robot to hop from rest at position  $r_0$  with velocity  $v_0$  and impact at position  $r_f$  with velocity  $v_f$ . The problem of computing the launch velocity,  $v_0$ , to intercept a target location,  $r_f$ , at time  $\tau = t_f - t_0$  is the well-known “Lambert orbital boundary-value problem” and efficient numerical solutions for different types of gravity fields are available. For the case of asteroids with irregular gravity field, a simple shooting method is used to calculate the launch velocity to successfully impact a target location [6.1].

Figure 6.1 shows the trajectory of an example robot from its initial position to the final position on asteroid Itokawa. This asteroid was used due to the similar size and mass to Bennu with a high-fidelity shape model for simulation purposes. Two waypoints were added in between to reduce error in the final position. The robot is able to find the initial hopping velocities required to reach its target location from its initial location successfully visiting the waypoints in between. Close targets are able to efficiently be reached by just one hop, but longer excursions require less efficient multi-hop schemes.

The maximum hopping height and hopping distance AMIGO is capable of on different small solar system bodies is shown in Figure 6.2 and Table 6.1. For each body, the local gravity is assumed a point mass and a simple ballistic trajectory is computed assuming the mean mass and radius. Thrust is assumed to be all eight nozzles fired at once for a duration of 1 second, corresponding to a  $\Delta v$  of 0.048 m/s. As can be seen from the more massive bodies, the hops are quite small and can be increased by increasing the burn time of the propulsion system (opening the valves for longer durations).

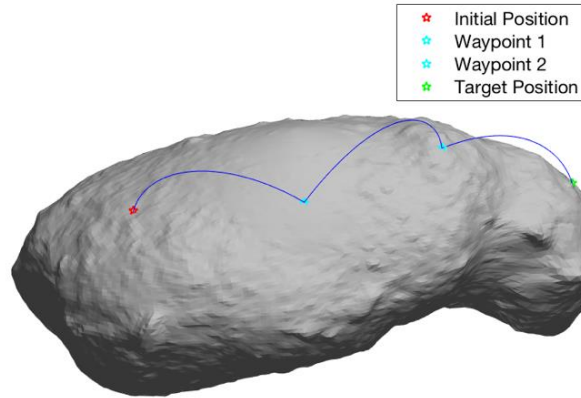


Figure 6.1: Ballistic Hopping Trajectories from an Initial Position to a Final Position with Two Waypoints In-between on Itokawa

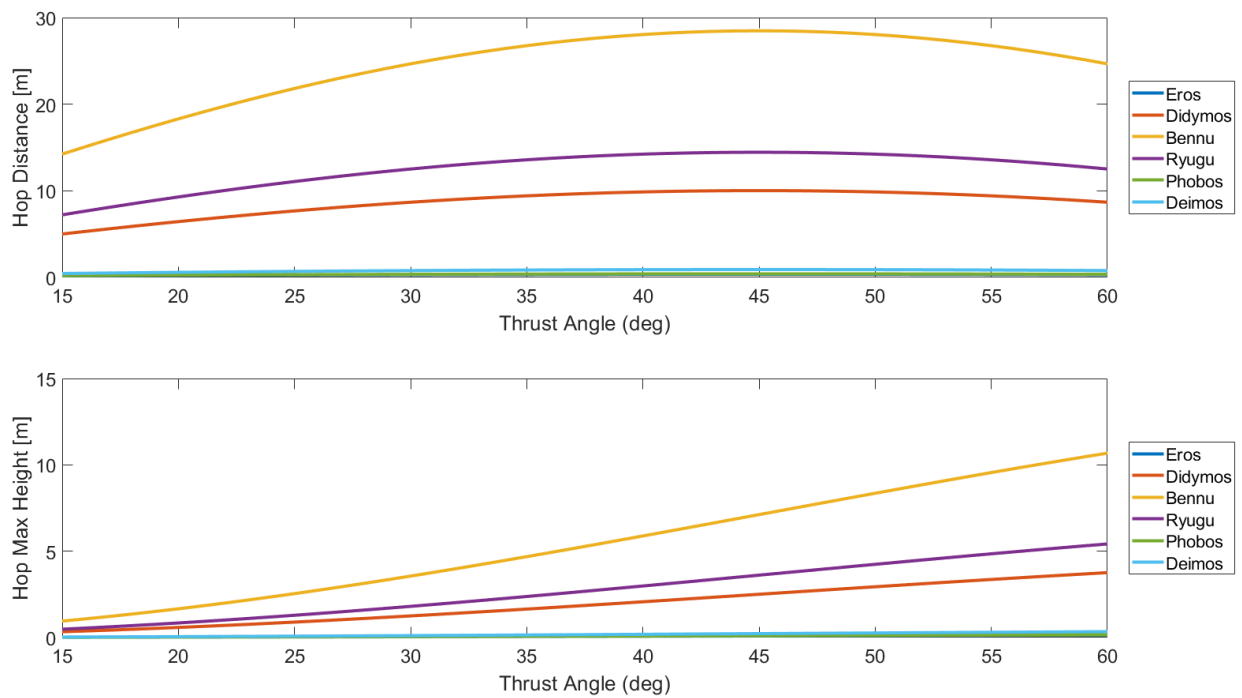


Figure 6.2: Maximum Hop Distance and Hop Height of AMIGO on Various SSSBs

| <b>Body</b> | <b>Max Distance [m]</b> | <b>Max Height [m]</b> |
|-------------|-------------------------|-----------------------|
| Eros        | 0.3686                  | 0.1382                |
| Didymos     | 10.02                   | 3.759                 |
| Bennu       | 28.48                   | 10.68                 |
| Ryugu       | 14.45                   | 5.419                 |
| Phobos      | 0.4141                  | 0.1553                |
| Deimos      | 0.9109                  | 0.3416                |

Table 6.1: Maximum Hop Distance and Height on Various SSSBs

## 6.b: Attitude Control During Hops

An attitude control system is required to ensure safe landing of the AMIGO after a hop. Quaternions are used as the attitude for the hopper. Quaternions are defined as

$$q = [q_1 \ q_2 \ q_3 \ q_4]^T \quad (6.2)$$

$$q = [q_v \ q_4]^T$$

Considering the equations of motion of a rigid spacecraft,

$$\dot{q}_v = \frac{1}{2} [\tilde{q}_v + I_{3 \times 3} q_4] \omega \quad (6.3)$$

$$\dot{q}_4 = -\frac{1}{2} q_v^T \omega \quad (6.4)$$

$$J \dot{\omega} = -\tilde{\omega} J \omega + \text{sat}(u) + L \quad (6.5)$$

Where  $\omega \in \mathbb{R}^3$  is the angular velocity vector,  $I_{3 \times 3}$  is the  $3 \times 3$  identity matrix, the  $\tilde{\cdot}$  is the skew symmetric operator,  $J \in \mathbb{R}^{3 \times 3}$  is the spacecraft inertia matrix,  $u \in \mathbb{R}^3$  is the control torque, the  $\text{sat}$  function corresponds to the saturation control modes, and  $L \in \mathbb{R}^3$  is the disturbance torque. Quaternions maintain structure through one constraint equation,

$$q_1^2 + q_2^2 + q_3^2 + q_4^2 = 1 \quad (6.6)$$

Meaning quaternions lie on a three-dimensional hypersphere in four-dimensional space,  $q \in \mathbb{S}^3$ . It is assumed that the attitude  $q$  and angular velocity  $\omega$  are known.

It is desired to design a control system to drive the spacecraft to the identity attitude ( $q_v = 0$ ) with no angular velocity ( $\omega = [0 \ 0 \ 0]^T$ ). To accomplish this, an adaptive sliding mode controller (ASMC) is used for its properties of robustness and disturbance rejection [6.2].

The saturated control authority is based on limitations from the thrusters; i.e. the discretized nozzles are only capable of providing certain amounts of torque on the robot. Considering the three saturation modes of minimum, medium, and maximum control torque, the saturation function is defined as

$$\text{sat}(u) = \begin{cases} 0, & \text{abs}(u_i) < u_{min} \\ u_{min}, & u_{min} \leq u_i < u_{mid} \\ u_{mid}, & u_{mid} \leq u_i < u_{max} \\ u_{max}, & u_{max} \leq u_i \end{cases} \quad (6.7)$$

Where  $u_i$  are the required control torque components in the robot body axes and  $\text{abs}(u_i)$  is the absolute value of the torque component. This saturation case is mirrored for negative torque, meaning rotation in the opposite direction. For the  $z$ -axis case, there is simply a maximum saturation, as the reaction wheel has continuous spin rates from no spin to its rated maximum. The input control torque must always satisfy these saturation conditions.

Drawing from the results from Zhu et. al [6.3], the control law is defined as

$$u = -\tau S - \sigma \text{sgn}(S) - u_a \quad (6.8)$$

Where  $\tau = \text{diag}(\tau_i), \tau_i > 0$  and  $\sigma = \text{diag}(\sigma_i), \sigma_i > 0$  are design parameters to reduce chattering upon reaching the sliding surface,  $S$  is the sliding surface ( $S \in \mathbb{R}^3$ )

$$S = \omega + k_1 q_v \quad (6.9)$$

With design scalar  $k_1 > 0$ ,  $\text{sgn}(S)$  is the sign function

$$\text{sgn}(S_i) = \begin{cases} -1, S_i < 0 \\ 1, S_i \geq 0 \end{cases} \quad (6.10)$$

And adaptive controller  $u_a$

$$u_a = \beta k_2 k_3 \|\xi\| \frac{\|S\|}{S} \quad (6.11)$$

$$\xi = [q_v \ \omega \ 1] \quad (6.12)$$

The update control laws are functions of time,

$$\dot{k}_2 = \beta k_2^3 k_3 \|\xi\| \|S\|, k_2(0) > 0 \quad (6.13)$$

$$\dot{k}_3 = p \|\xi\| \|S\|, k_3(0) > 0 \quad (6.14)$$

With  $\beta > 1$  and  $p > 0$  are design parameters. The adaptive portion of the control law rejects inertia uncertainties and external disturbances. From [6.3], it is shown that the control law Equation (6.8) is asymptotically stable for some bounded model uncertainties and disturbance torques. In actuality, due to the discontinuous nature of the control actuator, the controllable subspace may not be driven to  $S = 0$ . Rather, the robot will likely chatter around the desired state. The use of the ‘‘boundary layer’’ approach in [6.3] is neglected due to the lack of fine pointing control offered by the thrusters; no chattering can be reduced due to the minimum impulse bit.

To properly assess the usefulness of the sliding mode controller, expected disturbances should be modeled and accounted for in their worst case perturbations on the robot. The most important perturbing forces for the robotic hopper are solar radiation pressure (SRP) and gravity effects, namely oblateness and ellipticity [6.4]. Formulating the solar radiation pressure in terms of a potential function,

$$R_{SRP} = \frac{-\beta}{d_{ast}^2} \hat{d}_{ast} \cdot \hat{r} \quad (6.15)$$

Where  $\hat{d}_{ast}$  is the vector from the sun to the asteroid,  $\hat{r}$  is the vector of the orbiter from the asteroid center of mass in the asteroid reference frame, and  $\beta$  is quantified as

$$\beta = (1 + \rho) \cdot \left(\frac{A}{m}\right) P_\phi \quad (6.16)$$

Where  $\rho$  is the albedo of the spacecraft,  $A$  is the cross-sectional area,  $m$  is the mass, and  $P_\phi$  is the solar radiation constant. The asteroid gravitational effects are captured in the oblateness  $C_{20}$  and ellipticity  $C_{22}$  coefficients in a 2<sup>nd</sup> degree gravity perturbation,

$$R_m = \frac{-\mu}{2r^3} C_{20} [1 - 3(\hat{r} \cdot \hat{p})^2] + \frac{3\mu}{r^3} C_{22} [(\hat{r} \cdot \hat{s})^2 - (\hat{r} \cdot \hat{q})^2] \quad (6.17)$$

Where  $\mu$  is the gravitational parameter of the asteroid,  $\hat{p}$  is the maximum principal inertia axis,  $\hat{q}$  is the intermediate principal inertia axis, and  $\hat{s}$  is the minor principal inertia axis of the asteroid. Higher order effects are ignored. In an inertially fixed reference frame with the origin at the center of mass of the asteroid, the equations of motion of a satellite in orbit about an asteroid can be defined as

$$\ddot{\vec{r}} = \frac{\partial U}{\partial \vec{r}} + \frac{\partial R_{SRP}}{\partial \vec{r}} + \frac{\partial R_m}{\partial \vec{r}} \quad (6.18)$$

Where the potential U is

$$U = \frac{\mu}{r} \quad (6.19)$$

The disturbing accelerations modify the Keplerian motion, as seen in Equation (6.18). To compute the non-averaged disturbing accelerations,

$$\vec{a}_d = \vec{a}_{d_{SRP}} + \vec{a}_{d_m} = \frac{\partial R_{SRP}}{\partial \vec{r}} + \frac{\partial R_m}{\partial \vec{r}} \quad (6.20)$$

Considering the SRP perturbations, the disturbing acceleration calculation is simple,

$$\vec{a}_{d_{SRP}} = \frac{-\beta}{d_{ast}^3} \hat{d}_{ast} \quad (6.21)$$

To formulate the mass distribution acceleration, the disturbance is split into the oblateness and ellipticity effects for easier derivation.

$$\vec{a}_{d_{20}} = \frac{\partial}{\partial \vec{r}} \frac{-\mu}{2r^3} C_{20} [1 - 3(\hat{r} \cdot \hat{p})^2] \quad (6.22)$$

$$\vec{a}_{d_{20}} = \frac{-\mu}{2} C_{20} [1 - 3(\hat{r} \cdot \hat{p})^2] \frac{\partial}{\partial \vec{r}} \frac{1}{r^3} + \frac{3\mu}{2r^3} C_{20} \frac{\partial}{\partial \vec{r}} (\hat{r} \cdot \hat{p})^2 \quad (6.23)$$

Now, considering the partial derivative terms individually,

$$\frac{\partial}{\partial \vec{r}} \frac{1}{r^3} = -3r^{-4} \frac{\partial r}{\partial \vec{r}} \quad (6.24)$$

$$\frac{\partial r}{\partial \vec{r}} = \frac{\partial \sqrt{\vec{r} \cdot \vec{r}}}{\partial \vec{r}} = \hat{r} \quad (6.25)$$

The other partial term in Equation 6.23 is calculated,

$$\frac{\partial}{\partial \vec{r}} (\hat{r} \cdot \hat{p})^2 = 2(\hat{r} \cdot \hat{p}) \frac{1}{r} \frac{\partial}{\partial \vec{r}} (\hat{r} \cdot \hat{p}) = \frac{2}{r} (\hat{r} \cdot \hat{p}) \hat{p} \quad (6.26)$$

Thus, the disturbing acceleration from oblateness is

$$\vec{a}_{d_{20}} = \frac{-3\mu}{2r^4} C_{20} ([1 - 3(\hat{r} \cdot \hat{p})^2] \hat{r} - 2[\hat{r} \cdot \hat{p}] \hat{p}) \quad (6.27)$$

Now, for the computation of the ellipticity disturbing acceleration,

$$\vec{a}_{d_{22}} = 3\mu C_{22}[(\hat{r} \cdot \hat{s})^2 - (\hat{r} \cdot \hat{q})^2] \frac{\partial}{\partial \vec{r}} \frac{1}{r^3} + \frac{3\mu}{r^3} C_{22} \frac{\partial}{\partial \vec{r}} [(\hat{r} \cdot \hat{s})^2 - (\hat{r} \cdot \hat{q})^2] \quad (6.28)$$

Noting results from Equations 6.24-6.26,

$$\vec{a}_{d_{22}} = \frac{3\mu}{r^4} C_{22} (3[(\hat{r} \cdot \hat{s})^2 - (\hat{r} \cdot \hat{q})^2] \hat{r} + 2(\hat{r} \cdot \hat{s}) \hat{s} - 2(\hat{r} \cdot \hat{q}) \hat{q}) \quad (6.29)$$

Combining the three disturbing accelerations from Equations 6.21, 6.27 and 6.29,

$$\vec{a}_{d_m} = \frac{3\mu}{r^4} [C_{20}([1 - 3(\hat{r} \cdot \hat{p})^2] \hat{r} - 2[\hat{r} \cdot \hat{p}] \hat{p}) + C_{22}(3[(\hat{r} \cdot \hat{s})^2 - (\hat{r} \cdot \hat{q})^2] \hat{r} + 2(\hat{r} \cdot \hat{s}) \hat{s} - 2(\hat{r} \cdot \hat{q}) \hat{q})] \quad (6.30)$$

The SRP and mass distribution disturbing accelerations are used in Cowell's formulation to describe the equations of motion. These are numerically integrated to simulate a short period motion about an asteroid. Motion about asteroid 101955 Bennu is considered. Table 6.2 represents required asteroid and satellite parameters [6.5]

| Parameter                     | Value  |
|-------------------------------|--|
| Oblateness $C_{20}$           | -0.0175 km <sup>2</sup>  |
| Ellipticity $C_{22}$          | 0.0058 km <sup>2</sup>   |
| Gravitational Parameter $\mu$ | 5*10 <sup>-4</sup> km <sup>3</sup> /s <sup>2</sup>               |
| Mass to Area Ratio m/A        | 20 kg/m <sup>2</sup>   |
| Albedo                        | 0.05   |
| Solar Radiation $P_\phi$      | 1*10 <sup>8</sup> km <sup>2</sup> /s <sup>2</sup> m <sup>2</sup> |
| Asteroid vector               | [1.12 0 0] AU  |

Table 6.2: Asteroid and Spacecraft Parameters

The asteroid's inertia axes are chosen to be parallel to the x, y, and z axes of the asteroid's orbit for simplification (asteroid rotation is not taken into account due to the large rotational period relative to a hop). During simulations, the force is taken to be acting over the cross-sectional area of the robot evenly. Then, the net torque applied is calculated and included as the disturbing torque.

A disturbance also arises from the non-rigid nature of the inflatable structure. The inflatable can deform and produce some inertia uncertainties. A non-linear finite element model was set up using Tsai-Belytschko membrane elements to capture the membrane's deformation behavior. A worst analysis was conducted to simulate the membrane colliding elastically with a rigid wall at an incoming velocity of 1 m/s. This is assumed based on potential landing velocities after separation points from the mother spacecraft [6.6]. A constant volume inflation was used. The assumption this model makes is that the membrane is fully inflated at the time of collision.

Figure 6.3 shows the worst case expected deformation and stress plots of the membrane when it lands directly on the inflatable's side. As can be observed in this case a total deformation of about 60mm is expected to take place in the longitudinal direction. The corresponding worst-case change in inertia is accounted for in inertia uncertainties for numerical simulation.

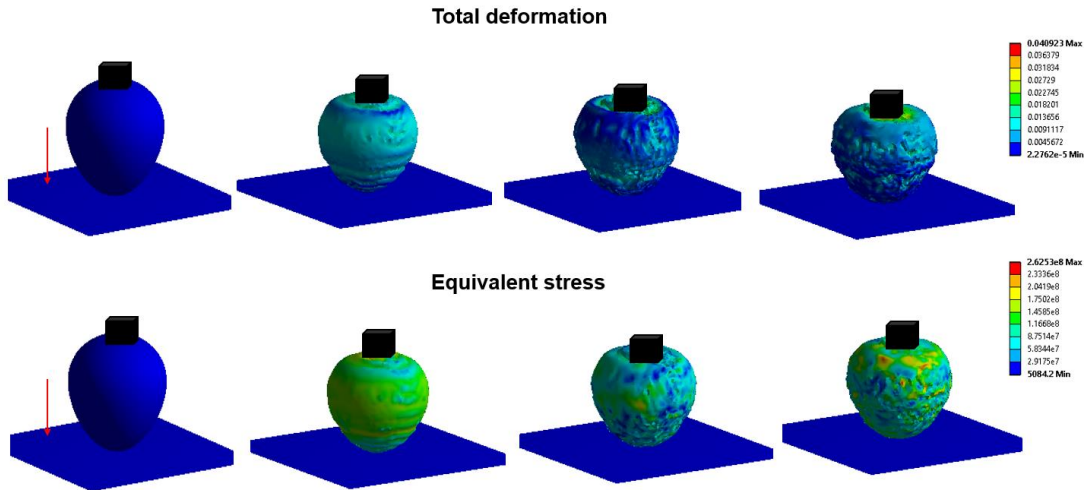


Figure 6.3: Deformation and Stress Plots

From the equivalent stress plots, it can be observed that stress concentrations begin to cause local buckling at the interface between the 1U CubeSat and the membrane causing to CubeSat to move into it. Table 6.3 describes analysis settings used:

| Property                         | Value   |
|----------------------------------|---|
| Membrane Young's modulus (Mylar) | 760000 psi  |
| Membrane Poisson's ratio (Mylar) | 0.38  |
| Membrane thickness               | $1.27 \times 10^{-5}$ m   |
| Internal membrane pressure       | $2 \times 10^{-5}$ psi (similar to that expected by sublimates) |
| Initial membrane velocity        | 1 m/s   |

Table 6.3: Deformation Simulation Properties

To begin numerical simulations, the initial state of the system is defined for a variety of cases. A 4<sup>th</sup> Order Runge-Kutta method is used to account for the non-linearity of quaternion rotation; they cannot be simply added together. MATLAB is used for simulations. Outputs of the simulation are plots of the quaternion and angular velocity evolution in time (Figure 6.4 and 6.5).

From these simulations of the controllability of the attitude, the average propellant consumption during one hop is  $7.52 \pm 0.78$  milligrams of propellant, whereas the actuation for one hop consumes 0.1 milligrams. As a high estimate, 8.5 milligrams of propellant is needed to actuate and control a single hop. Assuming a useful mass efficiency of 85%, 10 grams of propellant will enable 10 fully controlled hops. Increasing the amount of hops desired will require more mass of propellant and mass of the storage tank and heating system.

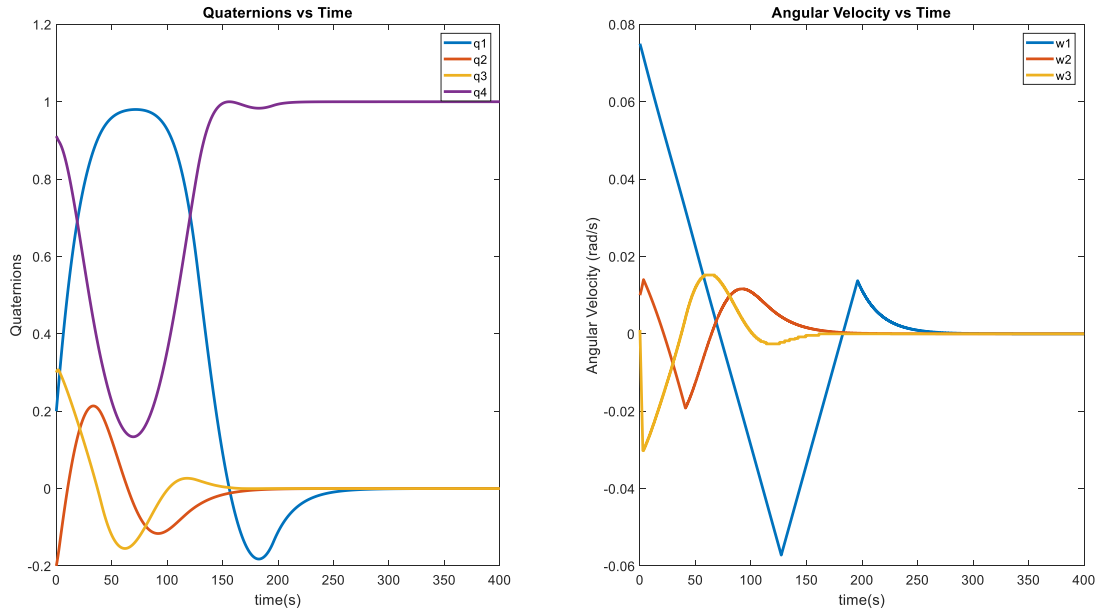


Figure 6.4:  $q(0) = [0.2 \ -0.2 \ 0.3 \ 0.911]^T$ ,  $\omega(0) = [0.075 \ 0.01 \ 0.001]^T \text{rad/s}$ .

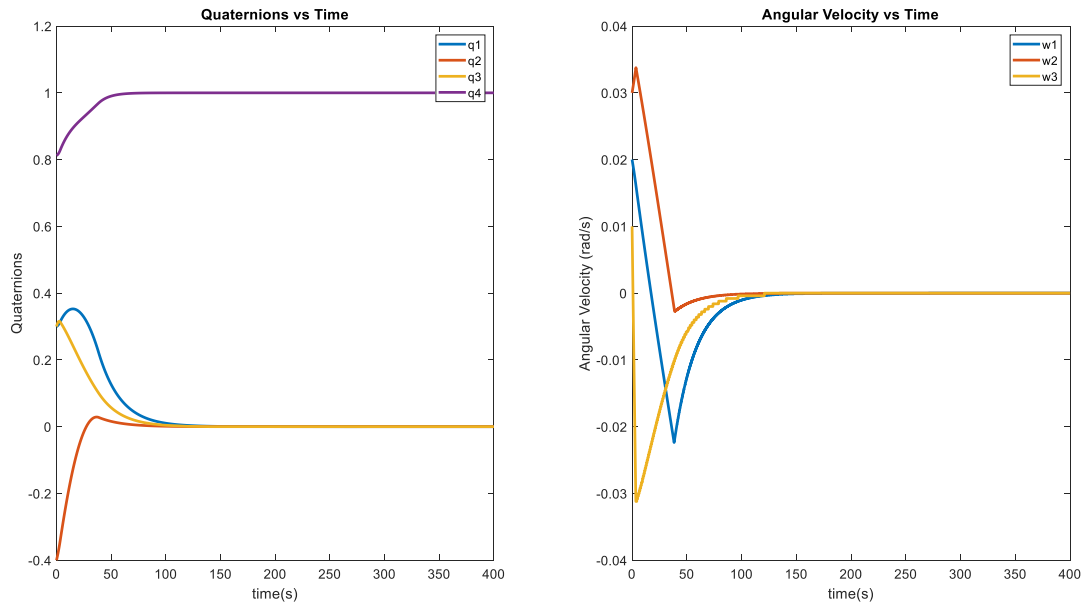


Figure 6.5:  $q(0) = [0.3 \ -0.4 \ 0.3 \ 0.812]^T$ ,  $\omega(0) = [0.02 \ 0.02 \ 0.01]^T \text{rad/s}$ .

### 6.c: Up-Righting Maneuvers

Should the robot not land upright, it will tilt over onto its side and rest on the surface with contact points on the inflatable surface and on the corner of the main structural cube. When this happens, the thruster chip is used to induce sliding motion against the regolith and liftoff of the robot. Assumptions made are that the regolith is homogeneous and flat (not rubble piles) and the contacts are points. A simplification to the model is planar motion, illustrated in Figure 6.6.

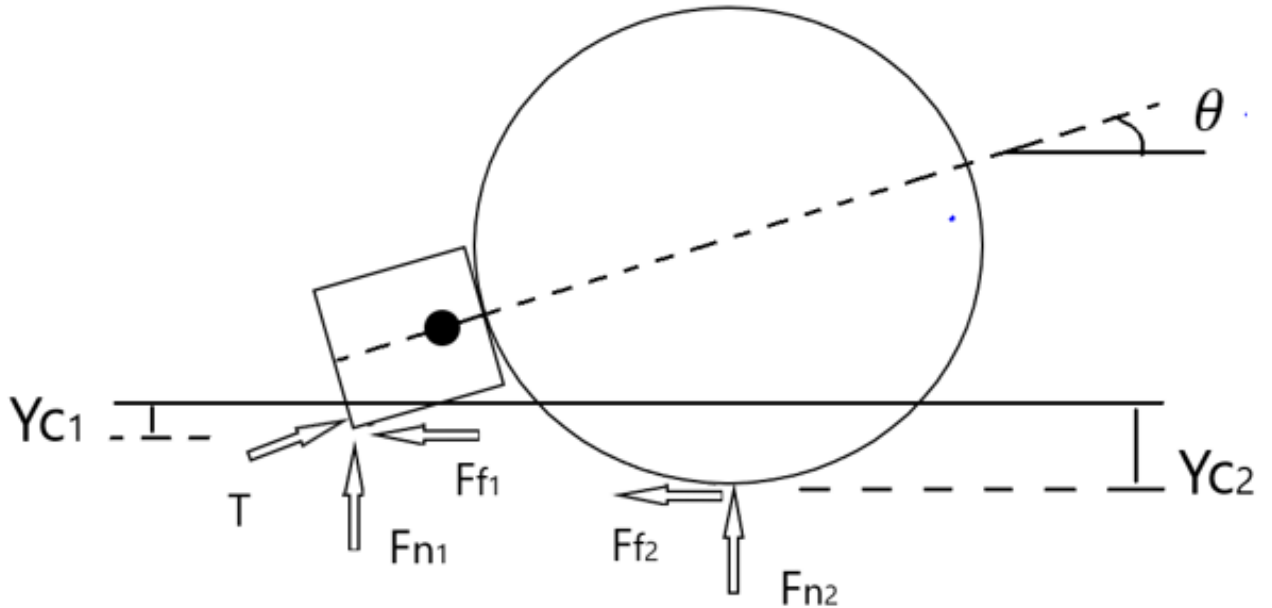


Figure 6.6: Tipped Over AMIGO with Reaction Forces

Drawing on knowledge from developments in the Hedgehog program [6.7], the system is modelled through Lagrangian mechanics [6.8]. The state of the planar robot is defined through generalized coordinates  $g = (x, y, \theta)$ . The motion of the robot is described by Eqn. 6.1

$$\frac{d}{dt} \frac{\partial T}{\partial \dot{g}} - \frac{\partial T}{\partial g} + \frac{\partial D}{\partial \dot{g}} + \frac{\partial V}{\partial g} = \frac{\partial \delta L}{\partial \delta g} \quad (6.31)$$

Where  $T$  is the kinetic energy,  $D$  is dissipative energy,  $V$  is potential energy, and  $\delta L$  is the Lagrangian portion of the virtual work. These quantities can be defined through state  $g$  and the two contact points,  $(x_{c_1}, y_{c_1})$  for the contact of the corner and  $(x_{c_2}, y_{c_2})$  for the inflatable contact point, both treated as points and assuming small impact depth:

$$T = \frac{1}{2} m(\dot{x}^2 + \dot{y}^2) + \frac{1}{2} J_x \dot{\theta}^2 \quad (6.32)$$

$$V = m g_{ast} y + V_c \quad (6.33)$$

Where  $m$  is the mass of the robot (assuming negligible mass change through propellant loss),  $J_x$  is the polar moment of inertia,  $g_{ast}$  is local surface gravity, and  $V_c$  is the contact potential energy,

$$V_c = \frac{1}{2}K(y_{c_1}^2 + y_{c_2}^2) \quad (6.34)$$

Where  $K$  is the stiffness of the regolith. This term only is used when the point is actually in contact with regolith ( $y_{ci} < 0$ ). The dissipative term is defined as

$$D = \frac{1}{2}C(\dot{y}_{c_1}^2 + \dot{y}_{c_2}^2) \quad (6.35)$$

Where  $C$  is the damping coefficient of the regolith, and only considers  $\dot{y}_{c_i} < 0$  (penetrating into the regolith). The virtual work is

$$L = u\theta + L_c \quad (6.36)$$

Where  $u$  is the control torque from the thrusters firing and  $L_c$  is the work against friction,

$$L_c = F_{f_1}x_{c_1} + F_{f_2}x_{c_2} \quad (6.37)$$

With slipping friction

$$F_{f_i} = -\text{sign}(\dot{x}_{c_i})\mu_d F_{n_i} \quad (6.38)$$

Where  $\mu_d$  is the dynamic friction coefficient and  $F_{n_i}$  is the normal force at the contact point. The contact points are geometrically related to the center of mass and rotation angle  $\theta$  when treated as a rigid body,

$$x_{c_1} = x - r_{c_1} \cos(\theta) \quad (6.39)$$

$$y_{c_1} = y - r_{c_1} \sin(\theta) \quad (6.40)$$

$$x_{c_2} = x + r_{c_2} \cos(\theta) \quad (6.41)$$

$$y_{c_2} = y - r_{c_2} \sin(\theta) \quad (6.42)$$

Where  $r_{c_1}$  is the distance from the center of mass to the corner of the main structure, and  $r_{c_2}$  is the distance from the center of mass to the contact point on the inflatable. From Equation 6.31, the contact dynamics can be described

$$m\ddot{x} = -F_{f_1} - F_{f_2} + T\cos(\theta) \quad (6.43)$$

$$m\ddot{y} + mg_{ast} + K[(y - r_{c_1} \sin(\theta)) + (y - r_{c_2} \sin(\theta))] + C[(\dot{y} - \dot{\theta}r_{c_1} \cos(\theta)) + (\dot{y} - \dot{\theta}r_{c_2} \cos(\theta))] = T\sin(\theta) \quad (6.44)$$

$$J_x\ddot{\theta} + r_{c_1} \sin(\theta) [K(y - r_{c_1} \sin(\theta)) + C(\dot{y} - \dot{\theta}r_{c_1} \cos(\theta))] + r_{c_2} \sin(\theta) [K(y - r_{c_2} \sin(\theta)) + C(\dot{y} - \dot{\theta}r_{c_2} \cos(\theta))] = u \quad (6.45)$$

The goal of the up-righting control is to drive the robot upright ( $\theta = \frac{\pi}{2}$ ) with the bottom of the robot resting on the surface ( $y =$  the distance from the center of gravity to the bottom of the robot). The adaptive sliding mode control law Equation 6.9 is modified,

$$S = \left[ x, y_{c_1}, \theta - \frac{\pi}{2} \right]^T \quad (6.46)$$

$$\xi = [\dot{x} \ \dot{y} \ \dot{\theta}] \quad (6.47)$$

Euler's equation of motion for the planar case is used.

$$J_x = -J_x \omega^2 + u + L_{cont} \quad (6.48)$$

Where  $L_{cont}$  are the torques from contact forces.

## **7. Conclusion**

The main purpose of this thesis is to provide the development in two enabling technologies for asteroid surface hopping robots through some hopping mechanism and a visualization method for path planning. The path planning provide a method to navigate an asteroid's hazardous terrain for safe excursions to a robust sampling of science data. The hopping mechanism is propulsive based, utilizing sublimate regenerative cold gas to lift the robot from the asteroid surface and provide attitude control during its traverses. This section provides the major conclusions and recommendations for future work of the thesis.

## 7.a: Summary of Findings

The development of the engineering test model of *AMIGO* shows the successful employment of a segmentation method to determine hop path planning. A top mounted stereo camera outputs a depth map and an algorithm has been developed to use that depth map to determine valid hopping directions and distances based on object detection. By analyzing vertical slices for obstructions in multiple ranges from a simple 2D color distance map, a large enough string of clear slices can be found through which to hop. Multiple hops can be completed autonomously to explore as much area of the surface as possible.

An optimization code for micronozzle has been developed that accounts for microfluidic loss effects. The optimization code was compared to a CFD analysis in ANSYS Fluent and shown to be of comparable performance. These nozzles produce milli-Newton levels of thrust with a specific impulse of over 60 seconds. Thus, they more than meet the requirement for achieving multiple hops while fitting within mass and volume restrictions.

The designed micropropulsion system works well as a control actuator for both hopping on an asteroid's surface and as attitude control during those hops. This is shown as the attitude settles to some desired attitude and angular velocity well within the bounds of the time it takes for the robot to hop, usually only requiring 30 seconds compared to 5-20 minutes of hopping.

## **7.b: Innovations**

The first significant advancement made is in the development of the visualization and path planning of hopping robots. From either a depth map or 3D point cloud, a scene can be analyzed by examining portions of the surrounding. Each of these slices is checked for obstructions and then compared as a whole. If a string of these slices is large enough for the robot to hop through, then it is a potential spot for the robot to traverse through. This can be extended to 3D point clouds, provided measures are in place that the robot does not hop backwards to where it originally was.

The other major contribution has been in the development of a novel sublimant regenerative cold gas micropropulsion system that doubles as both a hopping mechanism and 2-axis attitude control actuator. The propulsion system has low operating pressure and utilizes safe chemicals. The system is well suited for CubeSats in a university environment without need for as extensive safety testing and hazard avoidance as other chemical systems.

The micronozzles are designed with corrections applied to isentropic analysis. In this way, a large number of nozzles can be analyzed without need for computationally expensive fluid models to predict losses. The supposed optimum nozzles are then analyzed in CFD to verify performance and potentially make changes. In this way, nozzles can be examined much more rapidly.

The control of these nozzles is done by two sets of piezoelectric valves; high sealing forces are obtained by a diaphragm design, whereas each nozzle can be individually actuated with a cantilever type actuator. These two valves are designed with integration into a micro-system in mind to reduce the mass and volume occupied.

The control of these hopping robots through three mobility modes is realized by the micropropulsion system and a reaction wheel for the third axis. The use of the micronozzles as an attitude control actuator is proven through applying an adaptive sliding mode controller that utilizes three saturation modes. It is shown that this system enables attitude control well within the hop time constraints on small solar system bodies. The propulsion system is well suited to picosatellites and femtosatellites, classes of satellite systems that have not seen advances made in the realm of mobility. All of these systems combined contribute to the advancement of asteroid surface hopping capabilities for small robots.

### **7.c: Limitations**

The major limitations of the propulsion system lie in its operating pressures and output thrust. The chamber pressure almost necessitates vacuum operating conditions to reach the critical pressure ratio for supersonic exit. The low output thrust limits its use at best to attitude control for Earth orbit spacecraft, which would be in competition with more efficient macro systems; otherwise, this system is suited for CubeSat attitude control or for navigating in micro-gravity environments.

The analysis of fluid flow itself has limitations to a specific regime of low Reynold's number flow. The Knudsen number is sufficiently small that there is no need to account for rarefied or free molecular effects so a good portion of isentropic analysis can be utilized. However, there must be accounting for the viscous losses which at present is done only on experimental results for viscous losses in the thrust coefficient and on the discharge coefficient for mass flow rate. Those tests were done on nozzles of similar size to the ones analyzed in this work, but it is not confirmed they translate to nozzles of smaller orders of magnitude or larger.

The visualization system currently relies on stereo imaging that outputs image pictures and a 2D depth map. The development of our own stereo camera and image processing algorithm would allow for a point cloud to be recovered. However, the system as it stands does not provide topology information. The surface of asteroids not only has many boulders and obstructions but slopes and hills. Thus, the stereo system cannot distinguish between a sufficiently distant slope drop-off point and a lack of any surface at all. Future visualization systems will need to provide topology information so the robot is able to actually land where it expects.

## 7.d: Future Work

The future work for the development of the AMIGO platform primarily lies in testing and evaluation of the micropropulsion system. As of yet, no portions of the system have been fabricated as there is a lack of facilities to assess performance nor have the storage tank and filter been developed. Still, the valves and thruster chip can be tested with tradition pressurized cold gas to obtain an estimate of real performance. It is desired to validate nozzle designs before other components are fabricated in case the valve sizing needs to change to account for incorrect mass flow rates.

The propulsion system testing relies on development of a milli-Newton thruster test stand. Traditional measurements are done on load cells which are well suited to high thrust-to-weight ratio systems but are inaccurate for this system. The test stand in development is a torsional-type test stand, in which a beam pivots about a damped torsional spring when the thruster fires.

The deflection is measured by an LVDT, which measures the voltage of a solenoid when a metal pin in contact with the beam moves through the solenoid. The deflection is compared to a calibrated relation by which a range of known forces is applied to the beam each time a test is to be conducted in a thermal vacuum chamber. The state of development of this test stand is the CAD structure has been designed and a sensor selected. Still to be developed is a calibration scheme, leveling system, mounting/ transport system, and selection of torsional springs.

To actually test the nozzles, fabrication methods outlined in *Section 4.f* will be tested for compliance to mechanical design and actual performance. This ensures that both the nozzle is fabricated according to specification and the surface quality does not significantly inhibit performance.

Two other components must still be developed in the propulsion system. A filter will be used to filter out particulates from the gas flow before they reach the main sealant valve. This is an important component to reduce two-phase flow loss effects and prevent clogging of flow channels and valves. The heated storage tank must also be developed to house the solid propellant. This includes geometry design to fit within AMIGO, insulation for more efficient heating, and the resistive heating system. Ideally, there would be some sort of spring like mechanism to ensure the top surface of the sublimate is always in contact with the heaters so the primary heating method would be conductive rather than convective. Otherwise, the system would rely on heating the gas which would in turn heat the propellant base.

Developments still remain in the visualization system. Currently, the system uses a stereo camera as they are relatively small and can easily fit within CubeSat constraints. Progress is being made in miniaturizing LiDAR systems that would provide full 3D point cloud and mapping capabilities. Thus, the entire environment around the robot could be analyzed for a safe path to hop through. The algorithm is easily adapted to a 3D view and does not require a stereo input. A drawback to moving to LiDAR would be a loss of color image as the output would be a pure point cloud.

## II. References

- [2.1] “Vision and Voyages for Planetary Science in the Decade 2013-2022.” NASA, NASA, 18 Jan. 2018, [solarsystem.nasa.gov/science-goals/about/](http://solarsystem.nasa.gov/science-goals/about/).
- [2.2] Bernatowicz, T.J., Croat, T.K., and Daulton, T.L. “Origin and Evolution of Carbonaceous Presolar Grains in Stellar Environments.” 2006, Pp. 109-126 in *Meteorites and the Early Solar System II* (D.S. Lauretta and H.Y. McSween, eds.). University of Arizona Press, Tucson, Ariz.
- [2.3] Yang, J., Goldstein, J.F., and Scott, E.R.D. “Iron Meteorite Evidence for Early Catastrophic Disruption of Protoplanets”. 2007, *Nature* 446:888-891.
- [2.4] Gomes, R., et al. “Origin of the Cataclysmic Late Heavy Bombardment Period of the Terrestrial Planets.” *Nature*, vol. 435, no. 7041, 2005, pp. 466–469., doi:10.1038/nature03676.
- [2.5] Geers, V.C., et al. “C2D Spitzer-IRS spectra of disks around T Tauri stars. II. PAH emission features.” 2006, *Astronomy and Astrophysics* 459:545-556.
- [2.6] Castillo-Rogez, J. C., et al. “Expected Science Return of Spatially-Extended in-Situ Exploration at Small Solar System Bodies.” 2012 IEEE Aerospace Conference, 2012, doi:10.1109/aero.2012.6187034.
- [2.7] Grimm, Robert E., and Harry Y. Mcsween. “Heliocentric Zoning of the Asteroid Belt by Aluminum-26 Heating.” *Science*, vol. 259, no. 5095, 1993, pp. 653–655., doi:10.1126/science.259.5095.653.
- [2.8] David, Leonard (7 October 2013). "Russian Fireball Explosion Shows Meteor Risk Greater Than Thought". [www.space.com](http://www.space.com). New York, NY USA: Wired Magazine/Conde Nast.best estimate of the equivalent nuclear blast yield of the Chelyabinsk explosion
- [2.9] Hurford, T. A., et al. “Tidal Disruption of Phobos as the Cause of Surface Fractures.” *Journal of Geophysical Research: Planets*, vol. 121, no. 6, 2016, pp. 1054–1065., doi:10.1002/2015je004943.
- [2.10] Wilson, Jim. “What Is NASA's Asteroid Redirect Mission?” NASA, NASA, 16 Apr. 2015, [www.nasa.gov/content/what-is-nasa-s-asteroid-redirect-mission](http://www.nasa.gov/content/what-is-nasa-s-asteroid-redirect-mission).
- [2.11] Jones, Ross. “The MUSES-CN rover and asteroid exploration mission.” In *22nd International Symposium on Space Technology and Science*, pages 2403-2410, 2000.
- [2.12] Allen, Ross, et al. “Internally-Actuated Rovers for All-Access Surface Mobility: Theory and Experimentation,” *IEEE Conference on Robotics and Automation (ICRA)*, St. Paul, Minnesota, 2012.
- [2.13] Hockman, BJ, et al. “Design, Control, and Experimentation of Internally-Actuated Rovers for the Exploration of Low-Gravity Planetary Bodies,” *Conference on Field and Service Robotics*, 2015.
- [2.14] Xu, Yangsheng, et al. “Analysis of Actuation and Dynamic Balancing for a Single Wheel Robot” *IEEE/RSJ International Conference on Intelligent Robots and Systems*, October 1998.
- [2.15] Yoshimitsu, Tetsuo, et al. “Advanced Robotic System of Hopping Rovers for Small Solar System Bodies.” *International Symposium on Artificial Intelligence, Robotics, and Automation in Space*. 2012.
- [2.16] Jaumann, R, et al. “A Mobile Asteroid Surface Scout (MASCOT) for the Hayabusa-II Mission to Ryugu.” *European Planetary Science Congress*. 2017.
- [2.17] Dupius, Erick, et al. “Hopping robot for planetary exploration” *8th iSAIRAS*, September 2005.

- [2.18] Dubowsky, Steven, et al. "A concept Mission: Microbots for Large-Scale Planetary Surface and Subsurface Exploration" *Space Technology and Applications International Forum*, 2005.
- [2.19] Kalita, Himangshu, et al. "Mobility and Science Operations on an Asteroid Using a Hopping Small Spacecrafts on Stilts" 42<sup>nd</sup> AAS GNC Conference, February, 2018, Breckenridge, CO.
- [2.20] McMahon, Jay. "Dismantling Rubble Pile Asteroids with AoES (Area-of-Effect Soft-bots)." NIAC Proposal. 2017.
- [2.21] Lauretta, D. S., et al. "Episodes of Particle Ejection from the Surface of the Active Asteroid (101955) Bennu." *Science*, vol. 366, no. 6470, 2019, doi:10.1126/science.aay3544.
- [2.22] Thangavelautham, Jekan, et al. "Flying, hopping Pit-Bots for cave and lava tube exploration on the Moon and Mars" 2<sup>nd</sup> International Workshop on Instrumentation for Planetary Missions, NASA Goddard, Greenbelt, Maryland, 2014.
- [2.23] Kalita, Himangshu, et al. "GNC of the SphereX Robot for Extreme Environment Exploration on Mars," *Advances in the Astronautical Science*, February 2017.
- [2.24] Kalita, Himangshu, et al. "Guidance, Navigation and Control of Multirobot Systems in Cooperative Cliff Climbing," *Advances in the Astronautical Science*, February 2017.
- [2.25] Raura, Laksh, et al. "Spherical Planetary Robot for Rugged Terrain Traversal," *IEEE Aerospace Conference*, 2017.
- [3.1] Puig-Suari J., Turner C., Ahlgren W. "Development of the Standard CubeSat Deployer and a CubeSat Class Picosatellite." 2001 IEEE Aerosp. Conf. Proc. (Cat. No.01TH8542), vol. 1 (2001), pp. 347-353
- [3.2] Woellert, Kirk, et. al, "Cubesats: Cost-effective science and technology platforms for emerging and developing nations," *Advances in Space Research*, Volume 47, Issue 4, 2011, Pages 663-684, ISSN 0273-1177, <https://doi.org/10.1016/j.asr.2010.10.009>.
- [3.3] Staehle, Robert L., et al. "Interplanetary CubeSats: Opening the Solar System to a Broad Community at Lower Cost." (2012).
- [3.4] Schoolcraft J., Klesh A., Werne T. "MarCO?: Interplanetary Mission Development on a CubeSat." *AIAA SpaceOps Conference* (2016), pp. 1-8
- [3.5] Stirone, Shannon. "LightSail 2 Unfurls, Next Step Toward Space Travel by Solar Sail." *The New York Times*, *The New York Times*, 23 July 2019, [www.nytimes.com/2019/07/23/science/lightsail-solar-sail.html](http://www.nytimes.com/2019/07/23/science/lightsail-solar-sail.html).
- [3.6] Thangavelautham, J., Asphaug, E., Schwartz, S., "An On-Orbit CubeSat Centrifuge for Asteroid Science and Exploration," *IEEE Aerospace Conference* 2019.
- [3.7] Perez, F., "DustCube, a Nanosatellite Mission to Binary Asteroid 65803 Didymos as Part of the ESA AIM Mission." *Advances in Space Research*, Volume 62, Issue 12, 2018, Pages 3335-3356, ISSN 0273-1177, <https://doi.org/10.1016/j.asr.2018.06.019>.
- [3.8] Mueller, Jeurgen, "Thruster Options for Microspacecraft," tech. rep., *Micropropulsion for Small Spacecraft* (AIAA), 2000.
- [3.9] Brunetto, R. "Space weathering of small solar system bodies," *Earth, Moon, and Planets*, vol. 105, pp. 249–255, 2009.

- [3.10] Babuscia, A., et al., “Inflatable antenna for cubesat: Extension of the previously developed s-band design to the X-band,” AIAA Space, 2015.
- [4.1] Mehrparvar, Arash (February 20, 2014). "CubeSat Design Specification" The CubeSat Program, CalPoly SLO. The CubeSat Program, CalPoly SLO.
- [4.2] Masse, Robert, et al. “AF-M315E Propulsion System Advances and Improvements.” 52nd AIAA/SAE/ASEE Joint Propulsion Conference, 2016, doi:10.2514/6.2016-4577.
- [4.3] Sawka, Wayne N., and Mcpherson, Michael. “Electrical Solid Propellants: A Safe, Micro to Macro Propulsion Technology.” 49th AIAA/ASME/SAE/ASEE Joint Propulsion Conference, 2013, doi:10.2514/6.2013-4168.
- [4.4] Marrese-Reading, Colleen. “Microfluidic Electrospray Propulsion (MEP) Thruster Performance with Microfabricated Emitter Arrays for Indium Propellant.” 52nd AIAA/SAE/ASEE Joint Propulsion Conference, 2016, doi:10.2514/6.2016-4738.
- [4.5] Krejci, David, et al. “Emission Characteristics of Passively Fed Electrospray Microthrusters with Propellant Reservoirs.” *Journal of Spacecraft and Rockets*, vol. 54, no. 2, 2017, pp. 447–458., doi:10.2514/1.a33531.
- [4.6] GOMspace, MEMS Cold Gas Propulsion Module for 2U+ nanosatellites. Internet: <https://gomspace.com/shop/subsystems/attitude-orbit-control-systems/nanoprop-3u-propulsion.aspx>, 2017.
- [4.7] Bonin, G et al. “CanX–4 and CanX–5 Precision Formation Flight: Mission Accomplished!” In Proceedings of the 29th Annual AIAA/USA Conference on Small Satellites, Logan, UT, USA, 8–13 August 2015
- [4.8] Gibbon, D., et al. “Cost Effective Propulsion Systems for Small Satellites Using Butane Propellant.” *Acta Astronautica*, vol. 51, no. 1-9, 2002, pp. 145–152., doi:10.1016/s0094-5765(02)00074-7.
- [4.9] Lee, Riki, et al. “Free Molecule Micro-Resistojet: Nanosatellite Propulsion.” 41st AIAA/ASME/SAE/ASEE Joint Propulsion Conference & Exhibit, 2005, doi:10.2514/6.2005-4073.
- [4.10] Hejmanowski, N.J.C.A et al., “CubeSat High Impulse Propulsion System (CHIPS).” In Proceedings of the 62nd JANNAP Propulsion Meeting (7th Spacecraft Propulsion), Nashville, TN, USA, 1–5 June 2015.
- [4.11] Robin, Met al., “An Ammonia Microresistojet (MRJ) for micro Satellites.” In Proceedings of the 44th AIAA/ASME/SAE/ASEE Joint Propulsion Conference & Exhibit, Hartford, CT, USA, 21–23 July 2008.
- [4.12] Mueller, Juergen, et al. “An Overview of Mems-Based Micropropulsion Developments at JPL.” *Acta Astronautica*, vol. 52, no. 9-12, 2003, pp. 881–895., doi:10.1016/s0094-5765(03)00069-9.
- [4.13] Silva, Marsil A.c., et al. “Vaporizing Liquid Microthrusters with Integrated Heaters and Temperature Measurement.” *Sensors and Actuators A*, vol. 265, 2017, pp. 261–274.
- [4.14] Lee, Jongkwang, and Taegy Kim. “MEMS Solid Propellant Thruster Array with Micro Membrane Igniter.” *Sensors and Actuators A: Physical*, vol. 190, 2013, pp. 52–60.
- [4.15] Krusharev, I, et al., “Cubesat Micro-Propulsion Systems for Extending the Capabilities of Academic Projects.” IAC 2014, Toronto.
- [4.16] J.L.P.A., Moerel et al., “Development of Micro Propulsion System Technologies for Minisatellites in the Netherlands.” Proceedings of the Space Propulsion 2008, 5th International Spacecraft Propulsion Conference
- [4.17] Takir, Driss, and Joshua P. Emery. “Outer Main Belt Asteroids: Identification and Distribution of Four 3-Mm Spectral Groups.” *Icarus*, vol. 219, no. 2, 2012, pp. 641–654., doi:10.1016/j.icarus.2012.02.022.

- [4.18] Rivkin, Andrew S., and Joshua P. Emery. "Detection of Ice and Organics on an Asteroidal Surface." *Nature*, vol. 464, no. 7293, 2010, pp. 1322–1323., doi:10.1038/nature09028.
- [4.19] Lauretta, D. S., et al. "The Unexpected Surface of Asteroid (101955) Bennu." *Nature*, vol. 568, no. 7750, 2019, pp. 55–60., doi:10.1038/s41586-019-1033-6.
- [4.20] Air Force Space Command, Range Safety User Requirements Manual Volume 3 - Launch Vehicles, Payloads, And Ground Support Systems Requirements, 2011. (<http://static.e-publishing.af.mil/production/1/afspc/publication/afspcman91-710v3/afspcman91-710v3.pdf>).
- [4.21] Sutton, George Paul, and Oscar Biblarz. *Rocket Propulsion Elements*. 8th ed., Wiley., 2017.
- [4.22] Slough, John, et al. "Micro-Discharge Micro-Thruster." 2005, doi:10.21236/ada437433.
- [4.23] Sarda, Karan, et al. "Canadian Advanced Nanospace Experiment 2: Scientific and Technological Innovation on a Three-Kilogram Satellite." *Acta Astronautica*, vol. 59, no. 1-5, 2006, pp. 236–245., doi:10.1016/j.actaastro.2006.02.054
- [4.24] W.E. Acree, Jr., J.S. Chickos, "Phase Transition Enthalpy Measurements of Organic and Organometallic Compounds" in *NIST Chemistry WebBook*, NIST Standard Reference Database Number 69, National Institute of Standards and Technology, Gaithersburg MD, 20899
- [4.25] Chujo, Toshihiro, et al. "Development of Solid-Gas Equilibrium Propulsion System for Small Spacecraft." *Acta Astronautica*, vol. 140, 2017, pp. 133–139.
- [4.26] M. G. el Hak, "The fluid mechanics of microdevices - The Freeman ScholarLecture," *J. Fluids Engineering*, vol. 121, no. 5, pp. 5–33, 1999.
- [4.27] Torre, Federico La. "Gas Flow in Miniaturized Nozzles for Microthrusters". 2011. TU Delft. PhD Dissertation. ISBN: 978-94-91211-62-1
- [4.28] Kundu, Pijus, et al. "Design, Fabrication and Performance Evaluation of a Vaporizing Liquid Microthruster." *Journal of Micromechanics and Microengineering*, vol. 22, no. 2, 2012.
- [4.29] Jaeger, Richard C. *Introduction to Microelectronic Fabrication*. 2nd ed., vol. 5, Pearson Education, 2014.
- [4.30] Spisz, Ernie W. et al. "Thrust Coefficient Losses for Low-Thrust Nozzles" NASA, October 1965
- [4.31] Massier, P. F., Back, L. H, Noel, M. B. and Saheli, F., Viscous Effects on the Flow Coefficient for a Supersonic Nozzle-, *AIAA J.*, vol 8, No 3, 605-607, 1970
- [4.32] Parsopoulos, Konstantinos, et al. "Particle Swarm Optimization Methods for Constrained Optimization Problems." *Frontiers in Artificial Intelligence and Applications*. 2001.
- [4.33] Das, Swagatam, et al. "Particle Swarm Optimization and Differential Evolution Algorithms: Technical Analysis, Applications and Hybridization Perspectives," *Advances of Computational Intelligence in Industrial Systems*, Studies in Computational Intelligence, Springer–Verlag, Berlin, 2008, pp. 1–34.
- [4.34] Mezura-Montes E., Flores-Mendoza J.I. (2009) Improved Particle Swarm Optimization in Constrained Numerical Search Spaces. In: Chiong R. (eds) *Nature-Inspired Algorithms for Optimization*. Studies in Computational Intelligence, vol 193. Springer, Berlin, Heidelberg
- [4.35] Aziz, Nor Azlini Ab, et al. "Particle Swarm Optimization for Constrained and Multiobjective Problems: A Brief Review". *2011 International Conference on Management and Artificial Intelligence*.

- [4.36] Yang JM., Chen YP., Horng JT., Kao CY. (1997) “Applying family competition to evolution strategies for constrained optimization”. In: Angeline P.J., Reynolds R.G., McDonnell J.R., Eberhart R. (eds) *Evolutionary Programming VI*. EP 1997. Lecture Notes in Computer Science, vol 1213. Springer, Berlin, Heidelberg
- [4.37] Shi, Y., Eberhart, R.C. “Parameter Selection in Particle Swarm Optimization.” *Evolutionary Programming VII* (1998). Pp. 591-600
- [4.38] Menter, F. R. “Two-Equation Eddy-Viscosity Turbulence Models for Engineering Applications.” *AIAA Journal*, vol. 32, no. 8, 1994, pp. 1598–1605., doi:10.2514/3.12149.
- [4.39] Louwerse, M C, et al. “Nozzle Fabrication for Micropropulsion of a Microsatellite.” *Journal of Micromechanics and Microengineering*, vol. 19, no. 4, 2009, p. 045008., doi:10.1088/0960-1317/19/4/045008.
- [4.40] Campbell, Stephen A. *The Science and Engineering of Microelectronic Fabrication*. Oxford University Press, 2001.
- [4.41] Achtsnick, M., et al. “Modelling and Evaluation of the Micro Abrasive Blasting Process.” *Wear*, vol. 259, no. 1-6, 2005, pp. 84–94., doi:10.1016/j.wear.2005.01.045.
- [4.42] Arif, M., et. al, “Analytical model to determine the critical conditions for the modes of material removal in the milling process of brittle material,” *Journal of Materials Processing Technology*, 212 (2012) 1925–1933.
- [4.43] Rusnaldy, et al. “An Experimental Study on Microcutting of Silicon Using a Micromilling Machine.” *The International Journal of Advanced Manufacturing Technology*, vol. 39, no. 1-2, 2007, pp. 85–91., doi:10.1007/s00170-007-1211-9.
- [4.44] Guckenberger, David, et al., “Micromilling: A method for ultra-rapid prototyping of plastic microfluidic devices.” *Lab Chip*, 2015. doi:10.1039/c5lc00234f.
- [4.45] Golshan, Abolfazl, et al., “Ultraprecision Machining of Silicon Wafer by Micromilling Process.” *Advances in Material & Processing Technologies Conference*, 2017.
- [4.46] Cai, Yukui, et al. “Optimization of Machining Parameters for Micro-Machining Nozzle Based on Characteristics of Surface Roughness.” *The International Journal of Advanced Manufacturing Technology*, vol. 80, no. 5-8, 2015, pp. 1403–1410., doi:10.1007/s00170-015-7115-1.
- [4.47] Cai, Yukui, et al. “Influence of Machined Surface Roughness on Thrust Performance of Micro-Nozzle Manufactured by Micro-Milling.” *Experimental Thermal and Fluid Science*, vol. 77, 2016, pp. 295–305., doi:10.1016/j.expthermflusci.2016.05.004.
- [5.1] Megnin, Christof, et al., “A Bistable SMA Microvalve for 3/2-Way Control,” *Sensors and Actuators A: Physical*, Volume 188, 2012, Pages 285-291, ISSN 0924-4247.
- [5.2] Cheng, Choujun, et al., “Normally Closed Plunger-Membrane Microvalves Self-Actuated Electrically Using a Shape Memory Alloy Wire.” *Microfluidics and Nanofluidics* (2018). <https://doi.org/10.1007/s10404-018-2049-1>.
- [5.3] Megnin, Christof, et al., “Shape Memory Alloy Microvalves for a Fluidic Control System.” *Journal of Micromechanics and Microengineering*, Volume 24. 2013.
- [5.4] Yang, B.Z., et al., “A Latchable Microvalve Using Phase Change of Paraffin Wax.” *Sensors and Actuators*, Volume 134. 2007. pp. 194-200.
- [5.5] Au, Anthony K., et al., “Microvalves and Micropumps for BioMEMS.” *Micromachines*, Volume 2. 2011. doi:10.3390/mi2020179.

- [5.6] Oh, Hyun-Ung, et al., “Verification of MEMS Fabrication Process for the Application of MEMS Solid Propellant Thruster Arrays in Space Through Launch and On-Orbit Environment Tests.” *Acta Astronautica*, Volume 131. 2011.
- [5.7] Mueller, Jeurgan “A Review and Applicability Assessment of MEMS-Based Microvalve Technologies for Microspacecraft Propulsion.” *Micropropulsion for Small Spacecraft VA: AIAA*, 2000, vol. 187, Progress in Astronautics and Aeronautics, ch. 19.
- [5.8] Bintoro, Jemmy, “An Electromagnetic Actuated Microvalve Fabricated on a Single Wafer.” 2004. Georgia Institute of Technology. PhD Dissertation.
- [5.9] Ren, Hong, and Gerhard, Einsele, “Design and Fabrication of a Current-Pulse-Excited Bistable Magnetic Microactuator.” *Sensors and Actuators A: Physical*, Volume 58, pp. 259–64.
- [5.10] Chakraborty, Indrani, et al., “MEMS Micro-Valve for Space Applications.” *Sensors and Actuators A: Physical*, Volume 83, Issues 1–3, 2000, pp. 188-193.
- [5.11] Yang, EH., et al., “Leak-Tight Piezoelectric Microvalve for High-Pressure Gas Micropropulsion.” *Journal of Microelectromechanical Systems*, Volume 13, Number 5, October 2004.
- [5.12] Shannon Rios and Andrew Fleming, "A Novel Electrical Configuration for Three Wire Piezoelectric Bimorph Micro-Positioners," 2014 IEEE/ASME International Conference on Advanced Intelligent Mechatronics, 2014. doi:10.1109/AIM.2014.6878287.
- [5.13] S.O. Moheimani and Andrew J. Fleming, “Piezoelectric Transducers for Vibration Control and Damping.” Springer London, 2006.
- [5.14] Christophe Poizat, Ayech Benjeddou. “On Analytical and Finite Element Modelling of Piezoelectric Extension and Shear Bimorphs.” *Computers & Structures*, vol. 84, no. 22-23, 2006, pp. 1426–1437. doi:10.1016/j.compstruc.2005.01.005.
- [5.15] Jan Smits, et al. “The Constituent Equations of Piezoelectric Bimorphs.” *Proceedings, IEEE Ultrasonics Symposium*, 1990, doi:10.1109/ultsym.1989.67092.
- [5.16] Q.-M. Wang and L. E. Cross, “Constitutive Equations of Symmetrical Triple Layer Piezoelectric Benders,” *IEEE Transactions on Ultrasonics, Ferroelectrics and Frequency Control*, vol. 46, no. 6, 1999, pp. 1343– 1351.
- [5.17] Jundong Song, et al. “Design Optimization of PVDF-Based Piezoelectric Energy Harvesters.” *Heliyon*, vol. 3, no. 9, 2017, doi:10.1016/j.heliyon.2017.e00377.
- [5.18] Ayech Benjeddou, Marcelo Trindade, and Roger Ohayon, “A Unified Beam Finite Element Model for Extension and Shear Piezoelectric Actuation Mechanisms.” *Journal of Intelligent Material Systems and Structures*. Vol. 8, 1997, pp. 1012-1025. doi: 10.1177/1045389X9700801202.
- [5.19] Ayech Benjeddou, Marcello Trindade, and Roger Ohayon. “Piezoelectric actuation mechanisms for intelligent sandwich structures.” *Smart Mater Struct*. Vol 9, 2000, pp.328–35.
- [5.20] Ayech Benjeddou, “Advances in Piezoelectric Finite Element Modeling of Adaptive Structural Elements: a Survey.” *Computers and Structures*, vol. 76, no. 1-3, 2000, pp. 347–363., doi:10.1016/s0045-7949(99)00151-0.
- [5.21] Precision Acoustics, “Guide to Using Poled PVDF: PVDF Properties and Uses,” datasheet, <https://www.acoustics.co.uk/product/pvdf/>.
- [5.22] Liuxia Ruan, et al., “Properties and Applications of the  $\beta$  Phase Poly(vinylidene fluoride).” *Polymers*, Vol. 10, 2008. doi:10.3390/polym10030228.

- [5.23] Mohammad Malakooti and Henry Sodano, “Piezoelectric Energy Harvesting Through Shear Mode Operation.” *Smart Materials and Structures*, Vol. 24, 2015. doi:10.1088/0964-1726/24/5/055005.
- [5.24] “Ceramic Materials (PZT) - Boston Piezo-Optics Inc.” Boston Piezo Optics Inc., [bostonpiezooptics.com/ceramic-materials-pzt](http://bostonpiezooptics.com/ceramic-materials-pzt).
- [5.25] Jose Gonzalez, et al., “A Prospect of the Piezoelectric Effect to Supply Power to Wearable Electronic Devices.” *Proc. 4th Int. Conf. on Materials Engineering for Resources (Akita, Japan) 2001*, pp 202–07.
- [5.26] Irinela Chilibon, et al., “PZT and PVDF Bimorph Actuators.” *Journal of Optoelectronics and Advanced Materials*. Vol. 9. 2007, pp. 1939-1943.
- [5.27] S.P. Beeby, et al. “Energy Harvesting Vibration Sources for Microsystems Applications.” *Measurement Science and Technology*, vol. 17, no. 12, 2006, doi:10.1088/0957-0233/17/12/r01.
- [5.28] Yonggang Jiang, et al., “Low-Frequency Energy Harvesting Using a Laminated PVDF Cantilever with a Magnetic Mass.” *Power MEMS*. 2010.
- [5.29] “Advanced Electro Ceramics.” Soft PZT, [www.ceramtec.com/ceramic-materials/soft-pzt/](http://www.ceramtec.com/ceramic-materials/soft-pzt/).
- [5.30] Matthew Hooker, “Properties of PZT-Based Piezoelectric Ceramics Between -150 and 250°C.” *NASA Contractor Report*. 1998.
- [5.31] Sun, Jian, et al. “Comparison of Bonding of Bulk PZT to Silicon by Intermediate Glass Layer and by Intermediate Au Layer.” *Materials Science Forum*, vol. 663-665, 2010, pp. 490–493., doi:10.4028/www.scientific.net/msf.663-665.490.
- [5.32] Tanaka, Katsuhiko, et al. “Wafer Bonding of Lead Zirconate Titanate to Si Using an Intermediate Gold Layer for Microdevice Application.” *Journal of Micromechanics and Microengineering*, vol. 16, no. 4, 2006, pp. 815–820., doi:10.1088/0960-1317/16/4/019.
- [5.33] “Piezoelectric Ring Stacks and Chips, 2.6 Mm to 9.0 Mm Travel.” Thorlabs, [www.thorlabs.com/newgrouppage9.cfm?objectgroup\\_id=11059](http://www.thorlabs.com/newgrouppage9.cfm?objectgroup_id=11059).
- [5.34] I. Fazal, M.C. Elwenspoek, “Design and Analysis of a High Pressure Piezoelectric Actuated Microvalve.” *J. Micromech. Microeng.* 17 (2007) 2366–2379.
- [5.35] “SR Series 150V Piezo Ring Stack Actuators.” PiezoDrive, [www.piezodrive.com/actuators/150v-piezo-ring-stack-actuators/](http://www.piezodrive.com/actuators/150v-piezo-ring-stack-actuators/).
- [5.36] Mortensen, Niels Asger, et al. “Reexamination of Hagen-Poiseuille Flow: Shape Dependence of the Hydraulic Resistance in Microchannels.” *Physical Review E*, vol. 71, no. 5, 2005, doi:10.1103/physreve.71.057301.
- [5.37] “NAC2124-Hxx - Noliac - Your Piezo Partner.” Noliac, [www.noliac.com/products/actuators/ring-stacks/show/nac2124-hxx/](http://www.noliac.com/products/actuators/ring-stacks/show/nac2124-hxx/).
- [5.38] Garra, J., et al. “Dry Etching of Polydimethylsiloxane for Microfluidic Systems.” *Journal of Vacuum Science & Technology A: Vacuum, Surfaces, and Films*, vol. 20, no. 3, 2002, pp. 975–982., doi:10.1116/1.1460896.
- [5.39] Tang, K C, et al. “Evaluation of Bonding between Oxygen Plasma Treated Polydimethyl Siloxane and Passivated Silicon.” *Journal of Physics: Conference Series*, vol. 34, 2006, pp. 155–161., doi:10.1088/1742-6596/34/1/026.
- [6.1] Kalita, Himangshu, Thangavelautham, Jekanthan, “Motion Planning on an Asteroid Surface with Irregular Gravity Fields,” *Advances in the Astronautical Sciences*, February 2019.

- [6.2] W. Gao and J. C. Hung, "Variable structure control of nonlinear systems: A new approach," IEEE Trans. Ind. Electron., vol. 40, no. 1, pp. 45–55, Feb. 1993.
- [6.3] Zheng Zhu, et al. "Adaptive Sliding Mode Control for Attitude Stabilization With Actuator Saturation." IEEE Transactions on Industrial Electronics, vol. 58, no. 10, 2011, pp. 4898–4907., doi:10.1109/tie.2011.2107719.
- [6.4] D.J. Scheeres. "Orbit Mechanics About Asteroids and Comets." Journal of Guidance, Control, and Dynamics, vol. 35, no. 3, 2012, pp. 987–997., doi:10.2514/1.57247.
- [6.5] D.J. Scheeres, et al. "The Geophysical Environment of Bennu." Icarus, vol. 276, 2016, pp. 116–140., doi:10.1016/j.icarus.2016.04.013.
- [6.6] Lange, Caroline, et al., "Exploring Small Bodies: Nano- and Microlander Options Derived from the Mobile Asteroid Surface Scout." Advances in Space Research, Volume 62, Issue 8, 2018, Pages 2055-2083, ISSN 0273-1177, <https://doi.org/10.1016/j.asr.2018.05.013>.
- [6.7] R. G. Reid, L. Roveda, I. Nesnas and M. Pavone. (2014). "Contact Dynamics of Internally-Actuated Platforms for the Exploration of Small Solar System Bodies".
- [6.8] Lanczos, Cornelius. *The Variational Principles of Mechanics*. Dover Publications, 2005.